AN AMMONIA-FUELLED SOLID OXIDE FUEL CELL - INTERNAL COMBUSTION ENGINE HYBRID SYSTEM FOR SHIPS

A.A. KOEKKOEK

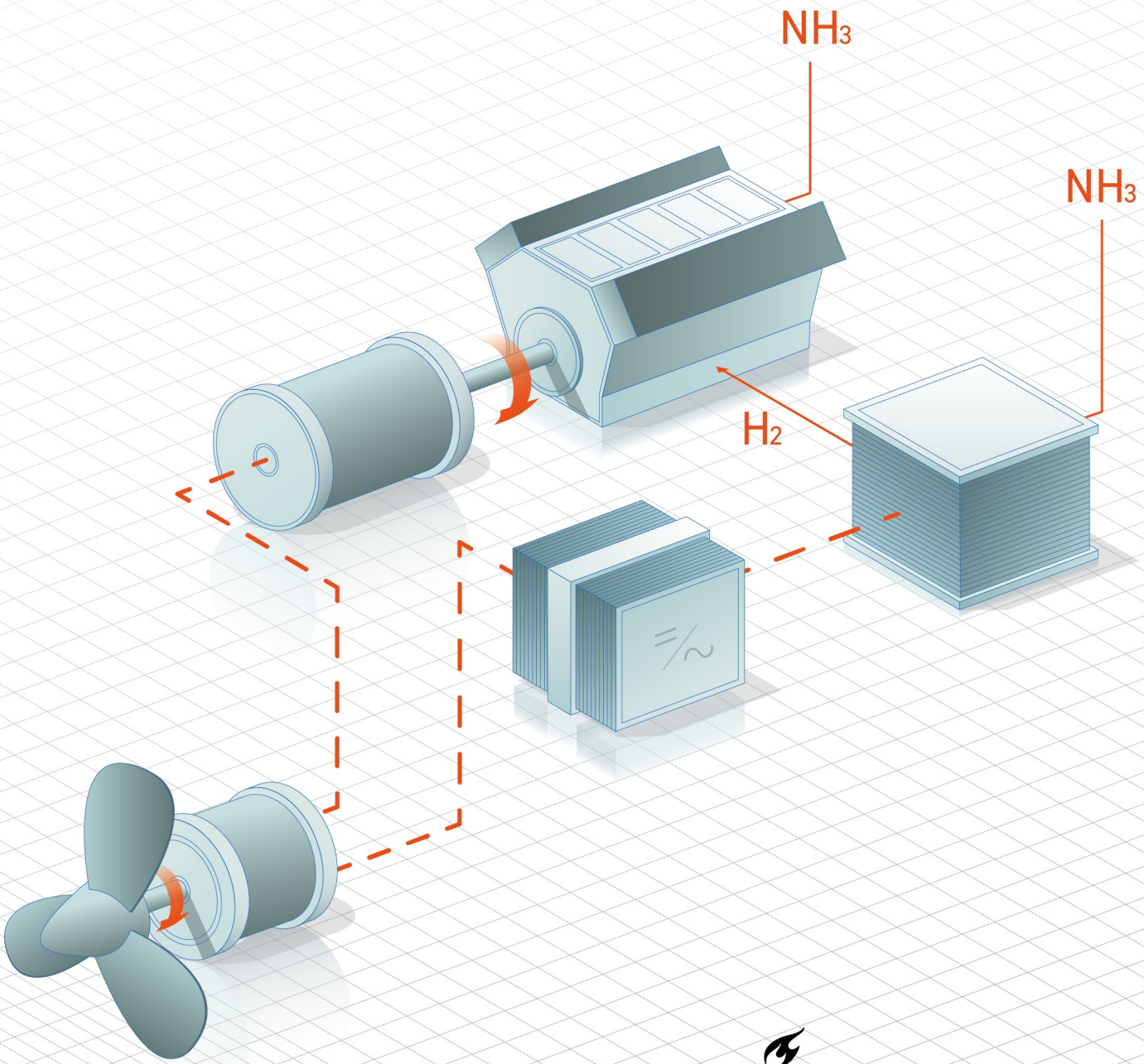

TU Delft Delft University of Technology

An Ammonia-Fuelled Solid Oxide Fuel Cell – Internal Combustion Engine Hybrid System for Ships

by

A. A. Koekkoek

to obtain the degree of Master of Science
in Mechanical Engineering (Energy, Flow & Process Technology)
at the Delft University of Technology,
to be defended publicly on Friday December 10, 2021 at 13:00.

Student number:	4475291	
Project duration:	Februari 8, 2021 – December 10, 2021	
Thesis committee:	Dr. Ir. L. van Biert,	TU Delft, supervisor
	Prof. Dr. Ir. W. de Jong,	TU Delft
	Dr. Ir. P. de Vos,	TU Delft
	Prof. Dr. A. J. M. van Wijk,	TU Delft, co-supervisor and chairman

Cover image by Harm Cnossen. An electronic version of this thesis is available at
http://repository.tudelft.nl/.

TU Delft

Preface

The success of my master's thesis can only slightly be attributed to my efforts: Especially the help and assistance of others have been crucial the past ten months.

Mainly, I want to thank my supervisor, Lindert van Biert. I have been fortunate with more help and constructive feedback than I would have ever expected before starting this project. The numerous face-to-face meetings on Monday morning were extremely valuable. His suggestions have kept me on track and pushed me in the right direction. Next, I would like to express my appreciation to my co-supervisor, Ad van Wijk. His wise words prevented me from losing myself in the details or forgetting the broader context of my research. Also, I want to thank Peter de Vos for allowing me to work on the fascinating 'AmmoniaDrive' concept. Furthermore, special thanks to Harm Cnossen for making the stunning cover, Pieter Spruijt for connecting me with Peter de Vos, Jeroen Reurings for sharing some ins and outs of his research, Maurice Rijs for providing feedback on my report and fellow *Energy, Flow and Process Technology*-students for exchanging thoughts.

I take my hat off to all friends, (former JvB-)housemates, family and Joica, who provided company and distraction and supported me the past months!

A. A. Koekkoek
Rotterdam, December 2021

Abstract

Ammonia (NH_3) may reduce CO_2 emissions from the marine industry as it is carbon-free and more energy-dense than hydrogen or batteries. Pure ammonia exhibits poor combustion characteristics, so several researchers have already operated small-scale internal combustion engines (ICEs) with ammonia-hydrogen blends. However, nitrogen oxides (NO_x) and unburned ammonia are major objections that require the after-treatment of exhaust gases. Experimental studies with solid oxide fuel cell (SOFC) stacks up to 1 kW demonstrated that SOFCs can convert ammonia to electricity with the highly endothermic ammonia cracking reaction at the fuel electrode or before the SOFC as an intermediate step. Although SOFCs tend to be more efficient and emit fewer NO_x compared to ICEs, their power density, dynamic behaviour and investment costs are inferior. Different authors came up with integrations of mostly methane-fuelled SOFCs with gas turbines or internal combustion engines.

This work presents an ammonia-fuelled SOFC–ICE hybrid system in which hydrogen off-gas from an SOFC enhances ammonia combustion in an ICE. 0-D components models are developed in an integrated model to quantify the effect of different parameters on fuel efficiency, power density, and heat management. The hybrid system simulations vary three parameters, all in three different ways. First, the SOFC provides either 25, 50 or 75% of the hybrid system power, resulting 25/75, 50/50 or 75/25 SOFC/ICE power splits. Secondly, either 0, 50 or 100% of the hydrogen in the SOFC is obtained from external cracking before the stack. Thirdly, the share of hydrogen in the ammonia-hydrogen ICE fuel blends is varied: 20, 30 and 40%. This leads to 27 distinct simulations, all at 5000 $A \cdot m^{-2}$ SOFC current density. Besides, current density is varied from 2500 and 5000 to 9000 $A \cdot m^{-2}$ in the 50/50 SOFC/ICE power split configuration.

Full internal cracking of ammonia in the SOFC results in an electrical efficiency of up to 58% and 54% (based on the lower heating value) for a 75/25 and 50/50 power split, respectively, but it leads to heat management failures in the 25/75 power split; where 50% external cracking results in 47% efficiency. Complete external instead of internal cracking decreases efficiency by at most 10 percent points (75/25 power split), because additional fuel is needed heat to the external cracker. Moreover, external cracking results in increased power consumption by the cathode air blower. The ICE efficiency, 41% (standalone system) or 43% (being part of the hybrid system), is outperformed in all 27 simulations mentioned above. The after-treatment model predicts the formation of highly unwanted N_2O. The computed SOFC–ICE specific volume is 2, 3 or 4 times larger than an ICE, but less fuel tank space required could cancel this out.

This research indicates that an SOFC reduces fuel consumption compared to an ICE, but using hydrogen off-gas with ammonia in an ICE is advantageous for power density and efficiency. Furthermore, operational parameters of the SOFC can be adjusted in favour of the system efficiency until there is too little electrochemical waste heat compared to the heat absorbed by ammonia cracking in the SOFC. Amongst many other topics, future research should include part load and dynamic operation because of the expected benefits of the hybrid system.

Contents

Nomenclature

Abbreviations

AC	Alternating current
ADR	Ammonia decomposition reaction
BCZY	Barium cerium zirconium yttrium oxide
CGO	Cerium gadolinium oxide
CI	Compression ignition
CW	Cooling water
DC	Direct current
EGR	Exhaust gas recirculation
FC	Fuel cell
FSCR	Fast selective catalytic reduction (reaction)
Genset	Combination of engine and generator (generator set)
GHG	Greenhouse gas
GT	Gas turbine
HAER	Hydrogen to ammonia energy ratio
HCCI	Homogeneous charge compression ignition
HOR	Hydrogen oxidation reaction
ICE	Internal combustion engine
LSF	Lanthanum strontium ferrite
LSGM	Lanthanum strontium gallium magnesium oxide
LSM	Strontium-doped lanthanum manganite
NG	Natural gas
PD	Power density
PEMFC	Proton-exhange membrane fuel cell
PEN	Positive-electrolyte-negative
PS	Power split
RCCI	Reactivity controlled compression condition
SA	Standalone
SCR	Selective catalytic reduction (reactor)
SI	Spark ignition

SOFC	Solid oxide fuel cell
SOFC-H	Proton conducting solid oxide fuel cell
SOFC-O	Oxide conducting solid oxide fuel cell
SP	Setpoint
SSCR	Standard selective catalytic reduction (reaction)
TPB	Three-phase boundary or triple-phase boundary
WGC	Wastegate control
YSZ	Yttria-stabilised zirconia

Constants

$\bar{R}$	Universal gas constant	$8.314\,\mathrm{J\cdot mol^{-1}\cdot K^{-1}}$
F	Faraday's constant	$96485\,\mathrm{C\cdot mol^{-1}}$

Variables

β	Transfer coefficient	–
$\dot{m}$	Mass flow	$\mathrm{kg\cdot s^{-1}}$
$\dot{N}$	Molar flow rate	$\mathrm{mol\cdot s^{-1}}$
$\dot{Q}$	Heat flow	W
ϵ	Geometric compression ratio	–
λ	Air excess ratio	–
ν	Stoichiometric coefficient	–
σ	Electric or ionic conductivity	$\Omega^{-1}\mathrm{m^{-1}}$
σ	Stoichiometric air-fuel ratio	–
τ	Thickness	m
a, b, c	Seiliger parameter	–
afr	Air-fuel ratio	–
$bsfc$	Brake specific fuel consumption	$\mathrm{g\cdot kWh^{-1}}$
D	Diffusion coefficient	$\mathrm{m^2\cdot s^{-1}}$
E	Activation energy	$\mathrm{J\cdot mol^{-1}}$
E	Voltage	V
E^0	Reversible open circuit voltage at standard pressure	V
ecr	External cracking ratio	–
g	Specific gibbs free energy	$\mathrm{J\cdot mol^{-1}}$
h	Cell height	m
h	Specific enthalpy	$\mathrm{J\cdot mol^{-1}}$
i	Current density	$\mathrm{A\cdot m^{-2}}$

i	Number of cylinders	–
i_0	Exchange current density	$\mathrm{A \cdot m^{-2}}$
i_1	Limiting current density	$\mathrm{A \cdot m^{-2}}$
K	Number of substances in the fuel blend	–
k	Number of revolutions per cycle	–
k	Pre-exponential factor	$\mathrm{A \cdot m^{-2}}$
L	Cell length	m
N	Number of revolutions per second	$\mathrm{s^{-1}}$
n_e	Electrons transferred per reaction	–
n_c	Polytropic compression exponent	–
n_e	Polytropic expansion exponent	–
P	Power	W
p	(Partial) pressure	Pa
p^0	Standard pressure	bar
p_me	Mean effective pressure	bar
PS	Power split	–
q	Specific heat transferred	$\mathrm{J \cdot kg^{-1}}$
R	Specific gas constant	$\mathrm{J \cdot kg^{-1} \cdot K^{-1}}$
r	Area-specific reaction rate	$\mathrm{mol \cdot s^{-1} m^{-2}}$
r	Area-specific resistance	$\mathrm{\Omega \cdot m^2}$
r_c	Effective compression ratio	–
r_e	Effective expansion ratio	–
RR	Recycle ratio	–
s	Specific entropy	$\mathrm{J \cdot mol^{-1} K^{-1}}$
T	Temperature	K
u	Specific internal energy	$\mathrm{J \cdot kg^{-1}}$
UF	Fuel utilisation	–
V_BDC	Total volume	$\mathrm{m^3}$
V_s	Swept volume	$\mathrm{m^3}$
V_TDC	Clearance volume	$\mathrm{m^3}$
W	Cell width	m
w	Specific work	$\mathrm{J \cdot kg^{-1}}$
x	Compression stroke effectiveness factor	–
x	Mole fraction	–

X_A	Isochoric heat release fraction	–
Z	Compressibility factor	–
(i)mep	(indicated) mean effective pressure	
X	Selectivity	–
Y	Yield	–

Subscripts

act	Activation
con	Concentration
eff	Effective
el	Electrolyte
act	activation
an	Anode
b	brake
c	Combustion
ca	Cathode
com	Compressor
f	fuel
nom	Nominal
ohm	ohmic
pol	Polytropic
tur	Turbine

1

Introduction

The International Maritime Organisation (IMO) estimated that the total greenhouse gas (GHG) emissions from shipping amount to over 1000 million tons of CO_2 equivalent per year; a 2.9% share in global GHG emissions [9]. In line with the global CO_2 reduction goals, the IMO has the ambition to reduce the annual GHG emissions by 50% in 2050 compared to 2008 [3]. Also, measures to reduce harmful emissions such as NO_x and SO_x are taken [3]. Apart from improving the combustion of conventional fuels, liquefied natural gas (LNG) is a clean alternative in terms of NO_x, SO_x, GHGs and particulate matters (PM). The research project 'GasDrive' studied the potential of a natural gas-fuelled integrated system of a solid oxide fuel cell (SOFC) and an internal combustion engine (ICE) [21]. Although the results in terms of efficiency and emission reduction were promising, it could not eliminate CO_2 emission, as natural gas is a fossil and carbon-based fuel. Ammonia (NH_3) is being developed as a carbon-free shipping fuel [47].

Ammonia is a tempting energy carrier as it is stored relatively easily. It condenses below -33°C at atmospheric pressure or above 10 bar at room temperature [34]. Figure 1.1 [122] shows its high energy density compared to other carbon-free energy carriers. With an annual production of 150 million tonnes, ammonia synthesis is well established [86], but responsible for around 1% of global CO_2 emissions due to the high pressures and temperatures involved and the use of natural gas as a hydrogen source [68]. Efforts are made to make the conventional "Haber-Bosch" production process more efficient. Most importantly, electrolysis with renewable electricity could supply the required hydrogen [68], making ammonia an attractive zero-carbon renewable energy carrier. Safety issues arise from the toxicity of ammonia but the marine industry is experienced in handling the substance [41, 63].

Its poor combustion characteristics make ammonia unsuitable for utilising directly in conventional marine internal combustion engines but blending ammonia with a promoter fuel is a solution [30, 122] which is gaining attention from commercial parties [6, 79]. Several researchers investigated ammonia-hydrogen combustion in small-scale engines [30], which is favoured over ammonia-hydrocarbon combustion as hydrogen is carbon-free. A crucial challenge is the suppression of excess NO_x and unburned ammonia emissions [30].

Solid oxide fuel cells manage to convert ammonia to electric power in an efficient way [39]. First, am-

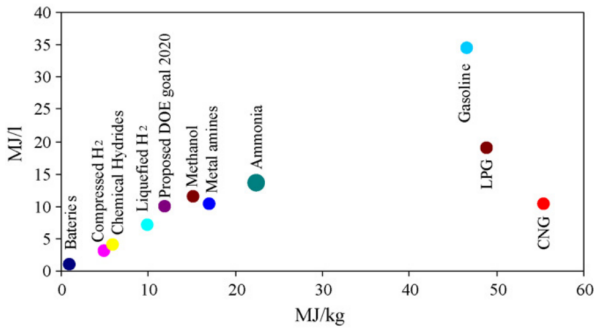

Figure 1.1: Volumetric and gravimetric energy densities of different fuels [122].

monia is decomposed into hydrogen and nitrogen [92] inside or outside the fuel cell. Then, electric current is generated from the electrochemical oxidation of hydrogen. A major advantage of SOFCs is that the high-temperature waste heat facilitates the highly endothermic ammonia decomposition reaction [64]. On top of that, nickel, a conventional SOFC anode material, catalyses the electrochemical oxidation of hydrogen and the ammonia decomposition reaction[64, 92]. An SOFC can never utilise 100% of the fuel, so the off-gas contains hydrogen. SOFCs are expected to emit little NO_x [39, 58, 88], especially compared to ammonia-fuelled ICEs. However, SOFCs are inferior to ICEs in terms of power density, capability of transient operation and investment costs [104].

An ammonia-fuelled SOFC–ICE hybrid system is highly attractive in the context of zero-carbon shipping due to the complementary nature of an SOFC and ICE. Ammonia is converted efficiently to electrical energy in the SOFC, and hydrogen from the SOFC off-gas enhances ammonia combustion in the ICE. The ICE will satisfy the need for dynamic operability and high power density of a marine power plant while restraining the system's capital costs [38]. This idea was introduced by Peter de Vos and published in *SWZ Maritime* [38]: 'AmmoniaDrive: a solution for zero-emission shipping?!'. Experimental analyses of ammonia SOFC systems up to 1 kW and small automotive sized ICEs have been reported in literature, but it appears that the suggested hybrid system has not been analysed experimentally or numerically before. This research can make a useful effort to assess the proposed concept, and it is intended to provide a basis for experimental or more thorough numerical follow-up research. It is aimed to answer the following research question:

How can an ammonia fuelled SOFC–ICE hybrid marine propulsion system be designed and the influence of main operating parameters on fuel efficiency and power density quantified?

The following sub-questions will serve as a guideline to answer the main research question.

1. How can the relevant sub-components for an analysis on system level be modelled, validated and fitted into a system model?

2. How can the sub-components be combined in an SOFC–ICE hybrid marine propulsion system that is able to operate at part and full load?

3. Under what circumstances can the SOFC deliver enough hydrogen promoter fuel to the ICE, and when is additional cracking necessary?

4. What is the influence of current density, fuel utilisation, external cracking ratio, SOFC/ICE power split and the reduction of nitrogen compounds on the hybrid system?

2

Literature study

This chapter aims to describe relevant theory relating to an ammonia-fuelled SOFC–ICE hybrid marine propulsion system. It also acts as the basis for the problem statement, research questions and plan of approach stated in chapter 1. Section 2.1 involves an explanation of important background information about SOFCs in general. Section 2.2 clarifies how ammonia can be used as a fuel for SOFCs, and it points out relevant research related to this topic. The main results of a literature survey on ammonia-fuelled ICEs are provided in section 2.4 after the introduction of ICEs in section 2.3.

2.1. Solid oxide fuel cell

2.1.1. Working principle

A fuel cell converts the chemical energy of a substance to electricity and by electrochemical oxidation. Electrons flow from the anode to the cathode through an external circuit and can power a load. While a heat engine is subject to the Carnot limit of maximum theoretical efficiency, the Gibbs free energy limits the maximum fuel cell efficiency (equation 2.2) [69]. The theoretical efficiency limit of a heat engine can be higher than the theoretical limit of a fuel cell at elevated temperatures but suffers severely from internal irreversibilities, including heat loss and friction [49]. Apart from that, the maximum temperature of heat engines is subject to material and environmental constraints (NO_x formation). Therefore, the electrical efficiency of a fuel cell is generally higher as the chemical energy is converted directly into electrical work instead of via heat as an intermediate step.

Most fuel cells types operate at moderate temperatures up to 210°C [25]. Among them is the Proton-exchange membrane fuel cell (PEMFC), which uses a proton-conducting solid polymer electrolyte and has been the most popular type of fuel cell [40]. However, PEMFCs have some significant disadvantages in the context of this research: The low-temperature waste heat cannot be used to promote the endothermic, high-temperature decomposition reaction of ammonia fuel. Next to that, even traces of ammonia can poison PEMFCs [112]. Molten carbonate fuel cells operate typically between 600 and 700°C [69]. Solid oxide fuel cells can operate on even higher temperatures, often above 800°C and up to 1100°C [69]. Oxygen is reduced at the cathode in an SOFC. Oxide (O^{2-}) ions are conducted through a solid electrolyte from the cathode to the anode, where the oxide ion oxidises a fuel. The high operating temperature required to aid the ionic conductivity of the electrolyte, is advantageous as it delivers high-quality waste heat, which could be used in a downstream power cycle such as a gas turbine. The high temperature also allows for internal reforming or cracking, which creates the possibility of supplying fuels other than pure hydrogen directly to the fuel cell [29]. A schematic layout and the reactions taking place in a hydrogen-fuelled SOFC are shown in figure 2.1.

2.1.2. Components and arrangements

The electrolyte in an SOFC is a layer of solid oxide or ceramic material able to conduct oxide ions. It should be chemically and mechanically stable, and a low electronic conductivity has to prevent leakage current. It should also be compatible (especially in terms of thermal expansion) with the material at the anode and cathode [42]. YSZ: Zirconia (ZrO_2), stabilised with Yttria, (Y_2O_3) is the most usual electrolyte material; it is a stable material, able to conduct O^{2-} ions, which can move through vacancies in the crystal lattice, while the material is not electronically conducting [69]. Zirconia ideally requires temperatures above 800 °C for

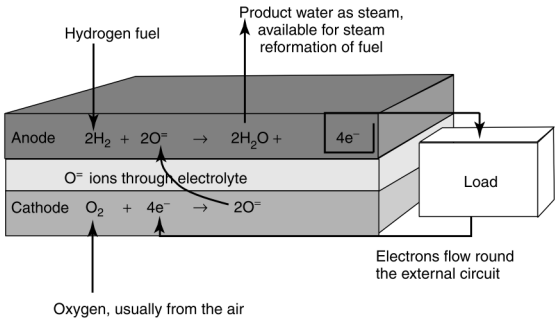

Figure 2.1: Reactions taking place in an SOFC fuelled with hydrogen [69].

good ionic conduction. Other electrolyte materials are proposed as well. For example, LaSrGaMgO (LSGM), showing better oxide conduction and able to operate at lower temperatures than YSZ, but has drawbacks as well; such as the formation of a resistive layer between the most common anode material, Ni-YSZ, and the LSGM electrolyte [44].

The anode material is of major importance as it is the place where the fuel is oxidised. The electrochemical reaction only occurs at, [110] or near [28] the three-phase boundary (TPB). The TPB a line interface composed of the place where the electrolyte, anode and the gas phase meet [110]. The electronic and ionic conductivity of the anode material should be high. The thermal expansion coefficient should match the thermal expansion coefficient of the electrolyte to prevent thermal stress. Furthermore, the anode should have a fine structure, be porous for gas diffusion, and have a large TPB. Ni-YSZ (Nickel-YSZ), a ceramic-metal composite, is the most common anode material [106]. The chemical stability at high temperatures is acceptable, and electronic and ionic conductivity are high. Ni-YSZ is a mixture of nickel and YSZ, so the thermal expansion coefficient is close to YSZ-electrolyte. Importantly, nickel is a suitable catalyst for the oxidation of hydrogen [125].

According to Shaikh et al. [106], carbon deposition and low resistance to sulphur poisoning are disadvantages of Ni-YSZ anodes. Apart from YSZ, CGO is used in nickel cermets as well and is reported to function well compared to YSZ [57, 106, 125]. Cu-CGO (Copper-Cerium-gadolinium oxide) could be one of the alternative anode materials [106].

The cathode should have high electronic conductivity, have a thermal expansion coefficient matching the thermal expansion coefficient of the electrolyte, and should be porous so that the oxygen can reach the TPB [12, 111]. The material should also be chemically stable, be a good catalyst for the reduction of oxygen and it should have a low cost [111]. The TPB micro-structure is highly dependent on the manufacturing technique and has a large impact on the electrochemical performance of the cathode [111]. Strontium-doped lanthanum manganite (LSM) is most common [42] and the preferred cathode material at high operating temperatures between 800°C and 1000°C [69]. Electrode kinetics weaken at lower temperatures, and this effect is strong in the reduction of oxygen at the cathode. The subsequent losses have to be limited, which calls for alternative materials at lower temperatures [111]. This includes perovskite-structured materials such as Lanthanum-Strontium-Ferrite (LSF) [25].

Fuel cells are stacked in series to achieve higher voltages, and they are separated by means of an interconnecting material. The electrically conducting interconnect connects the anode of one cell with the cathode of another cell. The interconnect material is subject to very strict demands: The material has to show excellent electrical conductivity, be stable and have a low permeability for hydrogen and oxygen. Furthermore, the thermal expansion should be close to the anode, cathode and electrolyte material to prevent thermal stresses. The material should be chemically compatible with the neighbouring components to prevent the formation of unwanted layers at the boundaries, the thermal conductivity should be adequate, it should resist oxidation, sulphur and carbon deposition, and it should be mechanically robust. All these demands must be satisfied in high temperature, oxidising and reducing environments, preferably at low cost [126]. Above 800°C, it is possible to use metals as an interconnect, but those are often expensive superalloys. Conventional steels differ too much in thermal expansion coefficient. Problems arising with metal interconnects are less likely to occur in lower temperature solid oxide fuel cells. An alternative to metal interconnects is using conducting (doped) ceramics. However, their manufacturing processes are complex [69].

Both a planar and a tubular arrangement, described by Larminie and Dicks [69], are possible for an

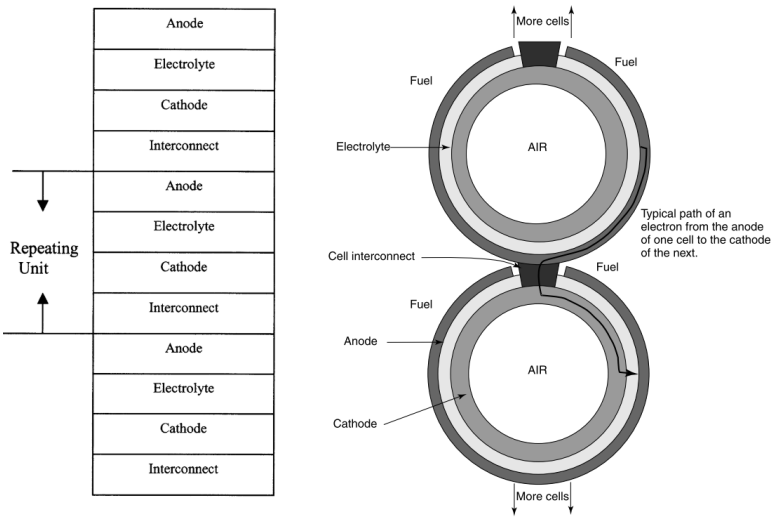

Figure 2.2: Schematic representation of an SOFC in planar arrangement [69] (left) and an SOFC in tubular arrangement [126] (right).

SOFC. The working principles are similar; a schematic representation is shown in figure 2.2. The major advantage of a tubular arrangement is the need for gas-tight sealing is reduced. However, power density tends to be low as electrons are conducted along a relatively long path, resulting in higher losses. This is not the case in a planar arrangement in which the individual cells are connected in a way in which the electrons only cross a minimal path, resulting in low ohmic losses and a higher power density. Disadvantages are the need for gas-tight sealing and the occurrence of thermal stresses at interfaces.

2.1.3. Performance and loss mechanisms

Without any losses, the open circuit or reversible voltage output of single fuel cell is given by:

$$E^0 = \frac{-\Delta g^0}{n_\mathrm{e}\mathrm{F}} \tag{2.1}$$

Where Δg^0 is the Gibbs free energy change of the reaction, and F is Faraday's constant which is the charge of one mole of electrons and n_e is the number of electrons released by one molecule of fuel. For a hydrogen fuel cell, the Gibbs free energy change becomes less and less negative with increasing temperature. The thermodynamic maximum efficiency (equation 2.2) decreases with temperature, on condition that Δs of the reaction is positive ($\Delta g^0 = \Delta h^0 - T\Delta s^0$), which is true for hydrogen.

$$\text{Maximum efficiency possible } = \frac{\Delta g^0}{\Delta h^0} \times 100\% \tag{2.2}$$

However, higher temperatures might still imply fewer losses in practice, and high-temperature waste heat can be used in a more efficient way. Δh^0 can be either the lower or higher heating value of the fuel, in equation 2.2 [69]. The Nernst equation provides the relationship between the theoretical output voltage, temperature, and the activities of reactants and products. For a hydrogen-fuelled SOFC where the product steam behaves as an ideal gas, the Nernst potential is given by:

$$E = E^0 + \frac{\bar{\mathrm{R}}T}{2\mathrm{F}} \ln\left(\frac{\frac{p_{\mathrm{H}_2}}{p^0} \cdot \left(\frac{p_{\mathrm{O}_2}}{p^0}\right)^{\frac{1}{2}}}{\frac{p_{\mathrm{H}_2\mathrm{O}}}{p^0}} \right) \tag{2.3}$$

A rise in system pressure will increase the voltage output [69] according to equation 2.4:

$$\Delta V = \frac{\bar{\mathrm{R}}T}{4\mathrm{F}} \ln\left(\frac{p_2}{p_1}\right) \tag{2.4}$$

In reality, the output voltage is lower than suggested by the equations above. Different loss mechanisms occur in fuel cells.

Activation losses arise due to the energy barrier that has to be overcome in (electro)chemical reactions in the electrolyte and the electrode region. In the past, these activation losses were often neglected due to the high temperatures (around 1000°C) in SOFCs. However, modern SOFC stacks tend towards lower operating temperatures, which causes the activation losses to rise to similar orders of magnitude compared to previously more dominant loss mechanisms [90]. Pressure, temperature, effective catalysts, electrode roughness, and reactant concentration all positively impact reducing activation losses [69]. The activation losses are often described by a form of the Butler-Volmer equation [31] in which it is assumed that each electrochemical reaction is "a one-step, single-electron transfer process"[90].

$$i_{\text{electrode}} = i_0 \left(e^{\beta(\frac{n_e F}{RT})\Delta V_{\text{act}}} - e^{-(1-\beta)(\frac{n_e F}{RT})\Delta V_{\text{act}}} \right) \tag{2.5}$$

i_0 is the exchange current density, β is the charge transfer coefficient. The first term dominates in high overpotential operation ($i/i_0 > 4$ [90]): Neglecting the second term simplifies equation 2.5 to the so-called Tafel equation [31]. In low overpotential operation ($i/i_0 < 1$ [90]), equation 2.5 can be linearised [31]. However, it is assumed that the magnitude of activation losses in an SOFC [14] does not allow for those approximations. β is often approximated as 0.5 in fuel cell applications [31], which simplifies equation 2.5 to a hyperbolic sine function. The Butler-Volmer is not a mathematical description of elementary kinetic processes, but it is based on empirical observations [20] and does not encompass the complex processes occurring at the TPB [20]. This research aims not to provide a detailed analysis of the electrochemical processes in an ammonia-fuelled SOFC. Despite its limitations, the Butler-Volmer equation (see chapter 3 is considered a valid way to approximate the voltage-current relationship in the system analysis conducted in this study.

Ohmic losses, proportional to the current, are related to the finite ionic and electric conductivity of the electrolyte and the electrodes, respectively. Ohmic losses [69] are simply described equation 2.6, where r is the total ohmic resistance of the fuel cell components.

$$\Delta V_{\text{ohm}} = i \cdot r \tag{2.6}$$

Concentration (or mass transport) losses occur due to the local depletion of reactants at reaction sites, which reduces the partial pressure of the gases and obstructs electrochemical reactions. Concentration losses show up especially at elevated current densities and high fuel utilisations [14]. For current densities below a certain limiting current, the effect is small, but the losses largely increase above it [31]. Chan et al. [31] propose an extensive way of mathematically describing concentration transfer losses based on Knudsen diffusion. This method is used in an often cited modelling study from Aguiar et al. [14]. It will be the concentration loss model of choice in this study; the equations are provided in chapter 3.

Fuel crossover implies the diffusion of fuel through the electrolyte, which wastes electrons. Internal current is the conduction of electrons through the electrolyte instead of through the external circuit. Both cause losses, but they are small in terms of operating efficiency in high-temperature fuel cells [69], so they are neglected in this research.

Together, the output voltage, including losses can be calculated using equation 2.7. Note that ΔV_{act} and ΔV_{con} (equation 2.7) do not represent a physical potential difference but are the difference between the case with and without losses [20]. Figure 2.3 shows a typical I-V curve. The region with low current density is dominated by activation losses. The middle, linear part is dominated by ohmic losses. Towards higher current densities, losses are dominated by mass transfer limitations.

$$V = E - \Delta V_{\text{ohm}} - \Delta V_{\text{act}} - \Delta V_{\text{con}} \tag{2.7}$$

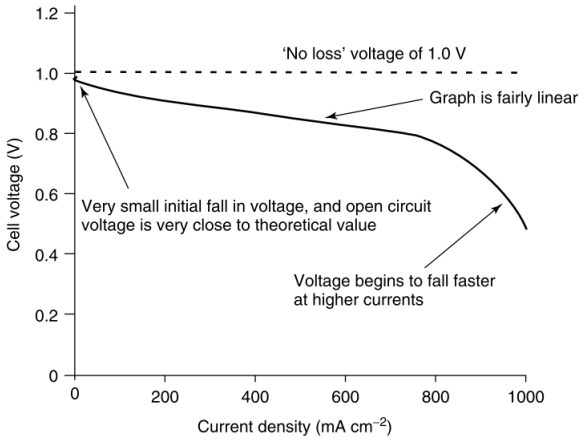

Figure 2.3: Typical I-V curve of a fuel cell operating at 800°C from Larminie and Dicks [69].

2.1.4. SOFC system and operation

The most straightforward fuel for solid oxide fuel cells is hydrogen. Hydrocarbons such as natural gas (NG) have proven to be a feasible fuel for solid oxide fuel cells as they can be easily reformed under the high-temperature conditions in the fuel cell. Despite the potential gain in efficiency compared to internal combustion engines, using hydrocarbons still results in the emission of CO_2. The complexity of storing hydrogen makes it attractive to synthesise hydrogen-rich molecules such as ammonia (NH_3) or methanol (CH_3OH) [69].

In SOFCs fuelled with hydrocarbons, the fuel has to be reformed to form a mixture of carbon monoxide (CO), hydrogen (H_2), carbon monoxide (CO_2), water (H_2O) and unreacted hydrocarbons [69]. This is a well-known, widely applied technology in the industry. Reforming can be done externally, as is the case in figure 2.4. However, endothermic reforming reactions can also take place as "internal reforming" reactions inside the SOFC stack. The required heat is then provided directly by the electrochemical reactions. Fuels such as hydrazine (N_2H_2) or ammonia are decomposed into hydrogen and nitrogen (N_2) before hydrogen is electrochemically oxidised [75]. This is called "decomposition", "cracking" or sometimes "recovery", and it may happen externally, before the fuel cell stack, or inside the fuel cell stack. As ammonia cracking is endothermic, internal cracking in the fuel cell stack may be feasible as it can make use of the available high-temperature waste heat [34]. The decomposition reaction also provides cooling.

Hydrogen is oxidised, so its partial pressure gradually declines from the inlet to the outlet of the fuel cell. From equation 2.3 one would expect a lower voltage towards the exit. Still, the voltage is approximately equal throughout the fuel cell due to the good electronic conductivity of the anode and cathode [69]. However, the current density does fall towards the exit [69] and the driving force for the electrochemical reaction diminishes towards 100% depletion. So; not all fuel can be used; a fraction stays unreacted in the outgoing anode stream. Fuel utilisation is defined by:

$$UF = \frac{\text{mass of fuel reacted in cell}}{\text{mass of fuel input to cell}} \tag{2.8}$$

Anode off-gas recirculation involves the partial recycling of the outgoing stream from the anode back to the stack [95]. This increases fuel utilisation and enhances steam reforming in the case of hydrocarbon fuel. The cracking reaction of NH_3 does not involve steam, limiting the effect of AOGR. The recycle ratio (RR) is defined as:

$$RR = \frac{\dot{m}_{\text{recirculated}}}{\dot{m}_{\text{anode,out}}} \tag{2.9}$$

A fuel cell stack is the core or an SOFC system and consists of a large number of series-connected cells to achieve a specific voltage. Large systems may include multiple stacks. An external reformer or cracker may be included in a fuel cell system in case (part of) the fuel is reformed or decomposed before entering the fuel cell stack. Heat integration in SOFC system is vital to achieving high efficiency. Preheating of reactants may be needed to and reforming or decomposition reactions usually require heat. The electrochemical reaction

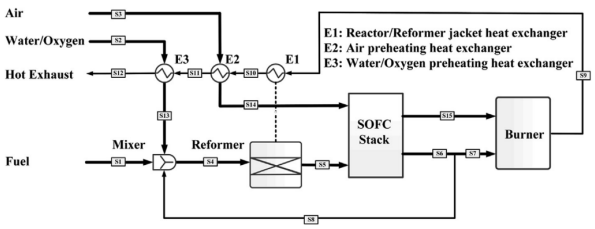

Figure 2.4: Example of an SOFC process flow diagram based on a hydrocarbon fuel [18].

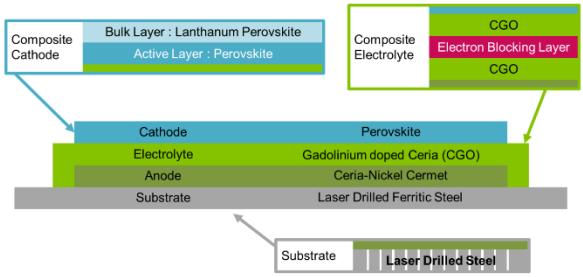

Figure 2.5: Representation of the Ceres Power SOFC [70].

produces heat, which is either lost to the environment or absorbed by the cathode and anode streams. High-temperature waste heat can be integrated with reforming or cracking processes, preheating, or be used in a downstream power cycle. 100% fuel utilisation is not possible as explained before in this section. The remaining fuel can be burned together with the cathode off-gas and used to heat the incoming flows or be directed to a downstream cycle. A DC/DC converter or an inverter (DC to AC) is used if the electrical power delivered by the SOFC is not on the desirable voltage. Blowers or air compressors supply fuel and air. They consume electric power, so influence the overall system efficiency [18]. Depending on the feedstock, pre-treatment such as desulphurisation may be necessary [69]. Figure 2.4 [18] shows an example of a process flow diagram including the stack, pre-reformer, burner and heat exchangers.

2.1.5. Commercial SOFC systems

The solid oxide fuel cell market is still immature and changing rapidly. Three manufacturers are pointed out, although many more exist.

Bloom energy installed over 350 MW of SOFC capacity in total, which makes it the largest manufacturer of SOFC systems. Its system can range from hundreds of kW to MW order size and makes use of "server modules" of 200 to 300 kW, each consisting of a large number of SOFC stacks. The NG- or biogas-fuelled system is meant to deliver a stable, highly efficient electricity supply to clients including companies such as Google, FedEx and Walmart [1, 82, 116].

Ceres Power, which partnered with companies such as Bosch and Cummins, makes use of a metal-supported (stainless steel) fuel cell (figure 2.5), operating between 500 and 600°C, which is relatively low. The stainless steel support allows for high flexibility with limited degradation. CGO is used as electrolyte material instead of the more conventional YSZ, and the system is fuelled with NG. Applications include pre-commercial combined heat and power systems for buildings [82]. According to Leah et al. [70], Ceres Power SOFCs achieve a degradation rate of less than 0.2% per 1000 hours, which is, as of now, impressive.

The Estonian-Finnish company Elcogen delivers anode-supported cells, which can operate in both fuel cell and electrolysis mode [5]. The operating temperature ranges between 600°C and 700°C and the focus of the technology is on lifetime, efficiency, low-cost materials and the ability to mass-produce in a cost-effective way [82]. They deliver individual cells or complete fuel cell stacks of 1 or 3 kW rated power that can be combined in a modular way to form large systems [5].

2.1.6. Modelling of an SOFC

Marra et al. [80] have written a book about methodologies of SOFC modelling for control and diagnosis purposes. Physical "white box" models use physical principles to make highly detailed models requiring substantial computational power. Black-box models, on the other hand, implement experimental data in a purely

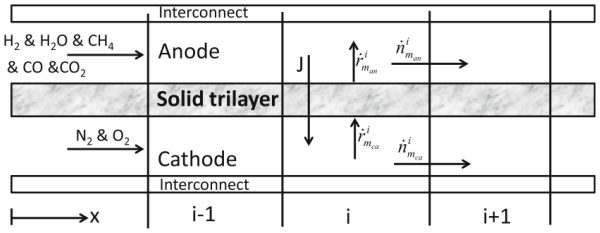

Figure 2.6: Schematic representation of a 1-D mass balance discretisation in a co-flow SOFC [80].

mathematical model. Gray box models provide a trade-off between these two, combining physical principles and experimental data. An example of these is called a 0-D, or lumped model. Black-box modelling is described by Marra et al. only in the context of neural networks, which is considered not within the scope of this research.

1-D models are relevant to analyse the spatial distribution of gas composition and temperature along the flow direction because temperature gradients are the major concern in controlling SOFCs due to the risk of excessive thermal stresses. Only a few state variables characterise the system. 1-D models provide a useful method to evaluate the performance of a fuel cell, without the need to solve variables in other directions than flow directions which, saves computation power. Marra et al. [80] propose a 1-D model which describes current, gas composition and temperature along the flow direction coordinate of a rectangular SOFC. Mass, energy and electrochemical balances are solved under a number of assumptions in each element of the discretised domain. It can be applied to either co- or counter-flow SOFCs. The mass discretisation is shown in figure 2.6.

No spatial variations are taken into account in a 0-D model, which makes them simpler than dimensional models. They are useful in system analysis, such as in a combined SOFC-gas turbine cycle when power, heat and input are important aspects [113]. Marra et al. [80] propose a 0-D model which is a fast method for predicting the dynamic response behaviour of a planar fuel cell stack. The thermal dynamics, in the order of minutes, are assumed to be dominant. Importantly, it is assumed that the trilayer temperature is uniform and represents the temperature of the entire control volume. This gives rise to the name "lumped" model. Among a number of other assumptions, the control volume is assumed to be adiabatic, so no heat is lost to the surroundings. The model then reduces to a first-order state-space model in which the outflow temperature is the only state variable. The steady-state, black-box, voltage output sub-model has been derived using a regression model with multiple variables, based on data from a 1-D model of the SOFC. The lumped SOFC model is experimentally validated and shows good agreement with reality. Cinti et al. [34] have made a 0-D model of an ammonia-fuelled SOFC, using a linear regression based on experiments conducted beforehand. The 0-D model is used in a system model to evaluate the thermodynamic behaviour of the whole system.

2.2. Ammonia as an SOFC fuel

Ammonia can be used as a fuel for SOFCs. The usual zirconia-based electrolyte of SOFCs is stable in ammonia and the common anode material nickel is a useful catalyst for ammonia decomposition [64]. Importantly, the endothermic decomposition reaction of ammonia can be integrated (directly or indirectly) with the high-temperature heat from the electrochemical oxidation of hydrogen in an SOFC.

2.2.1. Direct ammonia SOFC

In principle, ammonia can be supplied directly to an SOFC. Cinti et al. [34] argue that literature points out that all ammonia may decompose in an SOFC, and the utilisation of ammonia happens in a two-step electrochemical process. They claim no NO_x formation is reported in SOFCs. Direct ammonia SOFCs can be subdivided into SOFC-O and SOFC-H. The former involves an oxide conducting electrolyte, the latter involves a proton-conducting electrolyte. Both will be discussed below. An SOFC-O is most conventional and will be referred to as 'SOFC'.

SOFC

The conventional SOFC uses an oxide-conducting electrolyte. In [118] from Wojcik et al., a tubular SOFC with an YSZ electrolyte is used to test its reduction of ammonia in comparison to hydrogen. Almost 20 years old, this article served as a proof-of-concept, background material and a motivation for further research. It

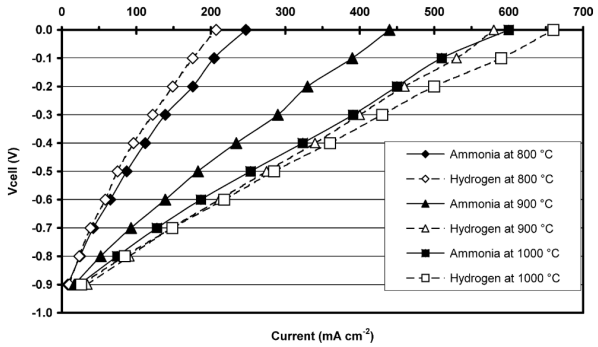

Figure 2.7: Comparison of I-V curves of hydrogen and ammonia at different temperatures [118].

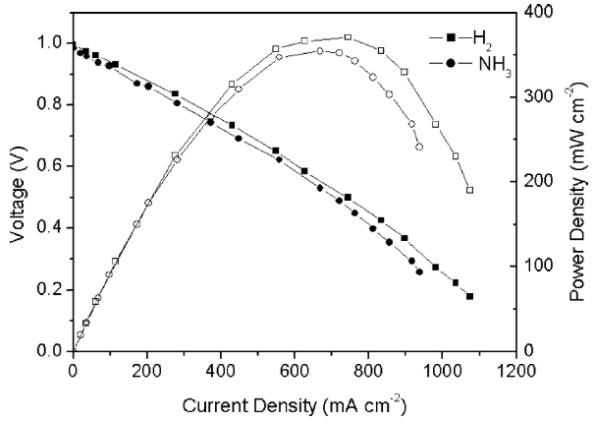

Figure 2.8: I-V (solid) and P-V curves (hollow) of hydrogen and ammonia, with pure oxygen as the oxidant [77].

is pointed out that the desired anodic reaction may be complicated by NO_x formation. First, they have carried out experiments with a silver anode at different temperatures (700°C, 800°C and 900°C). Especially at 700°C, activation losses turned out to be significant for ammonia. The voltage-current behaviour of hydrogen at 800°C is better than that of ammonia. Adding an iron catalyst leads to a great improvement of the performance of the ammonia SOFC; its I-V behaviour became comparable to hydrogen. A platinum anode shows current densities two orders of magnitude higher than in the other experiment. The results are shown in figure 2.7. However, they point out that platinum is not viable for commercialisation. Next to that, they relate using platinum to 'the problem of NO_x formation' which is not elucidated.

Ma et al. [77] report about a high-performance SOFC with a LSCO–BCGO cathode, Ni-BCGO anode and a proton conducting BCGO electrolyte, which prevents the formation of NO. Importantly, it turns out that the decomposition of ammonia is not the rate-determining step in the cell reaction, which is highlighted by figure 2.8. High current densities are obtained; also for CO_2-free air as the oxidant. CO_2 is expected to degrade the BCGO electrolyte [80].

Okanishi et al. [92] have conducted experiments with a 10-cell SOFC that is either directly fuelled by ammonia, decomposed ammonia or auto-thermally cracked ammonia. Important results are shown in figure 2.10. For increasing current, the performance of direct ammonia gradually declines compared to decomposed ammonia. At 36A, the reported efficiency of direct ammonia is 36.3% compared to 39.1% for decomposed ammonia or hydrogen. The hydrogen and direct ammonia stacks show similar degradation up to 1000 hours.

Kishimoto et al. [64] have developed a 1-kW stack as a follow-up on the study above. Again, they compare direct ammonia, external cracking and auto-thermal cracking before the SOFC stack. Direct ammonia supply results in a slightly lower output voltage than the equivalent N_2/H_2 mixture. This is due to the decrease in temperature of about 15 K as a result of the endothermic reaction. The same air flow rate has been used for direct NH_3 as for N_2/H_2. They claim that in large stacks, performance decline is due to temperature drop in the stack. At 80% fuel utilisation, a current of 50A and a power output of over 1 kW, the reported DC efficiency is 52%, but reducing the output power to a reasonable 900 W already increases the efficiency to

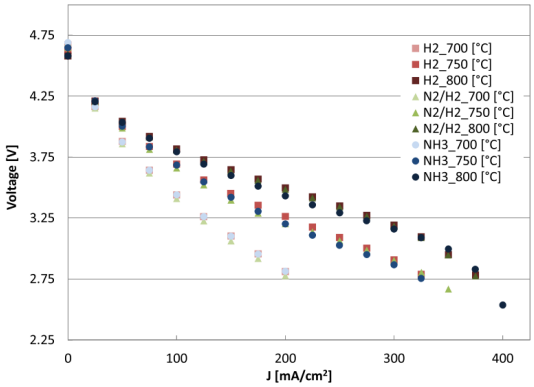

Figure 2.9: Performance of pure hydrogen, ammonia and a cracked ammonia mix [34].

55%. A 1000-hour durability test has been conducted: After a decline in output voltage, that recovered after 200 hours, stable performance is demonstrated for direct ammonia. However, material degradation is shown by microscopic images and the pressure drop increased in the durability test.

Jeerh et al. [58] explain that the difference between hydrogen- and ammonia-fuelled SOFCs is relatively small, especially towards elevated temperatures as the decomposition of ammonia will become faster. They also mention that the formation of NO_x is a risk, but can be almost eliminated when a suitable catalyst is used.

Dekker and Rietveld [39] report a 4 ppm NO_x concentration at a 1000°C exhaust temperature. At 950°C, this drops below 0.5 ppm. Standard Ni/YSZ are used and show a NH_3 conversion higher than 99.996%. A degradation rate below 1% per 1000 hours is reported in the course of a 3000 hours durability test.

Cinti et al. [34] provide very interesting material. The first set of experiments gives a detailed comparison of hydrogen, cracked ammonia (a mix of N_2/H_2) and pure NH_3 in an SOFC operating at different temperatures (figure 2.9). Importantly, the stack performance is hardly influenced by the type of fuel; polarisation curves are almost identical. Ammonia decomposition in the stack is indicated by equivalence between NH_3 and the N_2/H_2 mix. The equivalence between NH_3 and the N_2/H_2 mixture performance indicates that all ammonia is decomposed (on the condition that no direct oxidation of ammonia is taking place). The study also looks into temperature effects after introducing ammonia in an SOFC and shows, as expected, that it has a cooling effect due to the endothermic decomposition reaction. Ammonia reduces the temperature difference between the anode and the cathode, which is beneficial in terms of thermal stress. Due to reduced cooling demands, the cathode airflow decreases by roughly 30% at 800°C and open circuit operating conditions, which will positively influence the system efficiency due to the reduced air compressor power consumption. Experiments have been conducted to compare pure and diluted ammonia in water. Diluting ammonia with water reduces the stack voltage, but the heat capacity of H_2O does have a positive effect. The temperature difference between anode and cathode is reduced, and the anode temperature is lower. The experimental data is used for a thermodynamic model of the whole system. The model is used to verify that supplying pure ammonia results in a more efficient system efficiency compared to supplying the equivalent N_2/H_2 mixture, due to the reduced energy consumption from cathode air circulation.

SOFC-H

The proton conducting SOFC-H gained attention more recently. Useful information is provided in the reviews from Jeerh et al. [58] and Afif et al. [13]. The (half-)reactions and a schematic representation of the cell are shown in figure 2.11. The most important advantage is that the fuel is not gradually diluted by the formation of water, as this happens at the cathode in an SOFC-H. The current density can be higher due to the higher fuel concentration at the anode. Proton-conductors maintain good ionic conductivity at lower temperatures, which would allow for a lower temperature operation, minimising material-related design problems. NO_x formation is avoided in an SOFC-H due to the absence of oxygen at the anode. Water formation at the cathode instead of the anode will also prevent water from mixing with ammonia, which could corrode metal parts. It is claimed that the efficiency of a proton-conducting fuel cell is higher than its counterpart. However, the opposite has been stated as well in a numerical study from Ni et al. [89], contrary to what they found in an earlier thermodynamic analysis [88]. Demands to the electrolyte and electrodes are similar to those of a regular SOFC. Unfortunately, development is still in an early stage. According to Jeerh et al. [58], the highest

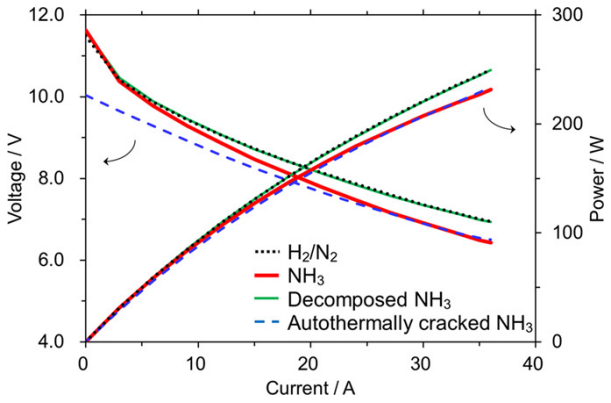

Figure 2.10: Performance of decomposed ammonia, auto-thermally cracked ammonia, and ammonia in an SOFC [92].

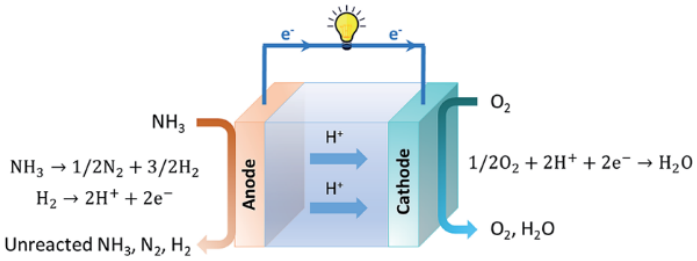

Figure 2.11: Schematic representation of an SOFC-H [58].

reported current densities have been obtained using a Pd (Palladium) anode. However, the high cost of Pd makes it unfavourable compared to Ni anodes.

Lately, research into SOFC-Hs has been conducted by Miyazaki et al. [83], where a Ni-$BaCe_{0.4}Zr_{0.4}Y_{0.2}O_{3-\delta}$ (Ni-BCZY) anode is used. Ni-BCZY fully decomposes ammonia at a temperature of 600°C which is better than Ni-YSZ and Ni-GDC as seen in figure 2.12. An experimental comparison of H_2 and NH_3 is made. Power density and output voltage of NH_3 is somewhat lower but still quite close to the power density belonging to H_2 fuel, which can be seen in figure 2.13. The authors conclude that Ni-BCZY is a suitable anode indirect ammonia SOFCs.

A Ni-BCZY anode has been used as well in an older study from Lin et al. [75]. They highlight that H_2 only outperforms NH_3 below 700°C due to the reduction in the catalytic activity of the ammonia decomposition reaction. They point out that NH_3 is first decomposed into H_2 and N_2 before H_2 is electrochemically oxidised.

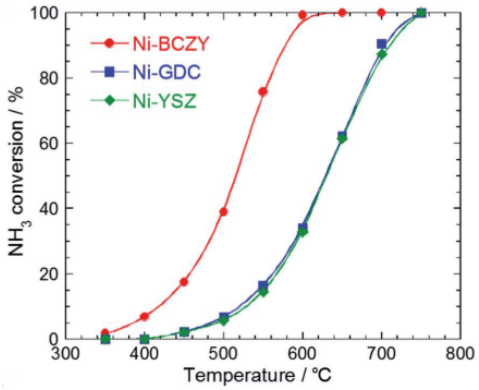

Figure 2.12: Comparison of different ceramic-metals in terms of ammonia conversion in an SOFC-H [83].

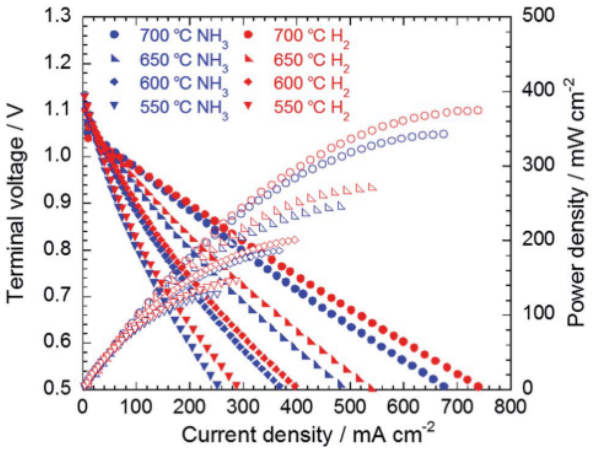

Figure 2.13: Comparison of different H_2 and NH_3 as a fuel to a single SOFC-H [83].

2.2.2. External cracking

Alternatively to fuelling an SOFC directly with ammonia, ammonia can be decomposed into hydrogen and nitrogen before the SOFC stack. This could be advantageous in case ammonia is likely to degrade the SOFC material. Ammonia cracking (recovery, decomposition) is an endothermic, catalytic process described by the following reaction [92]:

$$NH_3(g) \rightarrow 0.5\,N_2(g) + 1.5H_2(g) \quad \Delta h = 46\,\text{kJ}\cdot\text{mol}^{-1} \tag{2.10}$$

High temperature and low pressure shift the equilibrium to the decomposition side of the reaction. Boisen et al. [24] conducted experiments and highlight that the best catalysts for ammonia decomposition can be different to the best catalysts for ammonia synthesis.

Yin et al. [121] provide an overview of the ammonia decomposition reaction kinetics. They examine the performance of ruthenium, rhodium (Rh), platinum (Pt), palladium (Pd), nickel (Ni) and iron (Fe) catalysts. They also compare different support materials and promoters. It is found that under similar conditions, the conversion of ammonia over Ru is higher than over all the other catalysts. They point out that a material made of carbon nanotubes (CNTs) is the most efficient type of support material. Potassium hydroxide (KOH) is the best promotor to increase the activity of a CNT-supported Ru catalyst.

Schüth et al. [105] aim to provide a comparison of the activity of different catalysts. Again it is pointed out that Ru is the most active catalyst for ammonia decomposition. Bimetallic catalysts such as Fe on Pt and cobalt (Co) on Pt could be promising and have been tested experimentally. However, they might not be suitable at the high temperatures involved in an industrial decomposition process. The lower price of iron-based catalysts could make them feasible compared to ruthenium, despite their lower activity. The same cost advantage is true for nickel, which still shows relatively high catalytic activity for ammonia decomposition. Catalysts such as molybdenum nitride, which have been studied less extensively, seem to be less active and the costs will be in the same order as ruthenium catalysts. The article states that a temperature of at least 650 K (377°C) is required to produce pure hydrogen from ammonia, which would be well possible in SOFC systems.

Okanishi et al. [92] have experimentally tested an ammonia decomposition reactor in the context of an SOFC where they compared a Ni/Y_2O_3 catalyst with a $SrO–Ni/Y_2O_3$ catalyst. The results are shown in figure 2.14. Relatively high conversion is obtained at moderate temperatures, with full conversion at 650°C, which implies ammonia decomposition could be possible without external heating.

In the follow-up study of a 1-kW stack [64], similar experiments were conducted with a newly developed BaO/Ni/Sm2O3/MgO catalyst and showed improved results indicating that an external ammonia cracker could be operated at lower temperatures. In the stack itself, the reported difference in performance between N_2/H_2 mixture and externally cracked NH_3 is small. The durability of an external cracker has been tested up to 1000 hours; a slight decline in conversion is seen in the graph, but no thorough explanation is provided. The performance of the stack fuelled with pre-decomposed ammonia showed stable performance during the 1000 hour test.

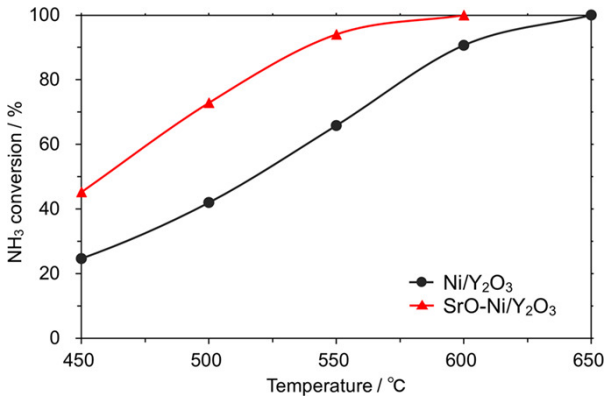

Figure 2.14: Comparison of ammonia decomposition catalysts [92].

2.2.3. Auto-thermal cracking

Okanishi et al. [92] tested an auto-thermal cracking process over a Co–Ce–Zr catalyst. In auto-thermal cracking, the oxidation of ammonia (exothermic) is combined with the decomposition of ammonia (endothermic). Therefore, part of the fuel is consumed before entering the SOFC, which immediately is a major drawback: Auto-thermal reforming results in low electrical efficiency. The advantage is that the heat from the oxidation could be useful to start up an SOFC system. With the reaction:

$$NH_3(g) + 0.095O_2(g) \rightarrow 0.5N_2(g) + 1.31H_2(g) + 0.19H_2O(g) \quad \Delta h = 0\ \mathrm{kJ \cdot mol^{-1}} \tag{2.11}$$

a thermo-neutral (Δh=0) reaction is obtained. Considering SOFC-Hs, the appearance of water at the anode in the case of an auto-thermal cracker could reduce the advantages of an SOFC within the context of NO_x formation and corrosion.

A 1-kW follow up study [64] evaluated auto-thermal reformed ammonia as a fuel. They claim that the presence of steam and nitrogen does not affect the output voltage. Nevertheless, a similar output voltage is reported for a higher consumption of NH_3: Although they do not state it explicitly, auto-thermal reforming should have a negative impact on fuel efficiency.

2.2.4. Concluding remarks about ammonia-fuelled SOFCs

Studies have pointed out that ammonia is a feasible fuel for an SOFC. Figure 2.15 shows three important design choices that have been discussed. Supplying ammonia directly to a fuel cell has a limited effect on the performance of the stack compared to an equivalent H_2 supply. For the system efficiency, direct ammonia is beneficial as the endothermic decomposition is directly combined with the exothermic electrochemical reaction. It could also limit system complexity. External cracking of ammonia into hydrogen and nitrogen before entering the stack may be beneficial for the long-term stability of the SOFC in terms of material degradation. However, degradation is seen in an external cracker as well. Auto-thermal cracking, in which part of the heat of oxidising ammonia is used to decompose ammonia, may be helpful for system start-up but negatively impacts electric efficiency. SOFCs can be subdivided into two types: Proton conducting SOFCs (SOFC-Hs), and oxide conducting SOFCs (SOFC-O, or, in this report, SOFCs). SOFC-Hs seem very promising in terms of performance due to the increased ionic conductance of the electrolyte and the formation of water at the cathode instead of the anode. NO_x formation in the SOFC-H will be limited due to the absence of oxygen at the anode. Nevertheless, SOFC-H research is still in an early phase, and more extensive research has been done on ammonia SOFCs. Diluting ammonia was briefly discussed: The heat capacity of water in diluted ammonia reduces temperature gradients but has a negative effect on the output voltage. In this research:

- Pure ammonia will act as the SOFC system fuel as there is no definite reason to choose diluted ammonia.
- Both direct ammonia (internal cracking) and external cracking will be analysed. Auto-thermal cracking is not incorporated because of the expected (negative) impact on system efficiency.
- An oxide conducting SOFC is the technology of choice as SOFC-Hs are regarded too immature.

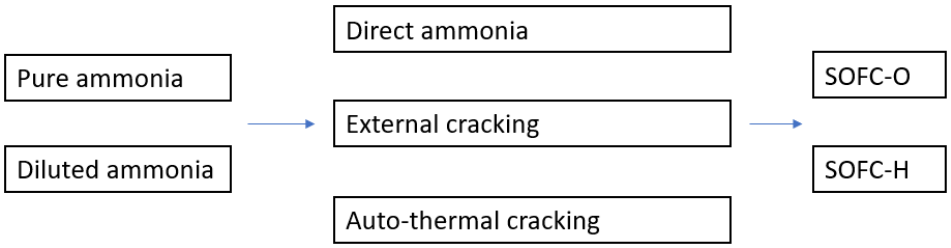

Figure 2.15: Design choices of an ammonia SOFC system.

2.3. Internal combustion engine

In an internal combustion engine (ICE), chemical energy is first converted into thermal energy through the combustion of fuel and oxygen from the air. Then, thermal energy is converted into mechanical energy on pistons connected to an output shaft.

2.3.1. Ignition types

Heywood [54] and Stapersma [109] provide useful background theory of ICEs. A diesel engine named after Rudolf Diesel, makes use of compression ignition (CI). Fuel is injected in compressed air and ignites due to the high temperature of the air. In a spark ignition (SI) engine, fuel and air are pre-mixed and ignited by means of a spark. The fuel must be vaporised and mixed well with the fuel. Usually, CI engines have a much higher compression ratio as the temperature increase in the compression stroke should be enough to ignite the mixture of fuel and air, while a SI engine should not facilitate auto-ignition. Gasoline, a mixture of light hydrocarbons, is the most important fuel for SI engines. It is suitable for SI engines due to its volatility and good resistance to auto-ignition (knocking). Its anti-knock resistance is expressed as the "octane number". Diesel fuels are a mixture of denser and higher boiling hydrocarbons compared to gasoline. Diesel fuel must have auto-ignition characteristics suitable for a CI engine, for which it is the main type of fuel. The auto-ignition characteristics in diesel fuels are expressed as the 'cetane number'. Natural gas, having bad ignition characteristics [109], can be used directly in an SI engine [67], or used in a CI engine by using an ignition aid (dual-fuel) [109].

More recently, homogeneous charge compression ignition (HCCI) gained attention. HCCI can be explained as a combination between CI and SI. Fuel and air are premixed as in an SI engine, but the fuel auto-ignites due to compression heat. Combustion is initiated simultaneously at different sites in the cylinder, so there is no clear propagating flame front in contrast to CI engines. High efficiency and low NO_x emission are important advantages, but challenges include the auto-ignition timing, the operating range, mixture preparation and cold start [120].

The dual-fuel concept of reactivity controlled compression ignition (RCCI) could be a way to have better control over the combustion process compared to HCCI. A low reactivity fuel, for example, ethanol, gasoline or ammonia, is mixed with air and compressed without reaching auto-ignition [99]. A high reactivity fuel such as diesel or hydrogen is introduced with one or more injections directly into the combustion chamber, triggering combustion.

2.3.2. Two-stroke and four-stroke engines

Most engines operate in a four-stroke cycle (figure 2.16), in which the cylinder requires four strokes, or two revolutions of the crankshaft, to obtain one power-producing stroke [54, 84]:

1. Intake stroke: From the highest point of the piston (top dead centre, TDC), the intake stroke starts. The piston moves down, and the cylinder fills with air (CI) or an air/fuel mixture (SI). The air intake closes near the bottom dead centre (BDC).

2. Compression stroke: Air (CI) or an air/fuel mixture (SI) is compressed as the cylinder moves upwards between the BDC and the TDC. The gases reach a high temperature due to compression. In CI, fuel injection in the compressed air triggers combustion. In the case of SI, a spark initiates the combustion of the air-fuel mixture.

3. Working stroke: After the piston reaches the TDC, the high pressure, high-temperature combusted gas in the cylinder expands, exerts work and moves the piston down towards the BDC. The exhaust valve

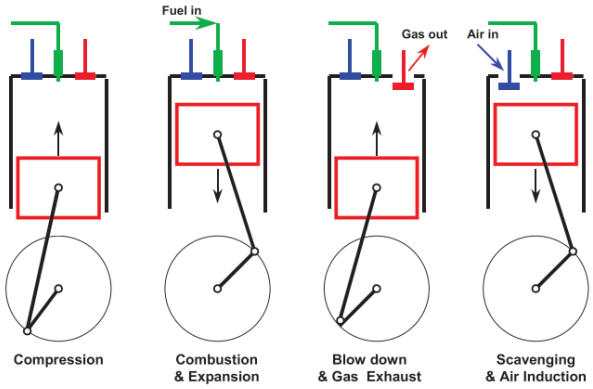

Figure 2.16: 4-stroke diesel engine principle [109].

opens before reaching the BDC, causing a portion of the combustion gas to leave during blow-down.

4. Exhaust stroke: Most combustion gas exits when the piston moves back to the TDC. Near the TDC, the inlet valve opens, allowing air into the cylinder. The remaining combustion gas may be removed from the cylinder in a scavenging process if pressurised air is fed to the cylinder. The exhaust is closed just after the TDC.

The compression, combustion and expansion part of the four-stroke process, when the inlet and exhaust valves are closed, is the closed cylinder process. The process between opening the exhaust valve, and closing the inlet valve, is the gas exchange process [54].

A two-stroke process only requires one revolution for compression, combustion, expansion, blow-down and scavenging. The exhaust valve opens earlier, well before the BDC. Still before the BDC, and after blow-down finishes, the air inlet opens. Around the BDC, a scavenging process introduces fresh air and pushes combustion gases out simultaneously [54]. A two-stroke has a working stroke per revolution instead of two revolutions, but is not two times as powerful as a four-stroke engine. The working stroke is less effective, and residual combustion gas may remain in the cylinder due to inefficient scavenging [109]. This results in a lower mean effective pressure (p_{me}) compared to 4-stroke engines. Most large ships use two-stroke diesel engines: The relatively simple two-stroke engine can use cheap, low-grade fuel (which cannot be used in medium speed 4-stroke engines) to achieve efficient operation [91, 108]. Next to that, the typical slow rotational speed of large two-stroke engines [109] allows for a direct connection to the propeller shaft without a gearbox [91, 108]. The low rpm could make them more suitable for ammonia than medium-speed 4-stroke CI engines due to the slow combustion of ammonia [124]. 2-stroke SI engines are undesired as the overlap between fuel/air inlet and exhaust results in excessive unburned fuel emission [53]. This is highly unwanted in the case of ammonia.

2.3.3. Turbocharging

Marine engines are nearly always turbocharged [109]. Air is compressed before it enters the engine, which increases the mass of oxygen per unit volume of air entering the engine, increasing the amount of fuel that can be combusted. The air compressor is powered by a gas turbine expanding hot exhaust gases. The turbine-compressor combination is called the turbocharger. Usually, the air is cooled after the compressor in an intercooler to increase its density further.

2.3.4. Important parameters

This section lists a number of parameters, taken from Stapersma [109] and Heywood [54].

The clearance volume, V_{TDC} is the minimum cylinder volume. This is when the piston is at the TDC. The maximum cylinder volume occurs at the BDC: V_{BDC}. The difference between V_{BDC} and V_{TDC} is the swept or displaced volume V_{s}. Equation 2.12 defines the geometric compression ratio. The inlet valve normally closes after BDC, which gives rise to an effective compression ratio, equation 2.13. x is the compression stroke effectiveness factor, which depends on the valve timing.

$$\epsilon = \frac{V_{\mathrm{BDC}}}{V_{\mathrm{TDC}}} = \frac{V_{\mathrm{TDC}} + V_{\mathrm{s}}}{V_{\mathrm{BDC}}} \tag{2.12}$$

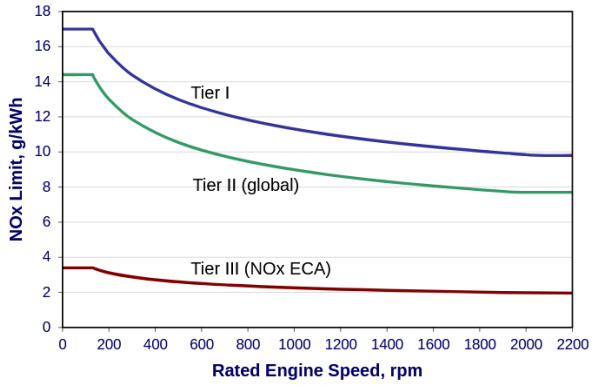

Figure 2.17: NO_x emission limits set by the International Maritime Organisation in MARPOL Annex VI [3].

$$r_c = x \cdot \frac{V_S}{V_{TDC}} + 1 \tag{2.13}$$

The specific fuel consumption, equation 2.14, is the fuel consumption per unit of brake power. The efficiency (equation 2.15) is the power output relative to the energy content (higher or lower heating value) of the fuel.

$$bsfc = \frac{\dot{m}_f}{P_b} \tag{2.14}$$

$$\eta_e = \frac{P_b}{\dot{Q}_f} = \frac{P_b}{\dot{m}_f \cdot \Delta h_f^0} \tag{2.15}$$

The reversible work of an expansion stroke is the integral of the pressure over the volume. This can be replaced by the work of a mean pressure times the stroke (or displacement) volume. The brake mean effective pressure, p_{me} is defined by equation 2.16. k is the number of revolutions per cycle (2 in four-stroke engine), i is the number of cylinders, and N is the number of revolutions per second

$$p_{me} = \frac{P_b \cdot k}{i \cdot V_d \cdot N} \tag{2.16}$$

The stoichiometric air-fuel ratio (equation 2.17) is the ratio between the theoretical minimum mass of air needed for complete combustion per unit mass of fuel. Similarly, the air-to-fuel ratio (equation 2.18 is the available air per unit mass of fuel. The air excess ratio, (equation 2.19) is the ratio between these two and must be at least higher than unity to prevent incomplete combustion.

$$\sigma = \frac{m_{air,minimum}}{m_f} \tag{2.17}$$

$$afr = \frac{m_{air}}{m_f} \tag{2.18}$$

$$\lambda = \frac{afr}{\sigma} \tag{2.19}$$

The most important emissions from marine diesel engines include CO_2, SO_2, CO, unburned hydrocarbons and NO_x. As this research will focus on ammonia as a fuel, mainly NO_x emission is an important point of attention. The strictest regulations, Tier III, shown in figure 2.17, often require special NO_x removal techniques. Tier III limits cover NO_x Emission Control Areas (e.g. the North Sea), whereas Tier I and II apply globally [3].

2.3.5. Modelling of an ICE

The most complex ICE models include detailed multidimensional methods. For example, Baratta et al. [19] use a three-dimensional engine model in combination with experiments to optimise the pressure ratio and to analyse the effect of the cylinder head geometry. This is, however, more suitable for component design than for system analysis due to its high computational demand.

Table 2.1: Six-stage Seiliger process [109].

Stage	Description	Seiliger parameter	Seiliger definition
1–2	Polytropic compression	$r_c = \frac{V_1}{V_2}$	$\frac{p_2}{p_1} = r_c^{n_c}$
2–3	Isochoric (constant-volume) combustion	$a = \frac{p_3}{p_2}$	$\frac{V_3}{V_2} = 1$
3–4	Isobaric combustion	$b = \frac{V_4}{V_3}$	$\frac{p_4}{p_3} = 1$
4–5	Isothermal combustion and expansion	$c = \frac{V_5}{V_4}$	$\frac{T_5}{T_4} = 1$
5–6	Polytropic expansion	$r_e = \frac{V_6}{V_5}$	$\frac{p_5}{p_6} = r_e^{n_e}$
6–1	Isochoric (constant-volume) heat rejection	–	$\frac{V_6}{V_1} = 1$

At a lower level of complexity than multidimensional modelling, one could divide the combustion zone of an ICE into one, two, or multiple zones [102]. A multi-zone ICE model as the one from Rakopoulos and Michos [98], where a syngas-fuelled SI engine is modelled, is very useful for predicting NO_x emissions due to the strong (local) temperature dependency of NO_x formation. Although the multi-zone model is claimed to be 0-D by the authors, it still provides information in space.

An example of a grey-box 0-D model is the "Mean Engine Value Model" for SI engines from Hendricks and Sorenson [52]. Their model exists of three dynamic sub-models of the fuel inflow, rotational speed of the crankshaft and the inlet manifold pressure. Although this model is very useful for dynamic control applications, aspects such as thermal efficiency are required as an input, which requires additional experiments or models.

The Seiliger model is a useful method for predicting engine performance based on the thermodynamic cycle, as shown in table 2.1 and figure 2.18 [109]. Parameters a, b and c describe the combustion process. The compression and expansion processes are described by the effective compression and expansion ratios, r_c and r_e, together with the polytropic exponents n_c and n_e. After defining the full cycle, the specific work per stage can be calculated. Often, the Seiliger process is referred to as a 5-point dual (combustion) cycle where the isothermal combustion–expansion stage (4–5) is removed. Sapra et al. [102] and Reurings [100] have used the 6-stage Seiliger model to simulate a NG-fuelled engined in the context of an SOFC–ICE hybrid system. The Seiliger model turns out to accurately capture the combustion process. However, it relies on experiments to determine the a, b and c Seiliger parameters and to the best of the author's knowledge, an extensive data-set on an NH_3-fuelled ICE is unavailable.

0-dimensional Wiebe functions are methods to predict the combustion process in terms of burn rate and mass fractions of various engine types. They are widely used in engineering as they are relatively simple techniques to predict the mass fraction burned during the combustion process [76]. The single Wiebe function computes the mass fraction burned as a function of crank angle. The double Wiebe function provides an extension on the single Wiebe function to account for different burn rates in advanced combustion strategies [76]. The heat release can then be used to predict the in-cylinder pressure as a function of crank angle. It is said to be the most useful model in engine research when a simple and computationally efficient model is desired [48]. Sapra et al. [102] compare the Seiliger model with a Wiebe function approach. The Wiebe approach is claimed to be slightly less accurate.

Park et al. [93] analyse and compare a NG-fuelled SOFC–ICE hybrid system with an HCCI-type engine. The authors model the engine as a simple 4-stage Otto cycle, which they justify by claiming that combustion in an HCCI engine can be assumed to be isochoric. On condition that the Otto cycle is a valid approximation, the relative simplicity of this approach seems very useful for the analysis of an integrated system. Also Blarigan [23] claim that the Otto cycle can be approached using HCCI. They fuelled pure ammonia to a free-piston linear generator in their experiments. It is unclear how well their free-piston linear generator can be modelled with an ideal Otto cycle. Apart from that, the question arises how their free-piston linear generator compares to a conventional internal combustion engine.

2.3.6. Marine power plants

The ultimate purpose of a marine power plant is to supply power for propulsion and auxiliary systems. In his PhD thesis, Van Biert [21] formulated a number of characteristics defining the suitability of a power plant for a marine application. The performance of a marine propulsion system can be expressed in the system properties below [21].

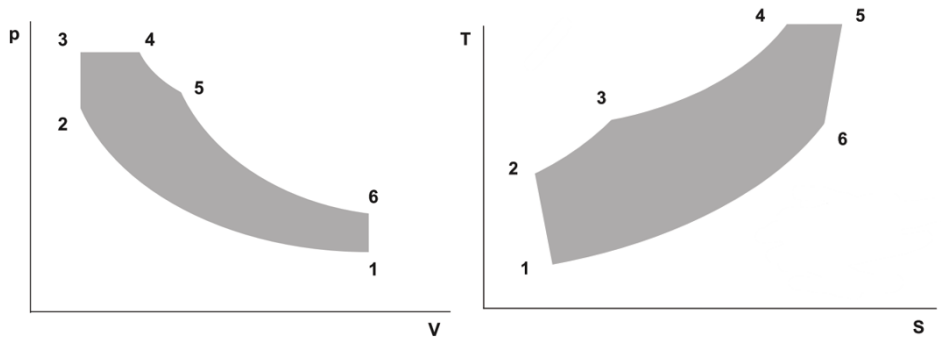

Figure 2.18: Seiliger P-V and T-S diagram [109].

- Electrical efficiency
- Power and energy density
- Load transients and system start-up
- Environmental impact
- Safety and reliability
- Economics

2.4. Ammonia as an ICE fuel

2.4.1. Internal combustion of ammonia using a promoter fuel

Zamfirescu and Dincer [122] claim that it is possible to use ammonia in a HCCI type ICE. Due to the low flame temperature, low laminar flame speed, high ignition energy and narrow flammability limits, pure ammonia is unsuitable for conventional ICEs. This problem can be avoided by mixing ammonia with a "promoter fuel" enhancing combustion. As the fuel utilisation in an SOFC is never 100%, hydrogen in the off-gas may be used as a promotor fuel in an ICE in an integrated SOFC–ICE system. Ammonia can also be used in catalytic reduction of NO_x in the exhaust gas as will be explained the next subsection.

Frigo and Gentili [46] analysed the influence of the composition of ammonia-hydrogen mixtures on the performance of a 4-stroke twin-cylinder SI engine of 505 cm^3, which is part of a range extender in an electric vehicle. The authors point out that previous research showed that the addition of roughly 1 wt% (8 vol%) hydrogen allows satisfactory combustion characteristics. The lower limit of added hydrogen is determined by the coefficient of variation of the indicated mean effective pressure COV_{IMEP}. The COV is also known as the relative standard deviation. Generally, it is considered that the allowable COV_{IMEP} is 10%. The relative amount of hydrogen is expressed in the hydrogen to ammonia energy ratio (HAER). Figure 2.19 shows that below 6-7% HAER, COV_{imep} sharply increases, which indicates an approximate minimum HAER of 7%. 1700 ppm ammonia in the exhaust is reported at full load and 3000 rpm.

As part of the same large scale project, Comotti and Frigo [37] use a ruthenium catalyst-based external cracker, recovering hydrogen from ammonia and feeding it to the same ICE as described in the previous paragraph. The cracker requires electric heat during start-up, or heat from the exhaust during ICE operation, as the decomposition of NH_3 is endothermic. The efficiency of the NH_3/H_2-fuelled ICE is reported to be at least comparable to the efficiency of the original gasoline version. NO_x formation values between 3000 and 5000 ppm are reported and depend on rotational speed, air/fuel ratio, load and the quantity of injected hydrogen. The authors claim NO_x formation is not a problem; it does not exceed the emission from gasoline and NO_x can be effectively reduced with Selective Catalytic Reduction (SCR) using ammonia.

Dimitriou and Javaid [41] claim that they are the first ones to provide a complete overview on using ammonia in CI engines. First, they provide an overview of previous research on ammonia in IC engines and summarise that ammonia is a feasible fuel for SI engines due to the high octane number. They point out that dual-fuel combustion of ammonia in CI engines is complex due to the auto-ignition resistance of ammonia, but it is still a feasible option in marine, power generation and heavy duty applications. Other challenges than auto-ignition resistance, are unburned ammonia emission, declining with fast-burning promoter fuels,

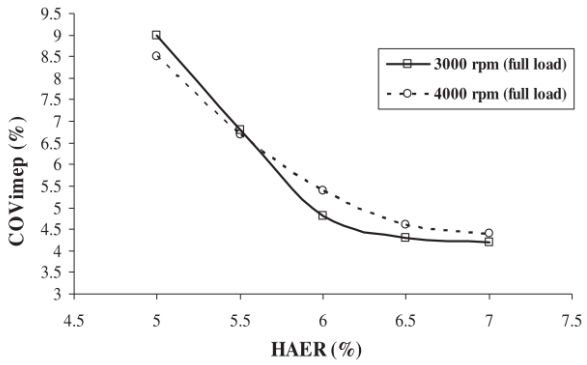

Figure 2.19: Coefficient of variation of the indicated mean effective pressure versus the hydrogen to ammonia energy ratio [46].

and the optimisation of injection. Also, reduction techniques for exhaust NO_x will have to be implemented in an ICE system. A large portion of their review is about hydrocarbon promoters (which is considered beyond the scope of this research).

Dimitriou and Javaid refer to research from Pochet et al. [96], who test a 499 cm^3 HCCI type ICE (r_c=15.3) with different hydrogen/ammonia blends. From their experiments, they conclude that the engine could operate with up to 70 vol% ammonia without the occurrence of ringing, at an intake pressure of 1.5 bar and an intake temperature of 475 K. Ringing occurs in HCCI engines and involves in-cylinder pressure oscillations leading to combustion noise or even damage to engine parts [81]. Exhaust gas recirculation (EGR), which means part of the exhaust gas is returned to the engine, reduces NO_x formation (up to 3500 ppm without EGR) but has little effect on N_2O formation up to a very large EGR.

In his MSc thesis at TU Delft, Zheng [124] worked on modelling HCCI hydrogen-ammonia combustion in ICEs. About hydrogen/ammonia SI ICEs, he summarises that they are inefficient, have low power densities and emit unburned fuel. CI engines on the other hand, show much NO_x formation. This gives rise to HCCI engines as a useful alternative, on the condition that a control system can adequately deal with changing conditions which affect auto-ignition. Switching to a different ignition type may be necessary under conditions including start-up and high load. Zheng reports stable operation between 31 vol% and 47 vol% hydrogen. As there was no data present from marine engines, he estimated the power output of a marine sized engine by scaling the output data from an automotive sized engine from Pochet et al. [96].

2.4.2. Selective catalytic reduction

Combustion control methods could reduce NO_x emission from an ammonia-fuelled engine, but likely not to levels meeting Tier III levels. Literature points out that an ammonia ICE system should be equipped with SCR. A clever solution is to use onboard ammonia as the reducing agent. According to Brandenberger et al. [27], the main reaction taking place in diesel engine SCR is 2.20, as NO is the main NO_x fraction. In presence of a large NO_2 amount, reaction 2.21 dominates. In emerging technologies such as EGR and HCCI, more NO_2 is formed, which is reduced according to reaction 2.22. Reaction 2.23 can normally be neglected in lean mixtures, as the reaction is slow and plenty of oxygen is present.

$$4NH_3 + 4NO + O_2 \rightarrow 4\ N_2 + 6H_2O \tag{2.20}$$

$$4NH_3 + 2NO + 2NO_2 \rightarrow 4\ N_2 + 6H_2O \tag{2.21}$$

$$4NH_3 + 3NO_2 \rightarrow 3.5\ N_2 + 6H_2O \tag{2.22}$$

$$4NH_3 + 6NO \longrightarrow 5\ N_2 + 6H_2O \tag{2.23}$$

According to Mørch et al. [85], reaction 2.20 is exothermic and takes place between 600 and 700 K, avoiding the need for reheating the exhaust gas. They stress that the main challenge in SCR is to avoid the emission of NH_3 (ammonia slip).

2.4.3. Pre-commercial ammonia ICEs

No commercial ammonia marine engines are available as of 2021. MAN B&W [79] announced that they are developing a two-stroke ammonia dual-fuel CI ICE resulting from the modification of the an engine type that

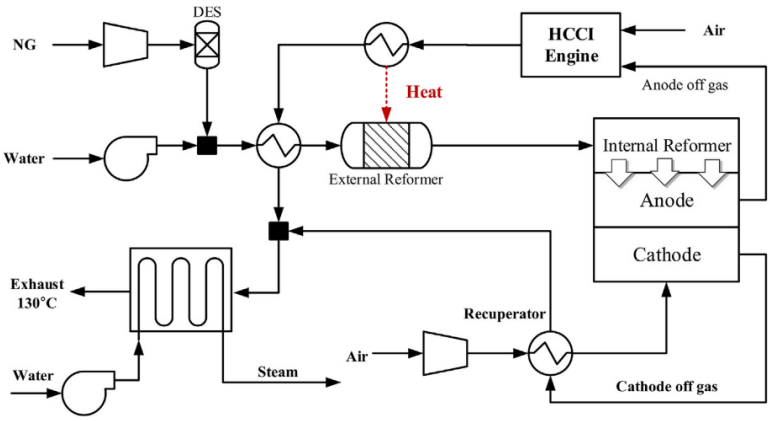

Figure 2.20: SOFC-HCCI hybrid system layout from Park et al. [93].

can run on LPG or methanol. This engine type, with a "specified maximum continuous power range from 4,350 kW to 29,120 kW" [78], has been available for orders since 2018. The ammonia version will be equipped with SCR to reduce NO_x emissions. MAN explains that hydrogen or dimethyl ether can replace the use of pilot oil as the promoter fuel. In 2019, MAN wrote that the development of the ammonia engine would take two to four years from then [79]. In 2020, Wärtsilä [10] announced that it will conduct the first long-term tests with an ammonia-fuelled four-stroke ICE in the first quarter of 2021. In July 2021, Wärtsilä reported that test results with 70% ammonia (the remaining 30% specified) were promising, and they succeeded in testing an engine with 100% hydrogen fuel [11]. Wärtsilä expects to complete an ammonia dual-fuel ICE power plant suitable for the maritime market in 2021; the pure ammonia equivalent will be ready by 2023 [11].

2.5. Hybrid SOFC–ICE system

Mainly SOFC–GT hybrid systems gained attention during previous years. Van Biert et al. [22] provide a comprehensive thermodynamic comparison of different types of SOFC- combined cycles. They state SOFC-GT integration is preferred at "low fuel utilitsations, moderate cell voltages and high stack temperatures". For "low temperature, higher voltage", integrating a steam turbine cycle is more attractive [22]. However, gas turbines appear to be less efficient and less cost-effective below multi-MW power scales [32]. An ammonia-fuelled SOFC–ICE hybrid system is a promising marine propulsion system as proposed by De Vos [38] in *SWZ maritime*. The system could exhibit high efficiency and simultaneously meet the functional requirements of a marine application. As explained in chapter subsection 2.1.4, SOFC fuel utilisation is never 100%. Thus, remaining hydrogen from the SOFC can be used as a promoter fuel in an ammonia-fuelled ICE. Excess heat from the SOFC stack can be usefully integrated with the endothermic decomposition reaction to increase the efficiency of the system. Furthermore, ammonia can be used in an SCR system.

Useful background material about an SOFC–ICE hybrid system is provided by Park et al. [93] in an article shortly mentioned in subsection 2.3.5. By means of simulations, they analyse and compare three NG-fuelled systems:

1. A regular SOFC system with a 100 kW class stack in which the anode-off gas (resulting from 75% fuel utilisation) is burned in a catalytic combustor after the SOFC. Half of the NG fuel is reformed in an external reformer, before the SOFC stack. Heat exchangers, blowers and heat exchangers are also incorporated in the model.

2. An SOFC–GT hybrid system in which a small gas turbine, using heat from combusted off-as, replaces the cathode air blower and delivers additional power.

3. An SOFC–ICE hybrid system (figure 2.20) in which an HCCI type ICE replaces the catalytic combustor present in system 1.

The SOFC–ICE hybrid system exhibited a 59.5% electrical efficiency, 1% higher than the SOFC–GT system and 8% higher than the regular SOFC system. Most interestingly, it gives an extensive explanation of the way the system has been modelled (in Aspen Plus) using a lumped (0-D) stack model and an Otto cycle to model the

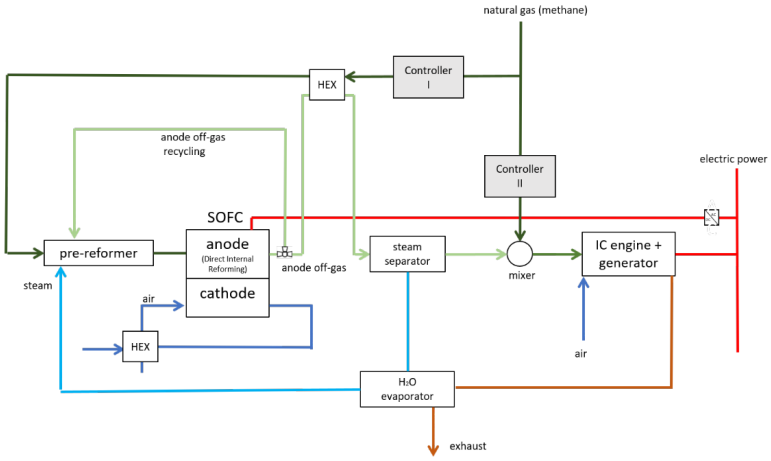

Figure 2.21: The proposed NG-fuelled SOFC–ICE hybrid system layout from Reurings [100].

HCCI ICE. In a comparable study from Choi et al. [32], where a 1-D SOFC model is used, similar conclusions are drawn.

The same research group as in [93] conducted a follow-up study aimed at developing a dynamic model (in MATLAB & Simulink) of a NG-fuelled SOFC–ICE hybrid system that can be used to develop control strategies for SOFC–ICE hybrid systems [60]. The SOFC stack is modelled quasi-3D; the external reformer and the heat exchangers 2-D and the ICE and blowers 0-D. The sub-models are experimentally verified. Results indicate that the dynamic behaviour is dominated by the SOFC stack and that the engine power mainly depends on the output variation of the stack [60].

However, in all mentioned studies, the ICE delivers less than 20% of the output power as it is fuelled only by anode off-gas (a bottoming cycle). According to De Vos [38], a power split favouring the ICE output, although less efficient, is most feasible in terms of capital expenditures, weight requirements and dynamic operability in marine applications. This has been addressed by Sapra et al. [103]. They analysed a hybrid SOFC–ICE system in which anode off-gas from an SOFC is used to promote combustion in a dual-fuel hydrogen-NG SI marine engine. The integrated model involves a 0-D SOFC model and a validated mean value engine model of the ICE. The system performance is verified at different SOFC/ICE power splits, current densities, fuel utilisations and pre-reforming ratios. The latter shows similarities to the degree of ammonia decomposition before the SOFC, which has been described in chapter 2.2. An equal power split (50–50) between the ICE and the SOFC with 750 kW electric power output, at a fuel utilisation of 85%, indicated an efficiency increase of 7.2 percent points compared to a conventional ICE system. In the situation where the ICE delivers 67% of the total power, the efficiency increase is 5% points compared to the conventional system. NO_x emissions drop by 60% (50–50 power split case) or 30% (33–67 SOFC–ICE power split case).

With his MSc thesis project [100], Reurings made important contributions to the aforementioned project from Sapra et al.. His thesis will serve as useful reference material in the present study. The proposed SOFC–ICE hybrid system is depicted in Figure 2.21.

In this study, an SOFC–ICE fuelled with ammonia in stead of NG will be investigated. Ezzat and Dincer [43] conducted an energy and exergy analysis of an ICE system and an ICE–PEMFC (Proton electrolyte membrane fuel cell) hybrid system for vehicular applications, fuelled with ammonia. This shows that the idea of a ammonia-fuelled combined ICE–FC system is not entirely new. Nevertheless, the study does not use an SOFC and parts of the article such as a 62% efficiency of the ammonia ICE system (without an FC) seem not credible. Ammonia SOFC–GT systems for rail applications have been studied by Al-Hamed and Dincer [15, 16]. Zheng conducted his MSc thesis; *An investigation of hydrogen-ammonia combustion inside internal combustion engines*, with the ammonia-fuelled SOFC–ICE hybrid system from De Vos [38] in mind. He focused on the ICE and did not perform a system analysis of an ammonia SOFC–ICE hybrid system.

3

Methodology

A system model of the ammonia-fuelled SOFC–ICE hybrid system has been developed in MATLAB & Simulink, of which the ultimate goal is to assist in answering the research questions in chapter 2. Section 3.3 will show how the SOFC and ICE systems are combined in the hybrid system model. Before this, the SOFC system model, based on a number of 0-dimensional sub-models, will be elucidated in section 3.1. The sub-models included in the ICE model are clarified in section 3.2.

3.1. Solid oxide fuel cell system

The dynamic solid oxide fuel cell model consists of a number of sub-models, as shown in figure 3.1.

- Mass balances of the anode and cathode incorporate the hydrogen oxidation reaction and the ammonia decomposition reaction. A temperature controller adjusts cathode airflow.
- The dynamic energy balance is a lumped model solving for the outlet temperature.
- The electrochemical model computes the no-loss voltage and subtracts activation, concentration and ohmic losses based on the stack temperature and partial pressures of the gases.
- The iso-thermal external decomposition reactor (cracker) model computes the required inlet flow of fuel and the heat required to crack 0 to 100% of the incoming ammonia to hydrogen and nitrogen. It also calculates how much extra fuel has to be cracked and burned to heat the cracker.
- The heat integration model checks whether heat exchanges can pre-heat fuel and air to stack inlet conditions through heat recovery.
- The output model calculates the power output, efficiencies, fuel consumption.

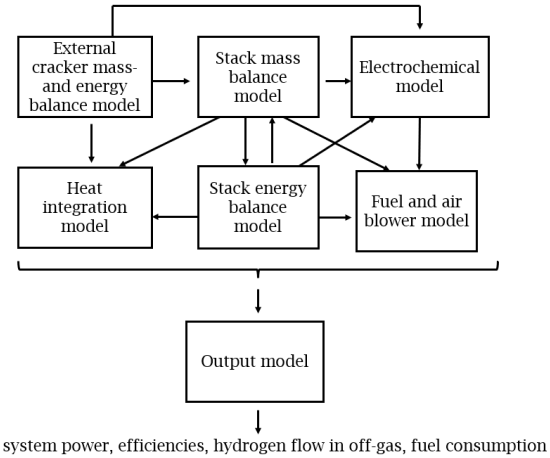

Figure 3.1: Structure of the SOFC system model developed in MATLAB & Simulink.

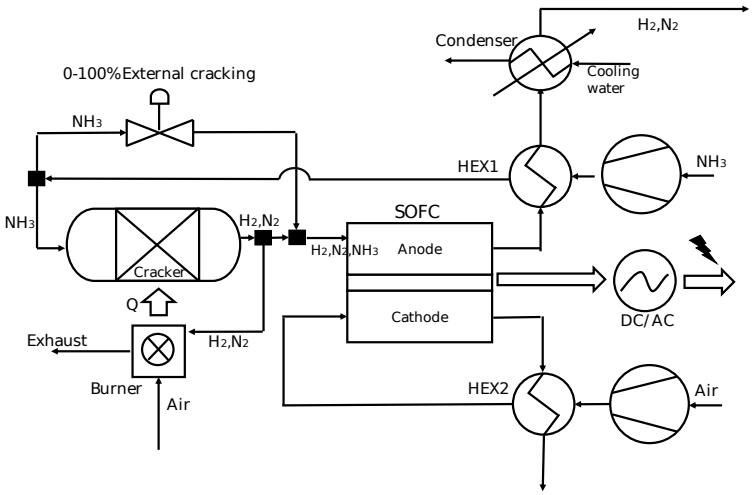

Figure 3.2: Layout of the SOFC system.

3.1.1. Mass balance of the stack

It is assumed that the only reactions taking place in the fuel cell include the hydrogen oxidation reaction (HOR, 3.1) and the ammonia decomposition reaction (ADR, already introduced in chapter 2; equation 2.10):

$$\mathrm{H_2}(g) + \frac{1}{2}\mathrm{O_2}(g) \rightarrow \mathrm{H_2O}(g) \tag{3.1}$$

$$\mathrm{NH_3}(g) \rightarrow 0.5\ \mathrm{N_2}(g) + 1.5\mathrm{H_2}(g) \tag{3.2}$$

Kang et al., [61] propose a useful way to solve the mass balance in the cathode and anode channel. These equations have been adapted to be applicable to be used with ammonia instead of methane. The mass balance of the anode channel consists of inflow, outflow, a term including the hydrogen oxidation and ammonia decomposition in the stack, and an accumulation term approximating $x_i^{\mathrm{cell}} = x_i^{\mathrm{out}}$:

$$\frac{p_{\mathrm{an}} V_{\mathrm{an}}}{\bar{\mathrm{R}} T^{\mathrm{stack}}} \frac{\mathrm{d}x_{\mathrm{i}}^{\mathrm{out}}}{\mathrm{d}t} = \dot{N}_{\mathrm{an}}^{\mathrm{in}} x_i^{\mathrm{in}} - \dot{N}_{\mathrm{an}}^{\mathrm{out}} x_i^{\mathrm{out}} + WL \sum_{j=1}^{2} \nu_{ij} r_j \qquad i \in \{\mathrm{H_2}, \mathrm{NH_3}, \mathrm{N_2}, \mathrm{H_2O}\} \quad j \in \{\mathrm{HOR}, \mathrm{ADR}\} \tag{3.3}$$

where i includes the anode channel components, j fuel cell reactions, $\dot{N}$ is the total molar flow rate, x_i is the mole fraction of component i, W is the cell width, and L is the cell length. ν_{ij} is the stoichiometric coefficient of component i in reaction j, and r_j is the area-specific reaction rate of reaction j. The term left of the dynamic $\frac{\mathrm{d}}{\mathrm{d}t}$ involves the total number of moles in the anode channel. Similarly, for the cathode channel:

$$\frac{p_{\mathrm{ca}} V_{\mathrm{ca}}}{\bar{\mathrm{R}} T^{\mathrm{stack}}} \frac{\mathrm{d}x_{\mathrm{i}}^{\mathrm{out}}}{\mathrm{d}t} = \dot{N}_{\mathrm{ca}}^{\mathrm{in}} x_i^{\mathrm{in}} - \dot{N}_{\mathrm{ca}}^{\mathrm{out}} x_i^{\mathrm{out}} + WL \sum_{j=1}^{2} \nu_{ij} r_j \qquad i \in \{\mathrm{O_2}, \mathrm{N_2}\} \quad j \in \{\mathrm{HOR}, \mathrm{ADR}\} \tag{3.4}$$

The outlet total molar flow rates of the channels are found using:

$$\dot{N}_{\mathrm{an}}^{\mathrm{out}} = \dot{N}_{\mathrm{an}}^{\mathrm{in}} + r_{\mathrm{ADR}} WL, \tag{3.5}$$

$$\dot{N}_{\mathrm{ca}}^{\mathrm{out}} = \dot{N}_{\mathrm{ca}}^{\mathrm{in}} - \frac{r_{\mathrm{HOR}}}{2} WL \tag{3.6}$$

Where the total molar concentration transient in the anode and cathode channel is neglected [62]. The HOR only affects the total molar flow rate change between cathode inlet and outlet due to its stoichiometry. The same is true for the ADR, which only affects the change from inlet to outlet molar flow rate of the anode channel. The area-specific reaction rate of the HOR is linked to the current density:

$$r_{\mathrm{HOR}} = \frac{i}{n_{\mathrm{e}} \mathrm{F}} \tag{3.7}$$

Table 3.1: Stoichiometric coefficient ν for each component in the hydrogen oxidation reaction (3.1) and the ammonia decomposition reaction (3.2).

	ν_{HOR}	ν_{ADR}
H_2	-1	1.5
NH_3	0	-1
N_2	0	0.5
H_2O	1	0
O_2	$-\frac{1}{2}$	0

100% conversion of the ammonia is assumed, as several authors support this. For instance, Kalinci and Dincer claims, "After checking the literature and results, one can write that considering a full conversion of NH_3 is conceptually reasonable enough from the viewpoint of the model accuracy" [59]. Kishimoto et al. showed that all ammonia decomposes in the anode channel at 700°C with a numeric model [66]. Experiments from Ma et al. indicate that ammonia decomposition is not the rate-determining reaction [77], simplifying the ADR reaction rate. It simply includes the total ammonia inflow to the anode, divided by the cell area.

$$r_{\text{ADR}} = \frac{\dot{N}_{\text{an}}^{\text{in}} x_{\text{NH}_3}^{\text{in}}}{WL} \tag{3.8}$$

3.1.2. Energy balance of the stack and temperature control

Equation 3.9 gives the energy balance of a single SOFC. The heat capacity of the gas is neglected: only the solid part of the cell determines the rate of energy accumulation [61, 119]. Contrary to more detailed models [119], the stack is modelled so that there is only one temperature layer: the electrodes, electrolyte, interconnect and gas channels. Equation 3.9 does not include any radiative, convective or conductive terms (in contrast to in [14]): they are equal to 0 due to the absence of a cell's temperature difference ΔT between different layers. Stack cell's temperature s along the flow direction or along the width or the height of the channel are neglected. This is considered to be valid because a number of modelling studies [14, 21, 100, 119] report ≤ 20 K total temperature difference between different layers. Only the interconnect temperature layer in [14] is (up to) another 20 K apart from the other layers. The dynamic term on the left implies that the outlet temperature represents the cell temperature as a whole as in a stirred tank reactor. This results in an error in dynamic behaviour, but the term diminishes once the system reaches steady-state.

$$\begin{aligned} m_{\text{solid}} c_{p,\text{solid}} \frac{\mathrm{d}T^{\text{out}}}{\mathrm{d}t} = \sum_{i=1}^{4} (\dot{N}_i^{\text{in}} h_i^{0,\text{in}} - \dot{N}_i^{\text{out}} h_i^{0,\text{out}})_{\text{an}} + \sum_{i=1}^{2} (\dot{N}_i^{\text{in}} h_i^{0,\text{in}} - \dot{N}_i^{\text{out}} h_i^{0,\text{out}})_{\text{ca}} - i V_{\text{cell}} WL - \dot{Q}_{\text{loss}} \\ i \in \{H_2, NH_3, N_2, H_2O\} \text{ (anode)} \\ i \in \{O_2, N_2\} \quad \text{(cathode)} \end{aligned} \tag{3.9}$$

$h^{0,\text{in}}$ and $h^{0,\text{out}}$ are functions of T^{in} and T^{out}, respectively. They are approximated using polynomials from NIST [4] (appendix A.2). $\dot{Q}_{\text{loss}}$ is estimated by computing the sensible heat gain by the anode and cathode gas and assuming that 5% is lost to the environment. The heat capacity of the solid is the sum of the heat capacities of the PEN (positive-electrolyte-negative) structure and the interconnect:

$$m_{\text{solid}} c_{\text{p,solid}} = \rho_{\text{PEN}} \cdot c_{\text{p,PEN}} \cdot (\tau_{\text{an}} + \tau_{\text{ca}} + \tau_{\text{el}}) + \rho_{\text{I}} \cdot c_{p,\text{I}} \cdot (\tau_{\text{I}} + \tau_{\text{I}} + \tau_{\text{I}}). \tag{3.10}$$

An excessive temperature gradient between the inlet and outlet of the SOFC stack is prevented using a temperature controller (figure 3.3). The PID controller monitors the output temperature setpoint and changes the output of the controller, the air excess λ_{air}, until the process value of the outlet temperature matches the setpoint. The air excess is not allowed to drop below 2 in the model. The desired stack temperature T_{stack} and $\Delta T = T_{\text{gas}}^{\text{out}} - T_{\text{gas}}^{\text{in}}$ are input to the model. 100 K temperature difference between the stack inlet and outlet (ΔT) is maintained. The outlet temperature setpoint is $T_{\text{stack}} + \frac{\Delta T}{2}$ and the inlet temperature is fixed at $T_{\text{stack}} - \frac{\Delta T}{2}$. The following equation governs the molar flow rate of air flowing into the cathode channel:

$$\dot{N}_{\text{ca}}^{\text{in}} = \frac{i \cdot W \cdot L \cdot \lambda_{\text{air}}}{4\text{F} \cdot x_{\text{O}_2}^{\text{in}}} \tag{3.11}$$

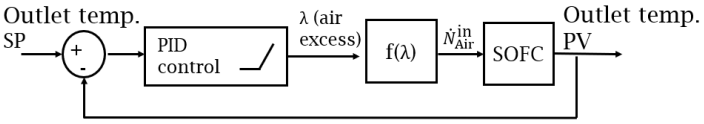

Figure 3.3: Temperature controller structure.

3.1.3. Electrochemistry

In the electrochemical model it is assumed that no direct oxidation of ammonia takes place. The partial pressures of reactants and products, which are used in the following equations, are approximated using:

$$p_i = \frac{p_i^{\text{in}} + p_i^{\text{out}}}{2} \qquad i \in \{H_2, O_2, H_2O\} \tag{3.12}$$

p_i^{out} follows from the mass balance. p_i^{in} is determined by assuming all ammonia entering the SOFC is instantaneously decomposed directly after the fuel cell inlet. In practice, this would not be possible, but it prevents the average partial pressure of hydrogen in the stack (equation 3.12) from being highly underestimated. The electrochemical performance is evaluated at an averaged stack temperature T_{stack} defined as:

$$T^{\text{stack}} = \frac{T^{\text{in}} + T^{\text{out}}}{2} \tag{3.13}$$

Equation 3.13 suggests a linear temperature profile, which is unlikely to be the case, but expected to be a better approximation of 3.13 than taking either T^{out} or T^{in} as representative for T^{stack}. The no-loss voltage of the fuel cell is given by the Nernst equation:

$$E = -\frac{\Delta g^0}{n_e \text{F}} + \frac{\bar{\text{R}} T}{2\text{F}} \ln\left(\frac{\frac{p_{H_2}}{p^0} \cdot \left(\frac{p_{O_2}}{p^0}\right)^{\frac{1}{2}}}{\frac{p_{H_2O}}{p^0}} \right) \tag{3.14}$$

Δg^0 is the change of the Gibbs free energy from the reactants to the product of the hydrogen oxidation:

$$\Delta g^0 = g^0_{H_2O} - g^0_{H_2} - \frac{1}{2} g^0_{O_2} \tag{3.15}$$

Where the Gibbs free energy of the reactants and products is calculated using the standard enthalpy h_0 and standard entropy s_0, which are both approximated using polynomials from NIST [4] (appendix A.2).

$$g_i^0 = h_i^0 - T \cdot s_i^0 \qquad i \in \{H_2, O_2, H_2O\} \tag{3.16}$$

The theoretical output voltage is corrected by activation, concentration and ohmic losses according to equation 2.7. The activation losses, ΔV_{act} are modelled using a form of the Butler-Volmer equation [14, 31], as explained in section 2.1.3.

$$\Delta V_{\text{act}} = \frac{2\bar{\text{R}} T^{\text{stack}}}{n_e \text{F}} \sinh^{-1}\left(\frac{i}{2 i_{0,\text{cathode}}}\right) + \frac{2\bar{\text{R}} T^{\text{stack}}}{n_e \text{F}} \sinh^{-1}\left(\frac{i}{2 i_{0,\text{anode}}}\right) \tag{3.17}$$

Where the exchange current densities i_0 [14] are determined using:

$$i_{0,\text{electrode}} = \frac{\bar{\text{R}} T^{\text{stack}}}{n_e \text{F}} k_{\text{electrode}} \cdot \exp\left(-\frac{E_{\text{electrode}}}{\bar{\text{R}} T^{\text{stack}}}\right) \qquad \text{electrode} \in \{\text{anode}, \text{cathode}\} \tag{3.18}$$

$k_{\text{electrode}}$ and $E_{\text{electrode}}$ are the pre-exponential factor and the activation energy of the exchange current density, respectively [14]. Concentration losses result from the local depletion of reactants and are expressed as:

$$\Delta V_{\text{con}} = \frac{\bar{\text{R}} T^{\text{stack}}}{2\text{F}} \ln\left(\frac{p_{H_2O,\text{TPB}} \cdot p_{H_2}}{p_{H_2O} \cdot p_{H_2,\text{TPB}}}\right) + \frac{\bar{\text{R}} T^{\text{stack}}}{4\text{F}} \ln\left(\frac{p_{O_2}}{p_{O_2,\text{TPB}}}\right) \tag{3.19}$$

Where the partial pressures at the TPB [14, 31] are calculated with:

$$p_{\mathrm{H_2,TPB}} = p_{\mathrm{H_2}} - \frac{\bar{\mathrm{R}} T^{\mathrm{stack}} \tau_{an}}{2\mathrm{F} D_{\mathrm{eff,an}}} i \tag{3.20}$$

$$p_{\mathrm{H_2O,TPB}} = p_{\mathrm{H_2O}} - \frac{\bar{\mathrm{R}} T^{\mathrm{stack}} \tau_{\mathrm{an}}}{2\mathrm{F} D_{\mathrm{eff,an}}} i \tag{3.21}$$

$$p_{\mathrm{O_2,TPB}} = p_{\mathrm{ca}} - (p_{\mathrm{ca}} - p_{\mathrm{O_2}}) \exp\left(\frac{\bar{\mathrm{R}} T \tau_{\mathrm{ca}}}{4\mathrm{F} D_{\mathrm{eff,ca}} p_{\mathrm{ca}}} i\right) \tag{3.22}$$

And $D_{\mathrm{eff,an}}$, τ_{an}, $D_{\mathrm{eff,ca}}$ and τ_{ca} are the effective diffusion coefficients and thicknesses of the electrodes. Finally, the ohmic losses [14] depend on the electric conductivity (σ_{an} and σ_{an}) of the electrodes and the ionic conductivity (σ_{el}) of the electrolyte:

$$\Delta V_{\mathrm{ohm}} = i\left(\frac{\tau_{\mathrm{an}}}{\sigma_{\mathrm{an}}} + \frac{\tau_{\mathrm{el}}}{\sigma_{\mathrm{el}}} + \frac{\tau_{\mathrm{ca}}}{\sigma_{\mathrm{ca}}}\right) \tag{3.23}$$

The cell voltage is obtained by subtracting ohmic, activation and concentration losses from the no-loss voltage.

$$V_{\mathrm{cell}} = E - \Delta V_{\mathrm{ohm}} - \Delta V_{\mathrm{con}} - \Delta V_{\mathrm{act}} \tag{3.24}$$

The cell power is the current density multiplied by the cell voltage and area.

$$P_{\mathrm{cell}} = i \cdot V_{\mathrm{cell}} \cdot W \cdot L \tag{3.25}$$

Input parameters of the fuel cell

The SOFC model requires several cell parameters. In the ideal case, a relevant experimental study with ammonia specifies all parameters listed in table 3.2: Not all materials used in conventional SOFCs are as likely to facilitate ammonia decomposition, or withstand material degradation in an environment with ammonia. Of the most useful papers found ([33, 35, 39, 64, 77, 92]), none provide an experimental analysis from an ammonia-fuelled SOFC together with a thorough evaluation of the properties of the materials used. The current subsection attempts to provide a brief justification for the choices made.

The thickness and conductivity of the cell layers are important in estimating the ohmic losses. Two options are considered to determine τ and σ:

- Obtain data for layer thickness and conductivity from a modelling study using an anode-supported cell such as [14] or [61]. This is the easiest option but does not necessarily apply to ammonia SOFCs, not least because it is not stated clearly what kind of materials the input properties rely on.
- The most relevant experimental studies describe the material type and the thickness of the cell layers. The properties of the material can be searched for in literature. This could be more realistic than the first option but is an oversimplification as well, due to the effect of, for example, micro-structure on the cell resistance [50]. It was found that it is difficult to find exactly the same materials in literature.

Electrolyte resistance appears to dominate the ohmic cell resistance, which follows from inserting the input data from Aguiar et al. [14] in equation 3.23. The options listed above are, therefore, briefly compared for the electrolyte only. Using cell data from Kishimoto et al. [64] is tempting, as it is the only kW-scale SOFC system study using ammonia. They describe the electrolyte as "ZrO_2-based material" what is likely to be yttria-stabalized zirconia (ZrO_2). Measurements on YSZ electrolyte for SOFCs have been performed by Han et al.. They provide material conductivity for a range of temperatures and different fabrication methods [50]. Figure 3.4 provides a comparison with the electrolyte conductivity equation provided by Aguiar et al. [14]. The trend is similar, but the conductivity found in [50] is still significantly higher. The overall resistance as in equation 3.23 would be 3 times as low using the Han et al. [50] conductivity for the cell data from [64], compared to the model used in Aguiar et al. A more conservative estimation is preferred, so τ and σ are adopted from [14] [14].

[14] is considered to be the source of choice for the effective diffusion coefficients $D_{\mathrm{eff,electrode}}$ too, in the absence of ammonia SOFC data in that context.

$c_{p\mathrm{solid}}$ and ρ_{solid} determine the heat capacity of the stack and are of importance when the transient characteristics of the stack are analysed. However, dynamic operation is not a focus point of this study. The used values originate from [14] as well, the sake of simplicity.

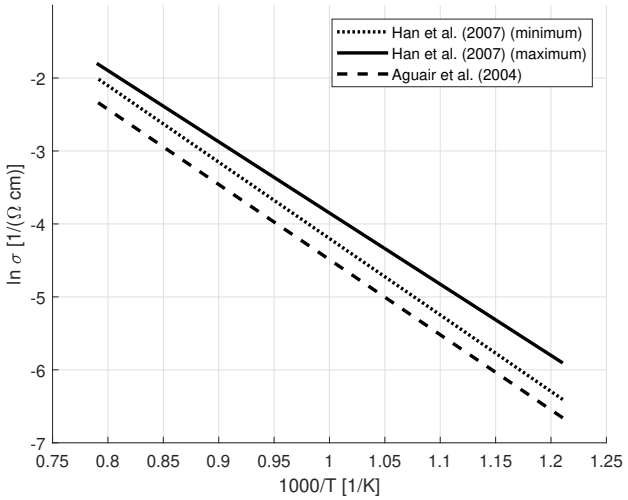

Figure 3.4: Comparison between the electrolyte conductivity found in the experimental study from Han et al. [50] and the electrolyte conductivity found in the modelling study from Aguiar et al. [14].

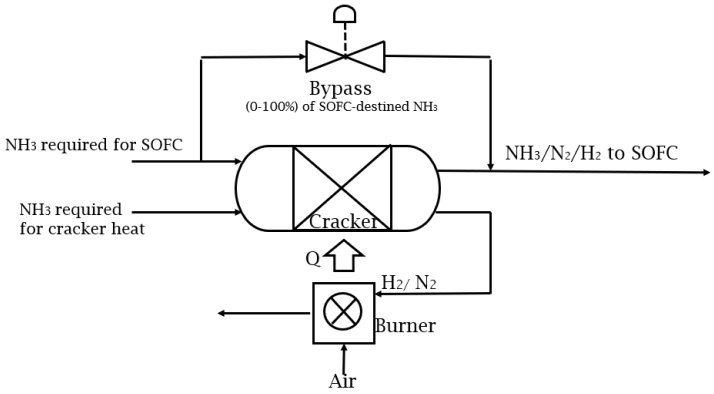

Figure 3.5: Schematic representation of the external cracker sub-model as a part of the hybrid system.

The activation overpotential input parameters $k_{\text{electrode}}$ and $E_{\text{electrode}}$ are described in [14] in at least some extent, in contrary to other papers found. Using them is considered appropriate as well. The authors claim that k_{ca} and E_{ca} are applicable to "YSZ-based materials".

All parameters (table 3.2) relevant for the electrochemical model are adopted from the direct internal reforming methane SOFC model of the frequently cited study from Aguiar et al. [14], which is appropriate because:

- Experimental or numerical studies with ammonia SOFCs provide insufficient information for an adequate electrochemical model.
- Equivalent to this study, Aguiar et al. assume only hydrogen is electrochemically oxidised.
- Aguiar et al. model an anode-supported cell, which is the type used most frequently in ammonia SOFC experiments [33, 35, 39, 64, 77, 92].

An improved evaluation of the parameters of an ammonia-ready fuel cell is left for further research.

3.1.4. External cracker

As described in subsection 2.2.2, an external cracker can be used to decompose ammonia into hydrogen and nitrogen before the SOFC stack. The amount of fuel required in the SOFC depends on the operating current, the total amount of H_2 molecules that can be extracted from the incoming flow and the utilisation of fuel in the SOFC. The model is suitable for hydrogen supply as well, apart from ammonia. The fuel utilisation of the

Table 3.2: Properties of the cell in the SOFC model.

Parameter	Value	Unit	Description
W	0.1	m	Cell width
L	0.1	m	Cell length
h	$1 \cdot 10^{-3}$	m	Channel height
τ_{an}	$500 \cdot 10^{-6}$	m	Thickness of anode
τ_{ca}	$50 \cdot 10^{-6}$	m	Thickness of cathode
τ_{el}	$20 \cdot 10^{-6}$	m	Thickness of electrolyte
τ_{I}	$500 \cdot 10^{-6}$	m	Thickness of interconnect
σ_{an}	$80 \cdot 10^{3}$	$\Omega^{-1}\text{m}^{-1}$	Electric conductivity of anode
σ_{ca}	$8.4 \cdot 10^{3}$	$\Omega^{-1}\text{m}^{-1}$	Electric conductivity of cathode
σ_{el}	$33.4 \cdot 10^{3} \cdot \exp\left(-\frac{10300}{T}\right)$	$\Omega^{-1}\text{m}^{-1}$	Ionic conductivity of electrolyte
$D_{\text{eff,an}}$	$3.66 \cdot 10^{-5}$	$\text{m}^2 \cdot \text{s}^{-1}$	Effective diffusion coefficient of anode
$D_{\text{eff,ca}}$	$1.37 \cdot 10^{-5}$	$\text{m}^2 \cdot \text{s}^{-1}$	Effective diffusion coefficient of cathode
$c_{p,\text{PEN}}$	500	$\text{J} \cdot \text{kg}^{-1} \cdot \text{K}^{-1}$	Specific heat capacity of PEN structure
$c_{p,\text{I}}$	500	$\text{J} \cdot \text{kg}^{-1} \cdot \text{K}^{-1}$	Specific heat capacity of interconnect
ρ_{PEN}	5000	$\text{kg} \cdot \text{m}^{-3}$	Mass density of PEN structure
ρ_{I}	8900	$\text{kg} \cdot \text{m}^{-3}$	Mass density heat capacity of interconnect
k_{an}	$2.35 \cdot 10^{3}$	$\text{A} \cdot \text{m}^{-2}$	Pre-exponential factor of i_0 at anode
k_{ca}	$6.54 \cdot 10^{3}$	$\text{A} \cdot \text{m}^{-2}$	Pre-exponential factor of i_0 at cathode
E_{an}	$140 \cdot 10^{3}$	$\text{J} \cdot \text{mol}^{-1}$	Activation energy of i_0 at anode
E_{ca}	$137 \cdot 10^{3}$	$\text{J} \cdot \text{mol}^{-1}$	Activation energy of i_0 at cathode

stack is defined as:

$$UF = \frac{iWL}{2\text{F}(1.5x^{\text{in}}_{\text{NH}_3} + x^{\text{in}}_{\text{H}_2})\dot{N}^{\text{in}}_{\text{tot}}} \tag{3.26}$$

Rewriting provides the total molar flow rate of fuel required for the SOFC power production. Note that this does **not** include the fuel potentially required to heat the cracker. Those streams are distinguished.

$$\dot{N}^{\text{in}}_{\text{tot}} = \frac{iWL}{2\text{F}(1.5x^{\text{in}}_{\text{NH}_3} + x^{\text{in}}_{\text{H}_2})UF} \tag{3.27}$$

The molar flow rate per component of the stream going to the SOFC is calculated using the input composition and the total molar flow rate. H_2O is also included, as this is produced further downstream.

$$\begin{aligned} \dot{N}_i &= x_i \dot{N}_{\text{tot}} \\ i &\in \{\text{H}_2, \text{NH}_3, \text{N}_2, \text{H}_2\text{O}\} \end{aligned} \tag{3.28}$$

The external cracking ratio (ecr) is an essential parameter in the model. It governs the amount of the SOFC-destined ammonia cracked externally (i.e. before entering the stack) in a reactor. It is the ratio of the converted NH_3 and the NH_3 to supply the necessary hydrogen for the electrochemical reaction in the SOFC. Again, this does not include the ammonia cracked to heat the cracker itself.

$$ecr = \frac{\dot{N}^{\text{cracked}}_{\text{NH}_3}}{\dot{N}^{\text{in}}_{\text{NH}_3}} = 1 - \frac{\dot{N}^{\text{out}}_{\text{NH}_3}}{\dot{N}^{\text{SOFC,in}}_{\text{NH}_3}} \tag{3.29}$$

Decomposing NH_3 is an equilibrium reaction. Nevertheless, it is assumed that all ammonia entering the cracker is converted, as equilibrium conversion is above 99.5% at a temperature higher than 800 K [17]: The fuel is pre-heated before the cracker. Still, ecr can be manually adjusted in the model (see figure 3.5). In practice, this means that 100% conversion is obtained in the external cracker, but that part of the incoming flow to the cracker is bypassed for $ecr < 1$ (see figure 3.5). The input composition of fuel: $x^{\text{in}}_{\text{H}_2}$, $x^{\text{in}}_{\text{NH}_3}$, $x^{\text{in}}_{\text{N}_2}$ and $x^{\text{in}}_{\text{H}_2\text{O}}$ can be freely chosen on the condition than $\sum x_i = 1$. $x^{\text{in}}_{\text{NH}_3}$ will normally be used in line with the goals of this research. Neglecting the accumulation of components in the external cracker yields expressions that calculate the outflow per component of the stream going to the SOFC stack:

$$\begin{aligned} \dot{N}^{\text{out}}_i = \dot{N}^{\text{out}}_{\text{an}} &= \dot{N}^{\text{in}}_i + ecr \cdot \nu_{i,\text{ADR}} \cdot \dot{N}^{\text{in}}_{\text{NH}_3} \\ i &\in \{\text{H}_2, \text{NH}_3, \text{N}_2, \text{H}_2\text{O}\} \end{aligned} \tag{3.30}$$

In which $\nu_{i,\mathrm{ADR}}$ is the stoichiometric coefficient of component i in the ammonia decomposition reaction (ADR, 3.2), listed in table 3.1. After this, the composition of the flow going to the SOFC anode can be calculated using:

$$x_i = \frac{\dot{N}_i}{\sum_{i=1}^{4} \dot{N}_i} \qquad i \in \{H_2, NH_3, N_2, H_2O\} \tag{3.31}$$

It is assumed that there is no heat loss from the cracker and the transient term of the energy balance is neglected, which reduces the energy balance to:

$$0 = \sum_{i=1}^{4} (\dot{N}_i^{0,\mathrm{in}} h_i^{0,\mathrm{in}} - \dot{N}_i^{0,\mathrm{out}} h_i^{0,\mathrm{out}}) + \dot{Q} \qquad i \in \{H_2, NH_3, N_2, H_2O\} \tag{3.32}$$

Where $h_i^{0,\mathrm{in}}$ and $h_i^{0,\mathrm{out}}$ are functions of T^{in} and T^{out} (appendix A.2), respectively. $\dot{Q}$, the heat supplied to the cracker, will be significant due to the highly endothermic nature of the ADR. The external cracker model is shown schematically in figure 3.5. The right amount of heat is supplied, so $T^{\mathrm{in}}_{\mathrm{cracker}}$=$T^{\mathrm{out}}_{\mathrm{cracker}}$.

All equations above are **only** for the fuel streams required for the SOFC. However, a substantial amount of heat has to be supplied if the cracker is used, which is achieved by burning hydrogen obtained by cracking an additional amount of ammonia. Equation 3.32 is solved for $\dot{Q}$. Then, the heat required to crack one mole of ammonia is determined:

$$q_{\mathrm{reaction}} = \frac{\dot{Q}}{\dot{N}_{\mathrm{cracked}}} \tag{3.33}$$

One mole of ammonia is cracked to 1.5 moles of hydrogen. This hydrogen is burned to heat the cracker, but obtaining it requires heat as well. The net heat from one mole of additional ammonia is approximated:

$$q_{\mathrm{net,NH3}} = 1.5 \cdot LHV_{H_2} - q_{\mathrm{reaction}} \tag{3.34}$$

So to estimate the amount of additional ammonia, one divides the heat required to maintain the SOFC-destined ammonia cracking reaction by the result of the equation above, which is corrected by $\eta_{\mathrm{heat}} = 0.9$ to account for heat losses in the reactor heating system.

$$\dot{N}_{\mathrm{NH3,heat}} = \frac{\dot{Q}}{q_{\mathrm{net,NH3}} \cdot \eta_{\mathrm{heat}}} \tag{3.35}$$

3.1.5. Heat integration

Incoming cold air and fuel and the endothermic ammonia decomposition reaction in the external cracker need substantial heat. Anode and cathode off-gas are often mixed and burned to provide a high-temperature heat source used in the heat sinks simultaneously, in more traditional standalone SOFC systems. In this study, however, anode off-gas will be used in the ICE downstream. Therefore, a configuration (see figure 3.2) has been chosen where cathode off-gas pre-heats the cathode intake air. The anode off-gas pre-heats the fuel going to the anode, and the fuel required for the burner hydrogen. Further research could optimise heat integration. Besides this, the simplicity of the proposed heat integration layout contributes to meeting marine power plant demands related to power density, load transients, system start-up and reliability (section 2.3.6).

The heat integration sub-model (appendix A.1) solves the heat balance of the two heat exchangers and computes the outlet temperature of the hot flows providing the heat. Heat loss is to the environment is neglected, the energy balance uses NIST [4] thermodynamic properties (appendix A.2). In the "normal" case, the hot streams heat the cold streams while maintaining at least a 20 K approach temperature in the heat exchanger. The anode exit stream contains more mass than the anode inlet stream, so normally enough heat is available to heat the fuel. The opposite is true in the cathode channel, where oxide ions diffuse to the anode channel. If there is not enough heat in the cathode outlet channel, the outlet stream may approach the inlet stream too closely. Therefore, the model puts out a warning if a non-physical outlet temperature occurs.

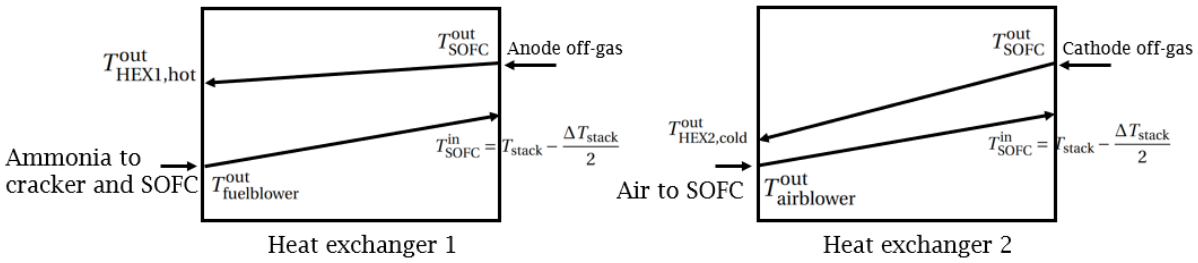

Figure 3.6: Visualisation of the temperature profile in the heat exchangers. The heat capacity of off-gas is higher than the fuel stream in heat exchanger 1. In heat exchanger 2, the incoming air has a higher heat capacity.

A simple model of a condenser is made, which calculates the cold utility required to remove the water from the anode off-gas stream. It first cools down the stream to 100°C and calculates the required duty equivalent to equation A.13. Then, it calculates the condensing duty by multiplying the enthalpy of vaporisation with the flow rate of water.

$$\dot{Q} = \Delta h^{vap} \cdot \dot{N}_{H_2O} \tag{3.36}$$

The required cooling water (CW) flow is estimated by assuming a 10 K temperature rise of the cooling water.

$$\dot{V} = -\frac{\dot{Q}}{\rho_{water} \cdot c_{p,water} \cdot \Delta T_{CW}} \tag{3.37}$$

The power of the water pump can be calculated by multiplying the volume flow with the expected pressure drop, but it has been neglected throughout this research due to its limited impact on the overall efficiency.

3.1.6. Fuel and air blowers

Blowers make sure that fuel and air is circulated through the SOFC system. The temperature rise is estimated by equation 3.38, assuming non-isentropic compression.

$$\Delta T_{blower} = \frac{T_{amb} \cdot \left(\left(\frac{p_{out}}{p_{amb}} \right)^{\frac{\kappa_{amb}-1}{k_{amb}}} - 1 \right)}{\eta_{is}} \tag{3.38}$$

ΔT_{blower} is used in equation 3.39 that calculates the electrical power to drive the blowers.

$$P_{blower} = \frac{N_{cells} \cdot \Delta T_{blower} \cdot \sum \dot{N}_i \cdot c_{p,i}}{\eta_{mech}} \tag{3.39}$$

The number of cells, N_{cells} is included, as the molar flow rate is calculated on a per-cell basis while the system blower power is required.

Literature reports a wide variety of SOFC pressure drops, and many of them only include the stack pressure loss. Analogues to Cinti et al. [35] a 100 millibar cathode and anode (which was not specified in [35]) system pressure drop is assumed. The pressure drop is specified at $ecr = 1$, $UF = 0.7$ and $T_{stack} = 1073$ K, after which the incoming volume flow is determined. Linear extrapolation is based on the volume flow is used to estimate the pressure drop at off-design operating points. This approach has been adopted from Peters et al., except for the fact that they include a 20% quadratic relation in the cathode side pressure drop. Table 3.3 lists the data used in the blower models.

The gas composition before the SOFC stack is used in equation 3.39, but for ammonia, the composition before the cracker instead of the stack should have been used. Next to this, the ratio of specific heats for air is also applied for the anode side but should have been 1.3 for ammonia. Despite those errors, the subsequent overestimation in fuel blower power is expected to have a limited impact on the overall system, as the airflow is considerably higher than the fuel flow.

3.1.7. Power output and efficiency

The power output of the stack scales with the number of cells.

$$P_{stack} = N_{cells} \cdot P_{cell} \tag{3.40}$$

	Value	Unit
c_{p,O_2}	29.4	$J \cdot kg^{-1} \cdot mol^{-1}$
c_{p,N_2}	29.1	$J \cdot kg^{-1} \cdot mol^{-1}$
c_{p,NH_3} (gas)	36.6	$J \cdot kg^{-1} \cdot mol^{-1}$
c_{p,H_2}	28.8	$J \cdot kg^{-1} \cdot mol^{-1}$
η_{is}	0.6	–
η_{mech}	0.9	–
p_{amb}	1.015	bar
k_{amb}	1.4	–

Table 3.3: Specific heat capacity, isentropic efficiency, mechanical efficiency, ambient pressure and ambient ratio of specific heats used in the fuel and air blower models.

The electrical efficiency of the stack is defined with the LHV of the exact composition of the stream entering the stack containing hydrogen or ammonia fuel, or both:

$$\eta_{cell} = \frac{P_{cell}}{LHV_{NH_3} \cdot \dot{N}^{in}_{NH_3} + LHV_{H_2} \cdot \dot{N}^{in}_{H_2}} \tag{3.41}$$

The electrical efficiency of the stack is greatly affected by the fuel utilisation, as the fuel leaving the stack unused is also incorporated in the denominator stack efficiency. Therefore, a corrected stack efficiency ($\eta_{cell,corrected}$) is proposed, as well. Due to the assumption that all ammonia is decomposed in the stack, the anode off-gas only contains hydrogen, so equation 3.42 is only corrected for hydrogen in the off-gas.

$$\eta_{cell,corrected} = \frac{P_{cell}}{LHV_{NH_3} \cdot \dot{N}^{in}_{NH_3} + LHV_{H_2} \cdot (\dot{N}^{in}_{H_2} - \dot{N}^{out}_{H_2})} \tag{3.42}$$

The DC cell power is converted to AC power via a 95% efficient inverter ($\eta_{DC/AC} = 0.95$). Three different SOFC system efficiencies are defined. η_{SOFC} (eq. 3.43) is most important. It is the electrical efficiency of the SOFC system in the configuration (figure 3.2) that can be combined with the ICE. The LHV of the ammonia entering the SOFC system includes the ammonia required for the electrochemical oxidation of hydrogen in the SOFC, as well as the ammonia cracked and burned to supply the heat of the reaction in the cracker ($\dot{N}_{NH_3,total} = \dot{N}_{NH_3,SOFC} + \dot{N}_{NH_3,crackerheat}$)..

$$\eta_{SOFC} = \frac{\eta_{DC/AC} \cdot P_{stack} - P_{fuelblower} - P_{airblower}}{LHV_{NH_3} \cdot \dot{N}_{NH_3,total}} \tag{3.43}$$

The gross SOFC system efficiency $\eta_{SOFC,gross}$ excludes the ammonia cracked and burned to supply the heat of the reaction in the cracker.

$$\eta_{SOFC,gross} = \frac{\eta_{DC/AC} \cdot P_{stack} - P_{fuelblower} - P_{airblower}}{LHV_{NH_3} \cdot \dot{N}_{NH_3,SOFC}} \tag{3.44}$$

Off-gas is used in the downstream engine in the hybrid configuration. However, hydrogen off-gas can be combusted and used to heat the external cracker, in a hypothetical standalone (SA) configuration. 90% of total the hydrogen off-gas lower heating value is subtracted from the required heat in the external cracker to yield a standalone efficiency.

$$\eta_{SOFC,SA} = \frac{\eta_{DC/AC} \cdot P_{stack} - P_{fuelblower} - P_{airblower}}{LHV_{NH_3} (\dot{N}_{NH_3,SOFC} + \dot{N}_{NH_3,crackerheat,SA})} \tag{3.45}$$

The standalone system efficiency is often equal to the gross SOFC efficiency due to the abundant presence of hydrogen in the off-gas; $\dot{N}_{NH_3,crackerheat,SA} = 0$ in that case.

3.2. Internal combustion engine sub-model

The internal combustion engine sub-model has been built in MATLAB & Simulink and is based on a five-point dual (Seiliger) cycle. The model is an adaption of a Diesel engine model received from Peter de Vos, head of the MSc programme Maritime Technology at TU Delft. As data of large-scale ammonia-hydrogen

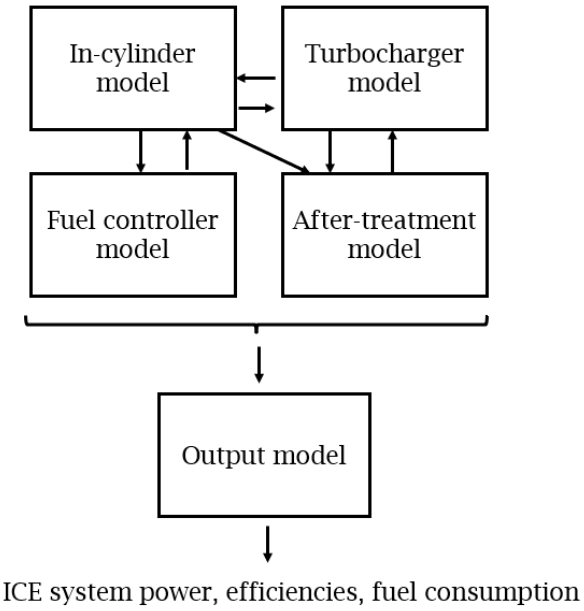

Figure 3.7: Structure of the ICE system model developed in MATLAB & Simulink.

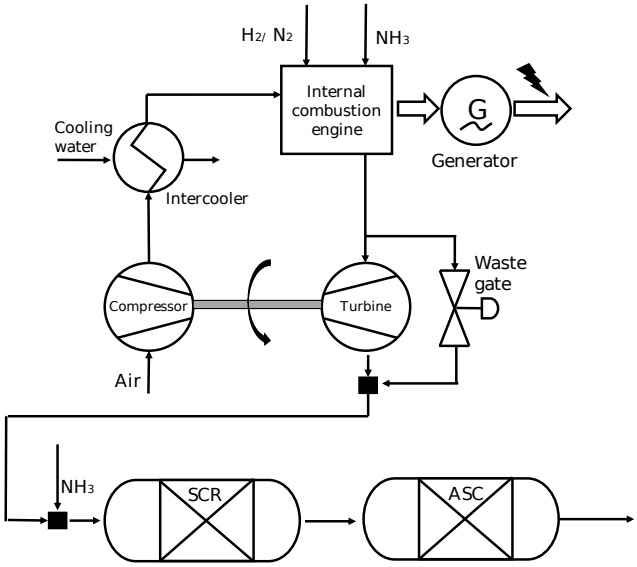

Figure 3.8: Layout of the ICE system.

Table 3.4: Wärtsilä 12V31DF main engine properties.

Variable	Value	Unit	Description
P_{nom}	7200	[kW]	Nominal power output
N	750	[min^{-1}]	Engine speed
ϵ	14.0	[-]	Geometric compression ratio
D	310	[mm]	Bore
S	430	[mm]	Stroke
i	12	[-]	Number of cylinders
k	2	[-]	Revolutions per cycle

engines is not available, the geometry and nominal power output are based on a Wärtsilä 12V31DF, which can operate with LNG using a pilot fuel or HFO. The Wärtsilä 12V31DF is a highly efficient four-stroke engine and is designed to drive a generator to act as an auxiliary engine or as the main engine in a Diesel-electric configuration. The model consists of a number of sub-models.

- The in-cylinder model is a dual cycle and comprises four sub-models describing compression, isochoric combustion, isobaric combustion and expansion. A heat release model calculates the heat release from the fuel.
- The non-isentropic turbocharger model estimates the work extracted from the exhaust flow using a turbine and calculates the pressure and temperature of the air coming out of the compressor. A wastegate controller lets a fraction of the exhaust gas bypass the turbine, possibly preventing too high air excess ratios. The compressed air is cooled in an intercooler before the intake.
- A fuel controller makes sure that the desired power output is obtained. It handles either natural gas or ammonia and is capable of dealing with hydrogen entering from the SOFC.
- The after-treatment sub-model includes mass- and energy balances of a selective catalytic reduction reactor and an ammonia slip catalyst.
- The output model calculates the power output, efficiency and fuel consumption.

3.2.1. In-cylinder model

An air-standard [84] analysis is conducted, which means a fixed amount of air is assumed to act as working fluid and the air exchange process occurring in reality is neglected. No combustion modelling is performed, but the heat from the fuel is assumed to come from an external source. The air-standard is different from the cold air-standard analysis, as $\kappa = \frac{c_p}{c_p}$ is not considered constant throughout the air-standard process. The effective compression ratio [109] is calculated using:

$$r_c = x \cdot (\epsilon - 1) + 1 \tag{3.46}$$

x is approximated with 1, as four-stroke engine inlets close near BDC [109]. The stroke volume V_s is used to calculate the trapped volume V_1 [109]. Rewriting the definition of the effective compression ratio [109] provides the volume after compression V_2.

$$V_s = \frac{\pi}{4} \cdot D^2 \cdot S \tag{3.47}$$

$$V_1 = V_s \cdot \left(\frac{r_c}{\epsilon - 1}\right) \tag{3.48}$$

$$V_2 = V_1 \cdot r_c \tag{3.49}$$

Heat release

The mass of air trapped in the cylinder per cycle is estimated using the ideal gas law:

$$m_{\text{air,cycle}} = \frac{p_1 V_1}{R_{\text{air}} T_1} \tag{3.50}$$

Table 3.5: Lower heating value, stoichiometric air-to-fuel ratio and combustion efficiency of the fuels used.

	H_2	NH_3	CH_4
LHV [MJ · kg^{-1}]	120.0	18.6	49.7
σ [-]	34.5	6.1	17.2
η_c (assumption) [-]	1.00	0.95	1.00

The effective specific heat input per cycle is approximated by equation 3.51. K, the number of fuels, is 1 for single fuel and 2 dual-fuel operation.

$$q_{\text{cycle,in}} = \frac{\eta_q \cdot \sum_{i=1}^{K} m_{\text{fuel,i,cycle}} \cdot \eta_{c,i} \cdot \text{LHV}_{\text{fuel,i}}}{m_{\text{air,cycle}}} \tag{3.51}$$

η_q is the heat input efficiency and is assumed to be 0.9, regardless of the fuel used. η_c is the combustion efficiency and is assumed to be 1 for hydrogen or conventional fuels. $\eta_c = 0.95$ is assumed for ammonia because a minimum 5% [97] unburned ammonia fraction (defined as $\frac{\dot{N}_{NH_3,\text{intake}}}{\dot{N}_{NH_3,\text{intake}}}$ [97]) was demonstrated by Pochet et al. in ammonia-hydrogen ICE experiments.

$q_{\text{cycle,in}}$ is the total heat input per cycle and is split in two parts. One fraction is released during isochoric combustion, and the other part during isobaric combustion. $q_{2\to3}$, seen in equations 3.61 and 3.62, is calculated using the factor X_A: The fraction of the total heat input released during isochoric combustion.

$$q_{2\to3} = X_A \cdot q_{\text{cycle,in}} \tag{3.52}$$

The heat release during isobaric combustion is written as:

$$q_{3\to4} = (1 - X_A) \cdot q_{\text{cycle,in}} \tag{3.53}$$

The parameter X_A is extremely important for the characteristics of the thermodynamic cycle and the performance of the engine. The upper bound $X_A = 1$ results in an Otto cycle; the lower bound $X_A = 0$ results in a Diesel cycle. The air excess ratio is modelled using:

$$\lambda = \frac{m_{\text{air,cycle}}}{\sum_{i=1}^{K} \sigma_i \cdot m_{\text{fuel,i,cycle}}} \tag{3.54}$$

Any imperfections in the scavenging process are neglected. σ is the stoichiometric air-to-fuel ratio.

Compression

The compression phase is assumed to follow the relation $Pv^{n_{\text{exp}}}$=constant to account for heat loss through the cylinder wall. Then, the pressure at point 2 is estimated using:

$$p_2 = p_1 \cdot (\frac{V_1}{V_2})^{n_{\text{exp,c}}} \tag{3.55}$$

Where the cylinder volume at point 1 and 2 is calculated using the cylinder geometry. Pressure p_1 follows from the turbocharger model. Temperature T_1 is assumed to be 328 K after the intercooler at all times. Knowing temperature P2, the temperature at point 2 is calculated with:

$$T_2 = T_1 \cdot \frac{p_2}{p_1} \frac{V_2}{V_1} \frac{Z_1}{Z_2} \tag{3.56}$$

The compressibility factor Z depends on temperature and pressure. A table of values for the compressibility factor of air for various temperatures and pressures (appendix A.3) has been extracted from REFPROP [72] and is used in a linear 2-D interpolation to determine Z. Equation 3.56 requires iteration, as $Z_2(p_2, T_2)$ is not known in advance. The model calculates T_2 (equation 3.56) based on an initial guess for Z_2 in a first iteration. Then it calculates $Z_2(p_2, T_2)$. Z_2 is used to re-calculate equation 3.56 and the obtained T_2 is used again to find a new Z_2. Once $|Z_2^{\text{old}} - Z_2^{\text{new}}| < 0.01$, iteration stops and T_2 is found. The work from point one to point two is calculated using

$$w_{1\to2} = \int_{v_1}^{v_2} p(v)\mathrm{d}v = \frac{p_2 v_2 - p_1 v_1}{1 - n^{\text{exp,c}}} = R_{\text{air}} \cdot \frac{T_2 \cdot Z_2 - T_1 \cdot Z_1}{1 - n^{\text{exp,c}}} \tag{3.57}$$

$n^{\text{exp,c}}$ is related to the heat loss through the cylinder wall and cannot be determined experimentally at this point. It is assumed that 5% of the work put in the compression stroke is lost as heat. The internal energy change during compression is determined using temperature-dependent functions for c_v obtained from NIST [4] (appendix A.2):

$$u_{1\to2} = \int_{T_1}^{T_2} c_\text{v}(T)\mathrm{d}T \tag{3.58}$$

Is used to determine the heat of the compression:

$$q_{1\to2} = u_{1\to2} + w_{1\to2} \tag{3.59}$$

The polytropic efficiency η_pol is defined by equation 3.60, of which the equivalent that assumes a constant $\kappa = \frac{c_\text{p}}{c_\text{v}}$ is described in [102, 109].

$$\eta_\text{pol} = \frac{-w_{1\to2}}{u_{1\to2}} \tag{3.60}$$

η_pol is positive for cooling during compression. A separate code has been used to iterate until the required work $-w_{1\to2}$ is 5% higher than the internal energy change of the cylinder air, $u_{1\to2}$, at nominal engine conditions.

Isochoric combustion

The temperature and pressure rises during isochoric combustion are governed by the heat input due to combusting fuel. The volume does not change during this process. Therefore, no work is associated. At elevated temperatures, the change in internal energy of air is merely governed by temperature. So:

$$u_{2\to3} = q_{2\to3} \tag{3.61}$$

$$q_{2\to3} = \int_{T_2}^{T_3} c_\text{v}(T)\mathrm{d}T \tag{3.62}$$

Where $q_{2\to3}$ is the heat released by combustion following from the heat input sub-model. Equation 3.62 is solved for T_3 using modified Newton-Raphson iteration for increased speed and NIST thermodynamic properties [4] (appendix A.2). Then, at constant volume, p_3 is determined by:

$$p_3 = p_2 \cdot \frac{T_3}{T_2}\frac{Z_3}{Z_2} \tag{3.63}$$

As during in the compression stroke, $Z_3(T_3, p_3)$ is not known in advance but the model iterates to find the correct p_3 and the corresponding T_3.

Isobaric combustion

The heat input $q_{3\to4}$ during isobaric combustion is obtained from the heat release model. Together with T_3 this is used to in the model that solves for T_4:

$$q_{3\to4} = \int_{T_3}^{T_4} c_\text{p}(T)\mathrm{d}T \tag{3.64}$$

Again, modified Newton-Raphson is used to solve for equation 3.64, which includes NIST polynomials for thermodynamic properties (appendix A.2). Then, the sub-model proceeds to calculating the associated work using T_3, T_4 and $p_3 = p_4$. Z_3 and Z_4 are obtained from interpolating table A.2 making it possible to obtain the specific volumes at point 3 and 4:

$$v_3 = Z_3 \cdot \frac{T_3 \cdot \text{R}_\text{air}}{p_3} \tag{3.65}$$

$$v_4 = Z_4 \cdot \frac{T_4 \cdot \text{R}_\text{air}}{p_4} \tag{3.66}$$

Then, the cylinder volume at point 2 is approximated using:

$$V_4 = V_3 \cdot \frac{v_4}{v_3} \tag{3.67}$$

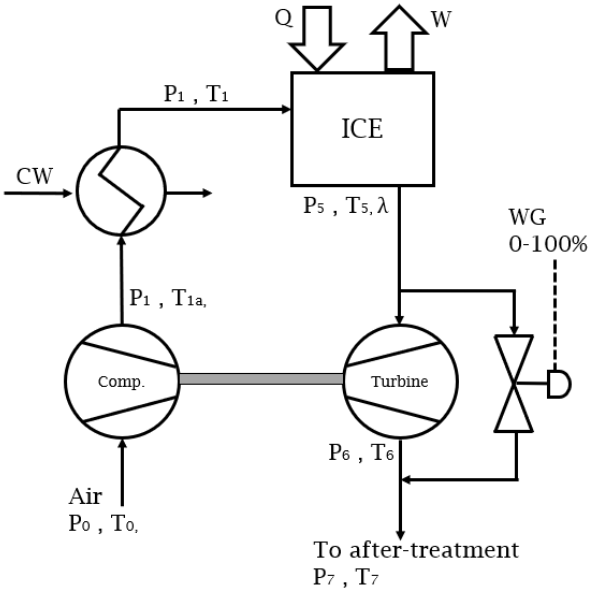

Figure 3.9: Turbocharger, ICE, intercooler and wastegate scheme.

Where $V_3 = V_2$. The specific work done on piston by the working fluid is then approximated using:

$$w_{3\to4} = \int_{v_3}^{v_4} P\mathrm{d}v = p_3 \cdot (v_4 - v_3) \tag{3.68}$$

Expansion
Useful work is obtained during the expansion stroke. Due to the high temperature of gases, an adiabatic is considered invalid to model the process. Analogues to the compression stroke, the expansion phase is assumed to follow the relation $Pv^{n_{exp}}$=constant to account for heat loss. The pressure at point 5 is then:

$$p_5 = p_4 \cdot (\frac{V_4}{V_5})^{n_{\mathrm{exp,e}}} \tag{3.69}$$

and the temperature at point 5:

$$T_5 = T_4 \cdot \frac{p_5}{p_4}\frac{V_5}{V_4}\frac{Z_4}{Z_5} \tag{3.70}$$

Where $Z_5(T_5, p_5)$ is again found by iteration. The work extracted is modelled with:

$$w_{4\to5} = \int_{v_4}^{v_5} P(v)\mathrm{d}v = \frac{p_5 v_5 - p_4 v_4}{1 - n^{\mathrm{exp,e}}} = \mathrm{R_{air}} \cdot \frac{T_5 \cdot Z_5 - T_4 \cdot Z_4}{1 - n^{\mathrm{exp,e}}} \tag{3.71}$$

The polytropic exponent, $n^{\mathrm{exp,e}}$, is not known and values found in literature cannot be used directly, as most models assume a constant ratio of specific heats. This would result in a strongly deviating heat loss compared to the literature source, as $\kappa = \frac{c_p}{c_v}$ varies throughout expansion and compression in this study. Approximately 8% heat loss is assumed during expansion. It has been verified that the corresponding polytropic exponent is 1.37 at nominal conditions.

3.2.2. Turbocharger system

The turbocharger model requires the temperature and pressure after expansion (T_5 and p_5), the air excess ratio λ, and the pressure drop over the exhaust and after-treatment system. The output is pressure p_1 of the air entering the engine and temperature T_7 after the turbine. An intercooler is present after the turbocharger and cools down the compressed air to 328 K, but its pressure drop and power consumption are neglected. The turbocharger model is based on irreversible expansion in a turbine driving a shaft. The shaft drives an irreversible compressor compressing intake air. $\kappa_{\mathrm{turbine}}$ and $\kappa_{\mathrm{compressor}}$ are kept constant along the expansion and compression stage respectively but are not equal. The change of gas mass before and after the engine is neglected in the air-standard analysis.

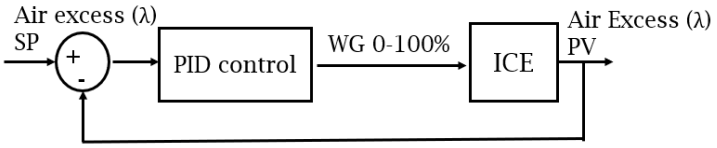

Figure 3.10: Wastegate controller structure.

Table 3.6: Turbocharger system assumptions.

Variable	Value	Unit	Description
$\eta_{\text{is,com}}$	0.7 [87]	[-]	Isentropic efficiency of compressor
$\eta_{\text{is,tur}}$	0.65 [87]	[-]	Isentropic efficiency of turbine
η_{mech}	0.9	[-]	Mechanical efficiency of turbocharger transmission
κ_{com}	1.388	[-]	$\frac{c_p}{c_v}$ at 480 K
κ_{tur}	1.364	[-]	$\frac{c_p}{c_v}$ at 700 K
T_0	298	[K]	Compressor inlet temperature
p_0	$1.015 \cdot 10^5$	[Pa]	Compressor inlet pressure
λ_{SP}	2.5	[-]	Engine air excess setpoint
τ_{tc}	20	[s]	Turbocharger time constant
T_1	328	[K]	Intercooler outlet temperature

The intake of fresh air is regulated by means of wastegate control [87]: If the air excess in the engine becomes too high, a part of the exhaust gas bypasses the turbine, which reduces the turbine work and thus the air intake. It is assumed that the pressure before the turbine equals the pressure after the expansion stroke, p_5. The pressure after the turbine p_6 is modelled as:

$$p_6 = p_{\text{atm}} + \Delta p_{\text{exhaust}} + \Delta p_{\text{SCR}} + \Delta p_{\text{ASC}} \tag{3.72}$$

The isentropic temperature ratio during turbine expansion depends on the pressure ratio of the turbine according to:

$$\frac{T_{6,\text{s}}}{T_5} = \left(\frac{p_6}{p_5}\right)^{\frac{\kappa_{\text{tur}}-1}{\kappa_{\text{tur}}}} \tag{3.73}$$

The turbine work (eq. 3.74) is transferred to the compressor (eq. 3.75) via a mechanical transmission. Combining and rearranging yields the isentropic temperature ratio across the compressor (eq. 3.76) , which is used in the compressor pressure ratio (eq. Equation 3.77). The equations obtained are also confirmed by [87].

$$\dot{W}_{\text{tur}} = \dot{W}_{\text{tur}} \cdot c_{\text{p,tur}} \cdot (T_5 - T_6) = \dot{m}_{\text{tur}} \cdot c_{\text{p,tur}} \cdot \eta_{\text{is,tur}} \cdot (T_5 - T_{6,\text{s}}) \tag{3.74}$$

$$\dot{W}_{\text{com}} = \eta_{\text{mech}} \cdot \dot{W}_{\text{tur}} = \dot{m}_{\text{com}} \cdot c_{\text{p,com}} (T_{1\text{a}} - T_0) = \dot{m}_{\text{com}} c_{\text{p,com}} \cdot \frac{T_{1\text{a,s}} - T_0}{\eta_{\text{is,com}}} \tag{3.75}$$

$$\frac{T_{1\text{a,s}}}{T_0} = 1 + \eta_{\text{is,com}} \eta_{\text{is,tur}} \eta_{\text{mech}} \cdot \frac{\dot{m}_{\text{tur}}}{\dot{m}_{\text{com}}} \cdot \frac{c_{\text{p,tur}}}{c_{\text{p,com}}} \cdot \frac{T_5}{T_0} \cdot \left(1 - \left(\frac{p_6}{p_5}\right)^{\frac{\kappa_{\text{tur}}-1}{\kappa_{\text{tur}}}}\right) \tag{3.76}$$

$$\frac{p_1}{p_0} = \left(\frac{T_{1\text{a,s}}}{T_0}\right)^{\frac{\kappa_{\text{com}}}{\kappa_{\text{com}}-1}} \tag{3.77}$$

The ratio $\frac{\dot{m}_{\text{tur}}}{\dot{m}_{\text{com}}}$ may be larger than unity without wastegate control (WGC) in reality, if fuel is added after the compressor. In the air-standard model, this is not the case; no fuel injection or combustion is modelled and $\dot{m}_{\text{tur}} = \dot{m}_{\text{com}}$ without any turbine bypass. WGC however, monitors the air excess, compares to the air excess setpoint and adjusts WG = $\frac{\dot{m}_{\text{tur}}}{\dot{m}_{\text{com}}}$ from 0 to 100% using PID control (figure 3.10). So: WG = 0 lets all exhaust gas bypass the turbine and WG = 1 lets no gas bypass. Reaching a certain air excess setpoint may be important especially in ammonia-hydrogen combustion due to the narrow flammability limits of ammonia [122].

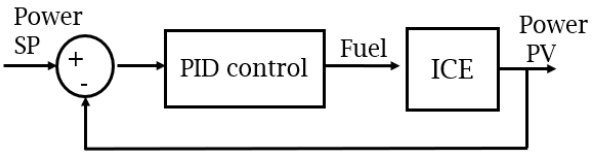

Figure 3.11: Fuel controller structure.

3.2.3. Fuel controller

The internal combustion engine model is made to be able to operate at 1-100% of nominal power. The fuel controller (figure 3.11) compares the output of the engine with the setpoint provided. If that does not match, the controller introduces more or less fuel per cycle $m_{\text{fuel,cycle}}$. In case of dual-fuel operation, only the main fuel (ammonia) is controlled by the fuel inflow controller, as the amount of hydrogen coming from the SOFC cannot be influenced directly.

3.2.4. After-treatment

It is important to note that NO_x formation is different in NH_3–H_2 combustion compared to hydrocarbon or H_2–hydrocarbon combustion [74, 96]. NO_x formation from fuel-bound nitrogen (fuel-NO_x) is more dominant than NO_x composed of nitrogen from the air (thermal-NO_x), according to Li et al. [74], which eliminates the usefulness of temperature reduction techniques against NO_x formation [96].

Different authors who studied ammonia-hydrogen ICEs report NO emissions up to 1700 ppm [46], 5000 ppm [37], 5500 ppm (for high hydrogen contents) [85], 3500 ppm [96], 4800 ppm [115] and as high as 9000 ppm at certain conditions [73]. Traditionally, NO_x is composed of more than 90% NO [45], which is confirmed by Westlye et al. where NO_x emission only includes a few percents NO_2. Other sources do not distinct NO_2 and NO [37, 46, 85, 96] or do not explain how NO and NO_2 compositions relate [97]. However, only small engines of less than 1 L displacement are used. It remains unclear how these measurements translate to large-scale marine engines. Nevertheless, 2500 ppm NO_x emissions will be incorporated in the model. SCR should reduce NO_x emissions to no more than Tier III limits, as shown in figure 2.17. These limits are provided in g/kWh; allowed ppm values depend on the fuel efficiency and air excess of the engine.

Several researchers comment on ammonia fractions present in the exhaust of ammonia–hydrogen engines. Lhuillier et al. report NH_3 emission from the engine of up to 1000 ppm (for lean conditions) [73]. Frigo and Gentili reported that NH_3 emission did not exceed 100 ppm at any time. A similar result was found in their later research [37]. Pochet et al. [97] mention that as much as 5% to 15% of the introduced NH_3 leaves unburned. Depending on the air excess, this could result in several 1000s ppm NH_3 and a severe fuel efficiency penalty. Even worse results were found in previous research from Pochet et al. [96]. Westlye et al. evaluated emissions from an ammonia–hydrogen dual-fuel SI engine and report an ammonia emission of 2000 to 2500 ppm for lean conditions and a compression ratio of 15 [115]. Ammonia slip from the SCR should be prevented. The IMO proposed a 10 ppm NH_3 limit [55] but did not implement it in Tier III regulations [3]. The EURO IV emission regulations for heavy-duty vehicles provide a guideline as well, with a maximum allowable ammonia slip of 10 ppm [2]. As Heck et al. [51] mention this value too, it is assumed that ammonia slip should be limited to 10 ppm.

No combustion modelling is performed, so it is challenging to comment on the effects of emission reduction. The air-standard model is used, so air is the working fluid and no combustion products are taken into account. To conduct a merely qualitative analysis of after-treatment effects, "artificial" emissions are added to the out-coming air stream. Simple SCR and an Ammonia Slip Catalyst (ASC) models are included to analyse the potential effects of after-treatment to reduce harmful ICE emissions. It is expected that exhaust gas from the ICE will include an excessive amounts of NO_x and, possibly, unburned NH_3 [41]. In the absence of data of marine-sized ammonia–hydrogen ICEs, NO_x and NH_3 emissions will be based on reports in literature.

The exit stream from the engine is approximated as a summation of air, NO, NO_2 and unburned ammonia. The unburned ammonia is considered to be 5% of the injected ammonia and x_{NO_x} is $2.5 \cdot 10^{-3}$ (2500 ppm) and consists of 90% NO and 10% NO_2. Both SCR and an ASC have been modelled and the structure is represented by figure 3.12.

$$\dot{N}_{\text{total}} = \dot{N}_{\text{air}} + \dot{N}_{\text{NO}} + \dot{N}_{\text{NO}_2} + \dot{N}_{\text{NH}_{3,\text{unburned}}} \tag{3.78}$$

$$\dot{N}_{\text{total}} = \dot{N}_{\text{air}} + 0.9 \cdot x_{\text{NO}_\text{x}} \cdot \dot{N}_{\text{total}} + 0.1 \cdot x_{\text{NO}_\text{x}} \cdot \dot{N}_{\text{total}} + \dot{N}_{\text{NH}_{3,\text{unburned}}} \tag{3.79}$$

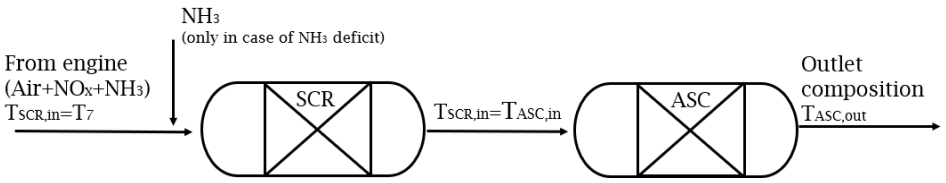

Figure 3.12: After-treatment structure.

Table 3.7: Stoichiometric coefficient ν for each component in the FSCR and SSCR reaction.

	ν_{FSCR}	ν_{SSCR}
N_2	2	1
O_2	0	$-\frac{1}{4}$
NO	-1	-1
NO_2	-1	0
NH_3	-2	-1
H_2O	3	$\frac{3}{2}$

$$\dot{N}_{\text{total}} = \frac{\dot{N}_{\text{air}} + \dot{N}_{\text{NH}_3,\text{unburned}}}{1 - x_{\text{NO}_x}} \tag{3.80}$$

Selective catalytic reduction reactor

The SCR model is a simple 0-D model of which the main goal is to examine the effect on fuel efficiency with the research questions in mind. In conventional engines where NO is the main NO_x component, SCR reaction 3.82 dominates and has an overall NH_3/NO stoichiometry of 1 [27, 45, 51]. In SCR with a conversion efficiency of less than 100%, it is important that the added number of moles of NH_3 is less than the present NO_x amount. Otherwise, ammonia will be emitted. The alternative is to remove the excess NH_3 in an additional after-treatment step, which is the method of choice in this thesis. The SCR model consists of mass- and energy balances of the fast SCR (FSCR) reaction and standard SCR (SSCR) reaction. FSCR and SSCR are assumed to happen in series. FSCR and SSCR:

$$2\text{NH}_3 + \text{NO} + \text{NO}_2 \rightarrow 2\,\text{N}_2 + 3\text{H}_2\text{O} \tag{3.81}$$

$$\text{NH}_3 + \text{NO} + \frac{1}{4}\text{O}_2 \rightarrow\ \text{N}_2 + \frac{3}{2}\text{H}_2\text{O} \tag{3.82}$$

are modelled simply using a fixed conversion of NO_2 (X_{FSCR}) in FSCR and NO (X_{SSCR}) in SSCR to avoid conducting detailed reaction modelling. Both X_{FSCR} and X_{SSCR} are assumed to be 0.9. An excess $\dot{N}_{\text{NH}_3}$ may already be present in the exhaust flow from the engine but if not: NH_3 is added to the incoming SCR flow up to a $\frac{\dot{N}_{\text{NH}_3}}{\dot{N}_{\text{NO}}+\dot{N}_{\text{NO}_2}}$ stoichiometry of 1. The SCR mass balances are then solved using equations 3.83 and 3.84:

$$\begin{aligned} \dot{N}_i^{\text{out}} &= \dot{N}_i^{\text{in}} + X_{\text{FSCR}} \cdot \nu_{i,\text{FSCR}} \cdot \dot{N}_{\text{NO}_2}^{\text{in}} \\ i &\in \{\text{N}_2, \text{O}_2, \text{NO}, \text{NO}_2, \text{NH}_3, \text{H}_2\text{O}\} \end{aligned} \tag{3.83}$$

$$\begin{aligned} \dot{N}_i^{\text{out}} &= \dot{N}_i^{\text{in}} + X_{\text{SSCR}} \cdot \nu_{i,\text{SSCR}} \cdot \dot{N}_{\text{NO}_2}^{\text{in}} \\ i &\in \{\text{N}_2, \text{O}_2, \text{NO}, \text{NO}_2, \text{NH}_3, \text{H}_2\text{O}\} \end{aligned} \tag{3.84}$$

With the stoichiometric coefficients listed in table 3.7. The SCR model operates adiabatically and its inlet temperature is the exhaust temperature from the engine. Equation 3.85 below, where $h_i^{0,\text{in}}$ and $h_i^{0,\text{out}}$ are functions of temperature, is solved for T^{out} to determine the outlet temperature. NIST properties [4] are used to determine enthalpies (appendix A.2).

$$\begin{aligned} 0 &= \sum_{i=1}^{4} (\dot{N}_i^{0,\text{in}} h_i^{0,\text{in}} - \dot{N}_i^{0,\text{out}} h_i^{0,\text{out}}) \\ i &\in \{\text{N}_2, \text{O}_2, \text{NO}, \text{NO}_2, \text{NH}_3, \text{H}_2\text{O}\} \end{aligned} \tag{3.85}$$

Table 3.8: Stoichiometric coefficient ν for each component in the ammonia slip catalyst.

	ν_1	ν_2	ν_3
N_2	$\frac{1}{2}$	0	0
O_2	$-\frac{3}{4}$	-1	$-\frac{5}{4}$
NO	0	0	1
NO_2	0	0	0
NH_3	-1	-1	-1
H_2O	$\frac{3}{2}$	$\frac{3}{2}$	$\frac{3}{2}$
N_2O	0	$\frac{1}{2}$	0

The pressure drop across the SCR system, Δp_{SCR}, is assumed to increase linearly with engine power. The pressure drop at nominal power output, 30 millibar, is based on a brochure from the engine manufacturer WingD [117].

Ammonia Slip Catalyst

An ammonia slip catalyst reactor is included in the system model to prevent ammonia slip. Three reactions are assumed to take place in parallel. Ammonia oxidises to nitrogen in the desired reaction, but N_2O are produced as well. Laughing gas (N_2O) is 300 times stronger than carbon dioxide, so its emission should be kept at a minimum.

$$NH_3 + \frac{3}{4}O_2 \rightarrow \frac{1}{2}N_2 + \frac{3}{2}H_2O \tag{3.86}$$

$$NH_3 + O_2 \rightarrow \frac{1}{2}N_2O + \frac{3}{2}H_2O \tag{3.87}$$

$$NH_3 + \frac{5}{4}O_2 \rightarrow NO + \frac{3}{2}H_2O \tag{3.88}$$

The mass balances are solved with equation 3.89 using the stoichiometric coefficients in table 3.8.

$$\begin{gathered} \dot{N}_i^{\text{out}} = \dot{N}_i^{\text{in}} + \sum_{j=1}^{3} Y_j \cdot \nu_{i,j} \cdot \dot{N}_{\text{NH}_3}^{\text{in}} \\ i \in \{N_2, O_2, NO, NO_2, NH_3, H_2O, N_2O\} \\ j \in \{\text{ASC reaction 1}, \text{ASC reaction 2}, \text{ASC reaction 3}\} \end{gathered} \tag{3.89}$$

Colombo et al. observe 100% conversion above approximately 300°C. It is assumed that all ammonia is converted in one of the products of the previous reactions, so the sum of all yields is 1:

$$\sum_{j=1}^{3} Y_j = 1 \tag{3.90}$$

Y_j is varies greatly with temperature, as seen in [36]. Higher temperatures result in a lower laughing gas yield (Y_2) [36]. The N_2, N_2O and NO yields (Y_1, Y_2, Y_3) are assumed to be 0.5, 0.05 and 0.45 following the results of Colombo et al. at 400°C in fig. 12 in [36]. 400°C has been chosen, as this is on the conservative side compared to the exhaust gas temperatures found in the ammonia-hydrogen ICE simulations (figure 4.18). The temperature at the ASC exit is determined by solving equation 3.91 for $h_i^{0,\text{out}} = f(T^{\text{out}})$, again using NIST properties [4] (appendix A.2).

$$\begin{gathered} 0 = \sum_{i=1}^{4} (\dot{N}_i^{0,\text{in}} h_i^{0,\text{in}} - \dot{N}_i^{0,\text{out}} h_i^{0,\text{out}}) \\ i \in \{N_2, O_2, NO, NO_2, NH_3, H_2O, N_2O\} \end{gathered} \tag{3.91}$$

The pressure drop across the ASC is assumed to be the same as the pressure drop across the SCR.

3.2.5. Power output and efficiency

The work obtained per kg working fluid is simply:

$$w_{\text{cycle}} = w_{1\rightarrow 2} + w_{3\rightarrow 4} + w_{4\rightarrow 5} \tag{3.92}$$

The torque developed is related to the mass of air introduced per cycle, $m_{\text{air,cycle}}$:

$$T = m_{\text{air,cycle}} \cdot w_{\text{cycle}} \cdot \frac{i}{2\pi k} \tag{3.93}$$

The model then calculates the engine power and subtracts 5% of the nominal engine power to account for mechanical losses. As the engine runs at a constant speed, the mechanical losses are assumed to be constant over the complete load profile.

$$P_{\text{ICE}} = T \cdot N \cdot 2\pi - 0.05 \cdot P_{\text{nom}} \tag{3.94}$$

Section 4.2 gives the results of the internal combustion engine, and makes use of three distinct efficiencies. The mechanical efficiency is defined as:

$$\eta_{\text{mech,ICE}} = \frac{P_{\text{mech,ICE}}}{\dot{m}_{\text{mainfuel}} \cdot \text{LHV}_{\text{mainfuel}} + \dot{m}_{\text{H}_2} \cdot LHV_{\text{H}_2}} \tag{3.95}$$

Where the mass flow of the main fuel is usually ammonia, but sometimes methane. If methane is used, no hydrogen is added. The thermal efficiency excludes mechanical losses and makes use of the work and fuel mass flow per cycle.

$$\eta_{\text{thermal,ICE}} = \frac{w_{\text{cycle}}}{m_{\text{mainfuel}} \cdot \text{LHV}_{\text{mainfuel}} + m_{\text{H}_2} \cdot \text{LHV}_{\text{H}_2}} \tag{3.96}$$

The electrical system efficiency of the engine includes the ammonia consumed during selective catalytic reduction, too. The power output is corrected by 95% generator efficiency.

$$\eta_{\text{ICE}} = \frac{\eta_{\text{generator}} \cdot P_{\text{mech,ICE}}}{\dot{m}_{\text{mainfuel}} \cdot \text{LHV}_{\text{mainfuel}} + \dot{m}_{\text{H}_2} \cdot \text{LHV}_{\text{H}_2} + \dot{m}_{\text{NH}_3,\text{SCR}} \cdot LHV_{\text{NH}_3}} \tag{3.97}$$

An ICE system operating as a standalone system cannot receive its hydrogen from an SOFC. However, ammonia can be cracked to hydrogen and nitrogen to heat the external cracker, in a hypothetical standalone (SA) configuration. 90% of total the hydrogen off-gas lower heating value is subtracted from the required heat in the external cracker to yield a standalone efficiency. The standalone electrical system efficiency of the engine is defined as:

$$\eta_{\text{ICE,SA}} = \frac{\eta_{\text{generator}} \cdot P_{\text{mech,ICE}}}{\dot{m}_{\text{mainfuel}} \cdot \text{LHV}_{\text{mainfuel}} + \dot{m}_{\text{H}_2} \cdot \text{LHV}_{\text{H}_2} + \dot{m}_{\text{NH}_3,\text{SCR}} \cdot LHV_{\text{NH}_3} + \dot{m}_{\text{NH}_3,\text{crackerheat}} \cdot LHV_{\text{NH}_3}} \tag{3.98}$$

Only one fuel type is included in the brake specific fuel consumption ($bsfc$) in g/kWh. It provides insight into the mass of fuel consumed, so fuels with different lower heating values should not be combined.

$$bsfc = \frac{\dot{m}_{\text{fuel}} \cdot 3600 \cdot 10^6}{P_{\text{ICE}}} \tag{3.99}$$

3.3. Hybrid system

The hybrid system (figure 3.14) is the combination of the SOFC system and the ICE system. The most important design choice is that the transfer of hydrogen from the SOFC to the ICE is the only inter-dependency. Water is condensed from the anode off-gas stream and the remaining hydrogen and nitrogen are lead to the ICE. This limited degree of integration reduces system complexity and increases the feasibility of part load and dynamic operation of the hybrid system in a real marine application. The MATLAB & Simulink model is made by combining the SOFC and ICE models in one single model (figure 3.13).

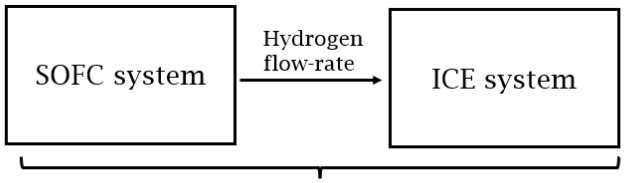

Figure 3.13: Structure of the hybrid model.

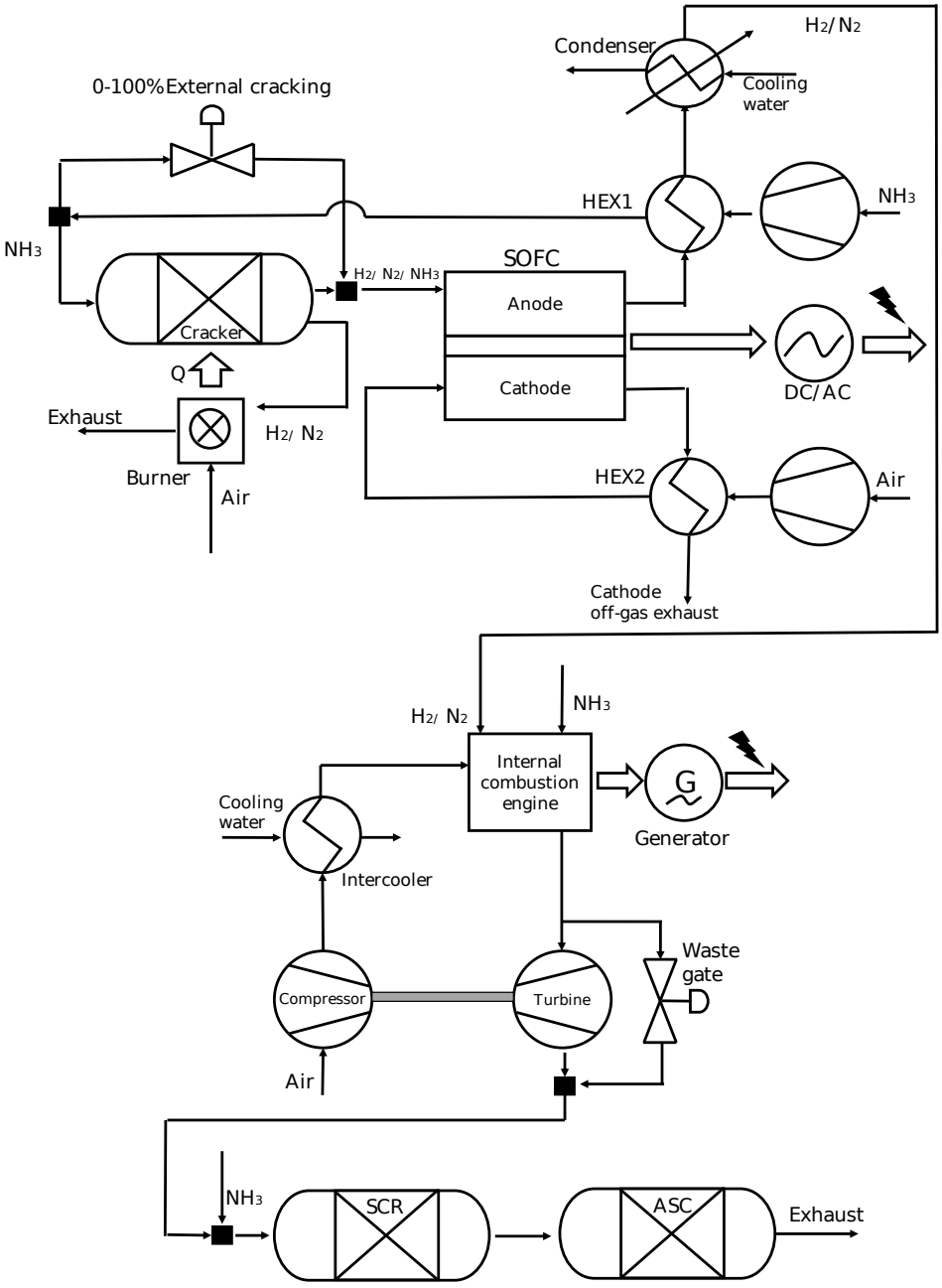

Figure 3.14: Schematic representation of the hybrid SOFC–ICE system.

Table 3.9: Power outputs of the different power splits of the hybrid system.

	$PS = 50/50$	$PS = 25/75$	$PS = 75/25$	unit
$P_{\text{SOFC,AC}}$	6,840	2,280	20,520	kW
$P_{\text{ICE,AC}}$	6,840	6,840	6,840	kW

One of the goals of this research is to analyse and compare systems with different divisions of power between the SOFC stack and the ICE. Three different power splits will be tested: One in which the SOFC and ICE power are equal (50%/50%), one power split favouring the ICE (25%/75%) and one power split favouring the SOFC (75%/25%). The SOFC model is scaled by adapting the number of cells N_{cells}, while the engine model stays the same (table 3.9). The power split is based on the electrical power (AC) of both systems, as is the hybrid system efficiency:

$$\eta_{\text{hybrid}} = \frac{P_{\text{system}}}{\dot{N}_{\text{NH}_3,\text{system}} \cdot \text{LHV}_{\text{NH}_3}} \tag{3.100}$$

4

Results

The results chapter is split into three parts:

- Section 4.1 characterises the behaviour of the ammonia-fuelled SOFC (system) model and compares it to literature.
- Section 4.2 highlights the performance of the ammonia-fuelled ICE (system) model and compares it to technical data of the Wärtsilä 12V31DF (on which the ICE model is based) from the manufacturer.
- Section 4.3 is of major importance as it provides the results of the hybrid system simulations. The hybrid system has been tested in three configurations: 50/50, 25/75 and 75/25 SOFC/ICE power split.

Results have been collected after simulations reached steady-state.

4.1. Solid oxide fuel cell system

A sensitivity analysis is performed to assess the effect of fuel utilisation, temperature and fuel composition on the output voltage, power density, electrical efficiency and cathode air demand of individual cells. This is described in section 4.1.1. Then, the behaviour of the SOFC model is compared to the results of the model developed by Aguiar et al. [14] and experiments on ammonia fuelled SOFCs by Kishimoto et al. [64] and Cinti et al. [35] to validate the model in section 4.1.2. Section 4.1.3 comments on air and fuel blower power, before the efficiency and heat management of the SOFC system containing $2.02 \cdot 10^5$ fuel cells, an external cracker and blowers are elucidated. Low current densities are used to analyse the stack performance in all three sections, but they are considered to be of limited importance in the hybrid system studied in section 4.3.

4.1.1. Performance of individual cells

A first evaluation of the stack has been done by comparing different sources of hydrogen as a fuel for the stack. Figure 4.1 does not show a notable difference. An important characteristic of the mass balance model is that all incoming ammonia decomposes directly as it enters the stack, which avoids a thorough evaluation of reaction kinetics. Whether pure NH_3 or an equivalent N_2/H_2 mixture is added has no influence on the computed partial pressures: the anode concentration loss and Nernst potential remain unaffected. Besides, the computed concentration losses account for only a limited part of the total losses (see figure 2.3).

Table 4.1: Constant parameters throughout the simulations. * The percentage heat loss in the stack is relative to the amount of heat that would otherwise all have been absorbed by the anode and cathode gases as sensible heat.

Parameter	Value	Unit	Description
p_{amb}	$1.015 \cdot 10^5$	Pa	Ambient pressure
p_{ca}	$1.015 \cdot 10^5$	Pa	Cathode pressure
p_{an}	$1.015 \cdot 10^5$	Pa	Anode pressure
k	1.4	–	Ratio of specific heats
Heat loss	5	%	Percentage heat loss in the stack*

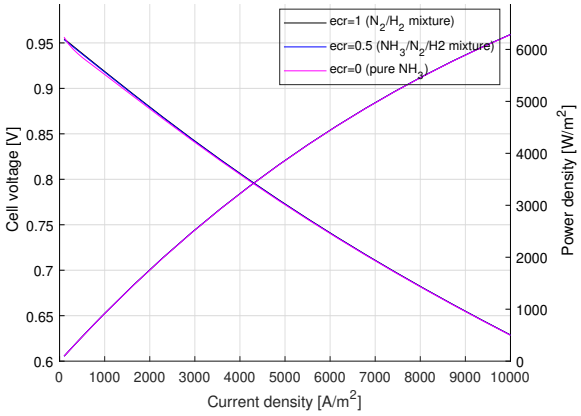

Figure 4.1: Cell voltage and power density at a fixed fuel utilisation (80%) and a fixed temperature setpoint (800°C) versus current density for three different external cracking ratios.

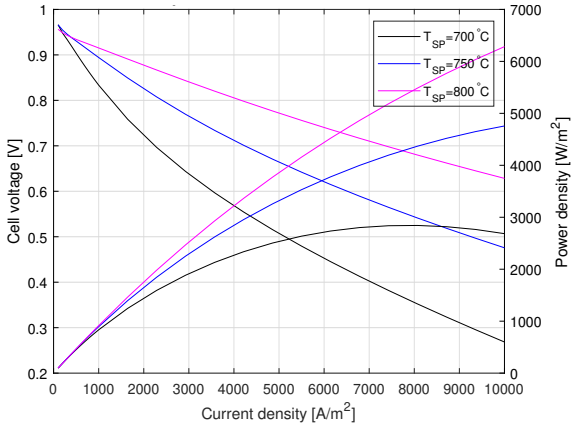

Figure 4.2: Cell voltage and power density at a fixed fuel utilisation (80%) and external cracking ratio (0), so pure NH_3, versus current density for three different temperatures.

Secondly, a sensitivity analysis has been conducted to evaluate the effect of temperature, which is important for the cell performance (figure 4.2) as the ionic resistance of the electrolyte decreases for increasing temperature. The effect of temperature on electronic resistance is neglected in this study. 800°C is chosen as the design, or reference temperature, due to the superior voltage and power density compared to lower temperatures.

The performance difference for various fuel utilisations (figure 4.3) is caused by a variation in partial pressures, affecting the Nernst potential and anode concentration losses. The curve flips below 4000 $A \cdot m^{-2}$ for 50% fuel utilisation ($UF = 0.5$) because the cell does not achieve 800°C due to the cooling capacity of the high fuel flow. This increases cell losses.

Figure 4.4 shows a representation of the different loss mechanisms in the cell. It is seen that, as temperature increases, the decay of activation losses is the main driver for the increase in cell voltage.

Insufficient heat is produced to maintain the desired operating temperature setpoint at low current densities. Operating temperature setpoints are used throughout all results instead of "actual" temperatures. This is not a problem unless the actual temperature does not match the operating temperature setpoint. The plot in figure 4.5 has been generated to show when this happens. A minimum current density of $\pm$ 500 $A \cdot m^{-2}$ is required to ensure that the operating temperature setpoint (800°C) is reached, in the most extreme case. A more severe problem at low current densities is that the thermal response of the stack becomes extremely slow because of the small amount of heat dissipated. It was first expected that the model would reach steady-state within an hour, easily. However, at sub-1000 $W \cdot m^{-2}$ the model's behaviour is far from optimal.

The cathode airflow is set by a temperature controller trying to maintain the operating temperature setpoint. Figures B.19 and B.21 (appendix B.3) show a response of the temperature controller output when the initial stack temperature is not equal to T_{SP}. The endothermic nature of the ammonia decomposition decreases the cooling air requirement compared to fuelling pre-decomposed ammonia. The air excess ratio,

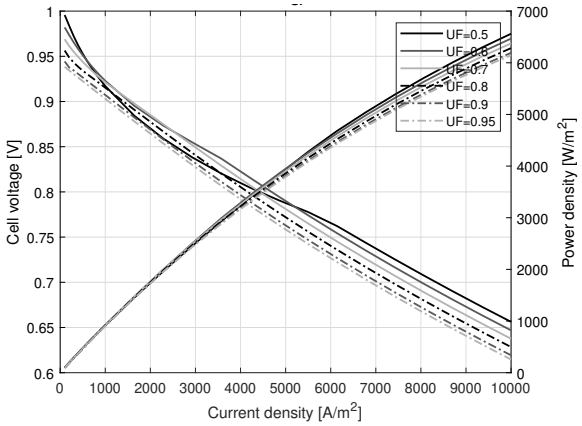

Figure 4.3: Cell voltage and power density at a fixed temperature setpoint (800°C) and external cracking ratio (0), so pure NH_3, versus current density for six different fuel utilisations.

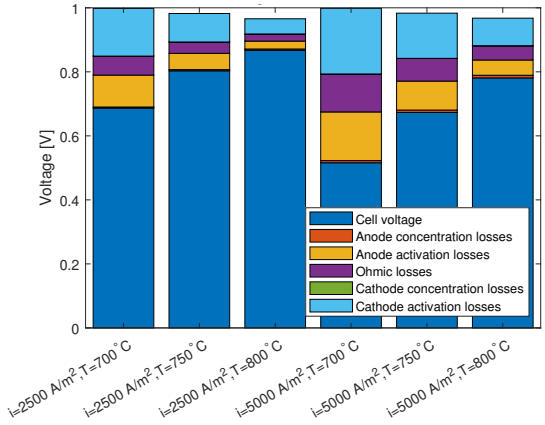

Figure 4.4: Cell voltage and loss mechanism for direct NH_3 and a 70% fuel utilisation.

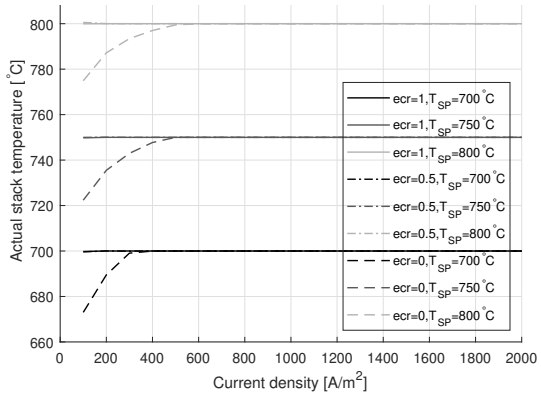

Figure 4.5: The average cell temperature calculated by the model at a fixed fuel utilisation (80%) versus current density for three different temperature setpoints and different external cracking ratios.

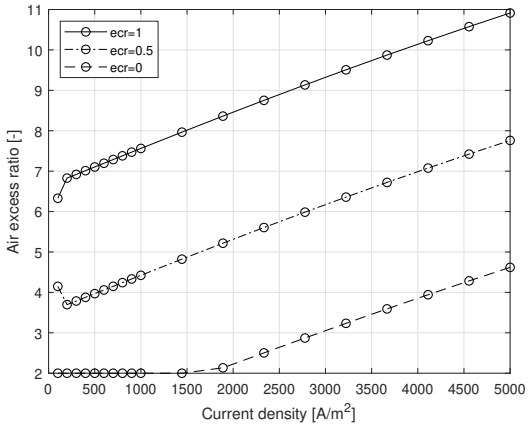

Figure 4.6: Cathode airflow at $T_{SP} = 800°C$ and $UF = 0.7$.

Table 4.2: Electrical efficiency of the cell with fully pre-decomposed ammonia at different operating points.

$T = 800°C, ecr = 0$	V_{cell}	P_{cell}	η_{cell}	$\eta_{cell,corrected}$
$UF = 0.5, i = 5000$	0.788	39.38	0.360	0.832
$UF = 0.5, i = 8334$	0.700	58.37	0.320	0.739
$UF = 0.7, i = 5000$	0.781	39.05	0.499	0.757
$UF = 0.7, i = 7675$	0.700	53.73	0.447	0.679
$UF = 0.9, i = 5000$	0.763	38.15	0.627	0.707
$UF = 0.9, i = 7040$	0.700	49.28	0.575	0.649

not allowed to drop below 2, is shown in figure 4.6. Logically, 100% externally cracked ammonia requires the least cathode air.

The cell efficiency for a number of operating points is depicted in tables 4.2 and 4.3. The "regular" cell efficiency exceeds 50% for high fuel utilisations. The highest "corrected" cell efficiency (equation 3.42) reaches 83% for $ecr = 0$ (pure ammonia), compared to 66% for $ecr = 1$ at T_{SP} 800°C and 50% fuel utilisation. The reason for the large efficiency difference between pure ammonia and decomposed ammonia is because the LHV of ammonia per hydrogen molecule is higher than for hydrogen itself; cracking ammonia is endothermic and requires energy. It is beneficial if this is done in the SOFC.

4.1.2. Validation of the SOFC model

Comparison to the modelling research of Aguiar et al.

The I-V and I-P curves of the 0-D SOFC model discussed in the previous chapter are used as a starting point to evaluate the SOFC model. The developed model is based on [61], so only one temperature layer is used. This is in contrast to [14], where heat transfer between PEN structure, air channel, fuel channel and interconnect were taken into account. Also, variation along stream direction is not taken into account in the SOFC model, but the only includes the inlet and exit conditions, which are averaged if necessary. All SOFC properties (table 3.2) have been taken from [14], as explained in subsection 3.1.3. The SOFC model was run at operating temperature setpoints of 700, 750 and 800°C. $ecr = 1$ has been used as input to the model, so fully cracked ammonia entered the stack as an equivalent N_2/H_2 mixture.

Table 4.3: Electrical efficiency of the cell with direct ammonia at different operating points.

$T = 800°C, ecr = 1$	V_{cell}	P_{cell}	η_{cell}	$\eta_{cell,corrected}$
$UF = 0.5, i = 5000$	0.803	40.15	0.323	0.656
$UF = 0.5, i = 8416$	0.700	58.91	0.282	0.563
$UF = 0.7, i = 5000$	0.782	39.12	0.441	0.629
$UF = 0.7, i = 7703$	0.700	53.92	0.394	0.563
$UF = 0.9, i = 5000$	0.764	38.18	0.553	0.614
$UF = 0.9, i = 7057$	0.700	49.40	0.507	0.563

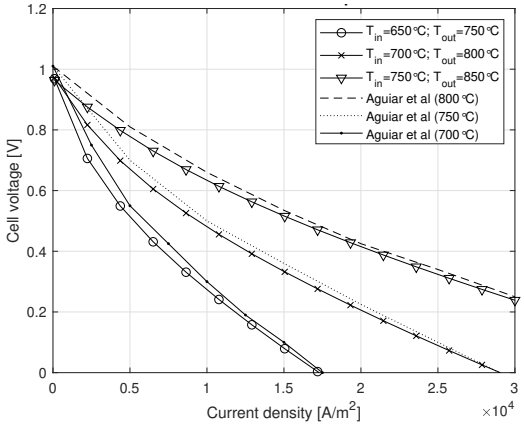

Figure 4.7: I-V curve for 100% externally cracked ammonia (N_2/H_2 mixture) and fully pre-reformed methane acquired from [14]. Both are operated at 75% fuel utilisation. Max. ± 0.01 V reading error from [14] fig. 3.

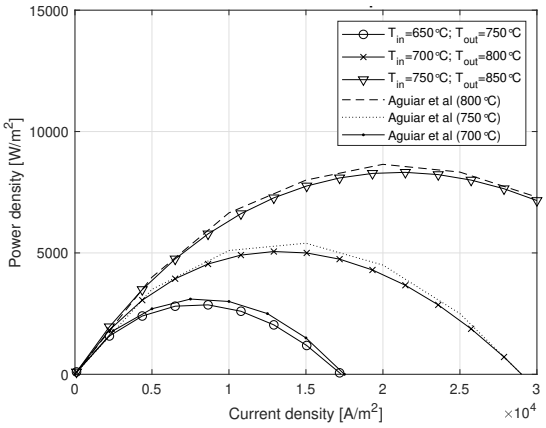

Figure 4.8: I-P curve for 100% externally cracked ammonia (N_2/H_2 mixture) and fully pre-reformed methane acquired from [14]. Both are operated at 75% fuel utilisation. Max. ± 100 $W \cdot m^{-2}$ reading error from [14] fig. 4.

The results are displayed in figure 4.7 and 4.8 and compared to the results obtained by [14] for current densities up to $30 \cdot 10^3$ $A \cdot m^{-2}$. This is unrealistically high for practical applications but is considered useful for assessing the model. In figures 4.7 and 4.8 it is observed that, especially for current densities above $5 \cdot 10^3$ $A \cdot m^{-2}$, the curves show similar behaviour, which is an indication that the simplifications made in the model compared to [14] are justified to at least some extent.

Figure 4.9 highlights the different loss mechanisms occurring in the SOFC model. Cathode concentration losses are negligible for the full operating range. The simple reason is that only a small fraction of the oxygen introduced is utilised in the fuel cell for these operating conditions, as excess air is present for cooling purposes. That excess of air is elaborated on later. Activation losses in the anode appear to be comparable to ohmic losses. They are the major source of losses in the cell together with the cathode activation losses. The share of anode concentration losses is limited. Its relative contribution should rise for high current densities, but this cannot be read from the graphs.

The losses found in [14] are included in figure 4.9 as well. It is easily seen that there is a 0.03 V offset in open-circuit voltage. A reason could be the use of an averaged composition from inlet to outlet in the SOFC model in this study, while Aguiar et al. appear to use the inlet composition of fuel and air. All loss types except the anode activation losses show very similar behaviour but the anode activation losses are larger in the model from Aguiar et al.. The explanation may be that Aguiar et al. use an extended Butler–Volmer equation for the anode activation overpotential [14], in contrast to this study. The difference in open-circuit voltage and anode activation losses cancel each other for moderate current densities in figure 4.7 and 4.8, so figure 4.9 provides an important insight into how the models compare.

Comparison to experimental research of Kishimoto et al.
The SOFC model is compared to experimental results obtained by different authors. The first and most rele-

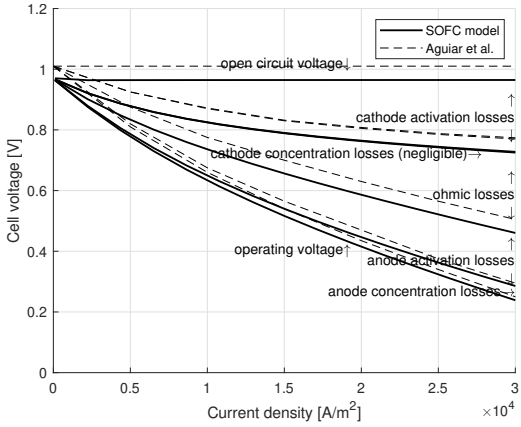

Figure 4.9: Different loss mechanisms for 100% externally cracked ammonia (N_2/H_2 mixture) and fully pre-reformed methane acquired from [14]. Both are operated at 75% fuel utilisation. The loss mechanisms are the differences between the curves. Max. ± 0.01 V reading error from [14] fig. 4.

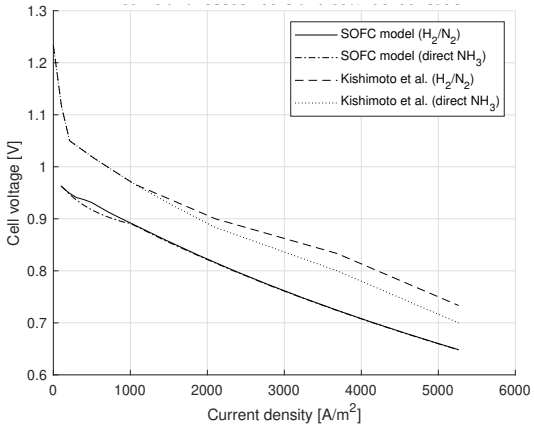

Figure 4.10: I-V curved for cracked ammonia (N_2/H_2 mixture) and direct ammonia NH_3 for this study and [65]. Both are operated at 85% fuel utilisation. Max. ± 0.01 V reading error from [64] fig. 3.

vant study has been developed by Kishimoto et al., who performed experiments with a 1 kW scale ammonia-fuelled SOFC stack with 30 anode-supported cells. The SOFC model was run for similar conditions as in [64]: 750°C, 85% fuel utilisation and for 0% and 100% pre-decomposed ammonia. Results are depicted in figure 4.10 and table 4.4, where it is seen that the predicted cell voltage is approximately 10% higher in the experiments performed by [64]. The performance of pre-decomposed ammonia in terms of voltage output is better than direct ammonia. This is in accordance with [64]. However, [64] attributes this to a decrease in stack temperature, while stack temperature is kept at a fixed value in the SOFC model, no matter if direct or pre-decomposed ammonia is added. There are large differences in temperature management between the current study and [64]. The SOFC model pre-heats air and fuel and maintains a fixed operating temperature by adapting the cathode airflow for cooling. [64] does not state whether the incoming streams are pre-heated, and the SOFC is kept at the right temperature using an electric furnace. Table 4.4 highlights the large difference in airflow.

Comparison to the experimental research of Cinti et al.
The SOFC model has been tested and compared to the experimental results from Cinti et al. [35]. Some striking differences are seen in figure 4.11. There is a considerable difference in OCV. It is not known whether one distinct reason exists. Some explanations are thought of:

- It is not found at what fuel utilisation the authors are operating the stack. At low fuel utilisations, the partial pressures of the fuel are higher which should result in an increased OCV.
- The authors use a furnace [35] to reach the desired stack temperature while the SOFC model pre-heats air and maintains its temperature due to reaction heat and losses. Moreover, there is a chance that

Table 4.4: Cell voltage, power density, air excess and cathode airflow for the SOFC model and [64] at the maximum reported current density of [64]. *: The cells of the SOFC measure 100 cm^2. The cells of [64] have a reported active area of 95 cm^2.

$i = 5263\ A \cdot m^{-2}$	Unit	SOFC model	Kishimoto et al. [64]
V_{cell} (H_2/N_2)	V	0.65	0.73
V_{cell} (NH_3)	V	0.65	0.70
p_{cell} (H_2/N_2)	$W \cdot m^{-2}$	$3.41 \cdot 10^3$	$3.86 \cdot 10^3$
p_{cell} (NH_3)	$W \cdot m^{-2}$	$3.41 \cdot 10^3$	$3.68 \cdot 10^3$
Air excess ratio (H_2/N_2)	–	13.80	2
Air excess ratio (NH_3)	–	8.99	2
Cathode airflow per cell* (H_2/N_2)	$L \cdot min^{-1}$	14.20	1.67
Cathode airflow per cell* (NH_3)	$L \cdot min^{-1}$	8.40	1.67

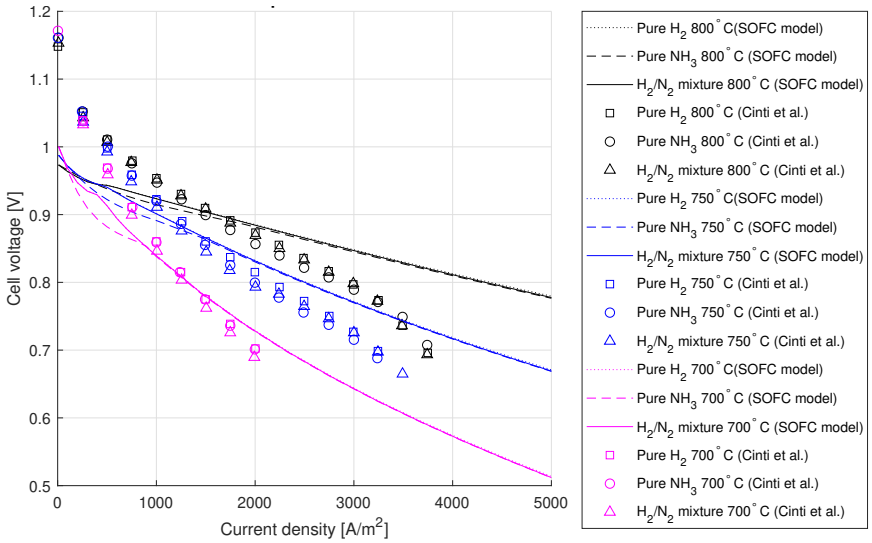

Figure 4.11: I-V curves for pure H_2, pure NH_3 and an equivalent N_2/H_2 mixture for a 700, 750 and 800°C temperature setpoint. The fuel utilisation of the SOFC model is 75% and the fuel utilisation of the experiments in [35] is not known.

fuelling direct NH_3 has such a strong cooling effect in [35] that it elevates the open-circuit voltage. The latter is considered unlikely as thermocouples monitor the temperature [35].

- The SOFC model is not suitable to be run at near-zero current densities as it disturbs system functioning, such the heat management.

- The Nernst equation, 2.3), used in the SOFC model may not suffice in describing the complex processes happening in the cell at OCV.

- The authors briefly mention that the dilution of fuel by nitrogen could have a positive effect on the OCV [35] which is not in accordance with the Nernst equation used in the model. The authors attribute this to "gas distribution and inlet gas speed" [35] but do not provide an explanation.

The cell voltage of [35] drops faster than in the SOFC model but he stack performance greatly depends on the manufacturer-specific cell properties. The SOFC model stack may simply outperform the stack used by [35]. This is supported by the observation that Kishimoto et al. [64] use a different stack and report higher cell voltages than this study. Cinti et al. [35] mention a maximum voltage difference between the polarisation curves in the order of 0.1% to 2%, which is in accordance with the results of the SOFC model for current densities higher than 1000 $W \cdot m^{-2}$. For lower current densities, the stack temperature of the direct ammonia simulations does not always reach the desired operating temperature due to the cooling effect of the ammonia decomposition reaction.

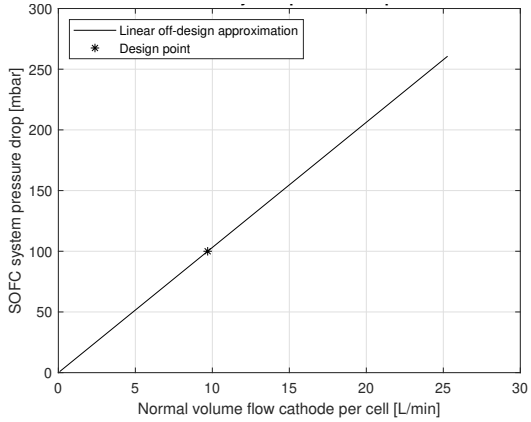

Figure 4.12: Cathode system pressure drop (design point set at $ecr = 1$, $i = 5000$, $UF = 0.7$; $T = 800°C$).

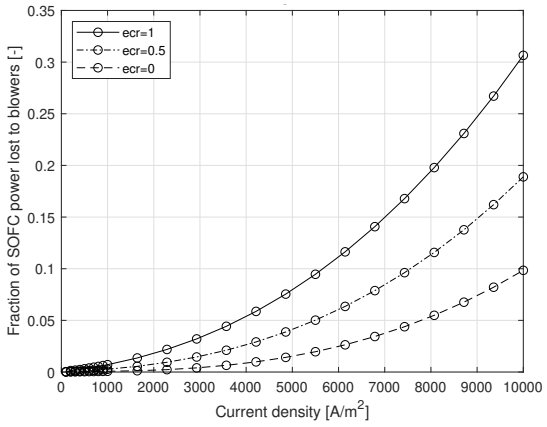

Figure 4.13: Required power to drive the air and fuel blowers relative to the SOFC power. $UF = 0.7$; $T = 1073$ K).

4.1.3. SOFC system performance

Air and fuel blowers

The work required to let the air flow through the SOFC system is known to be the most prominent source of power loss in the system. As mentioned in the methodology, the pressure drop is linearly extrapolated from the SOFC system design point to account for a pressure drop that varies with the cathode airflow. This is shown in figure 4.12. The relation between cathode volume flow and pressure drop is considered to be independent of other parameters related to operation, so only one curve needs to be displayed.

In figure 4.13, it is seen that the type of fuel to the stack has an enormous impact on the blower power required and the impact increases for large current densities because of the (approximately) quadratic relation between current density and blower power. In the sections before, there was no very clear difference in performance between direct ammonia and hydrogen-nitrogen, but here it is clear that one would strive for a low ecr (a low degree of pre-decomposition before the stack) on a system-level. 20% of the SOFC power is lost to the blower for fully decomposed ammonia at 8000 $A \cdot m^{-2}$. This is four times as much as the blower power for direct ammonia. At 5000 $A \cdot m^{-2}$, however, the blower power has already dropped below 10%. In light of the system efficiency one should be careful not to operate on a too high-current density (if possible at all, due to technical constraints in the cell).

Efficiency and heat management

A number of operating points of the SOFC system has been simulated. The number of cells (202,620) has been chosen such that the net power output is 7.2 MW at 70% fuel utilisation, 5000 $A \cdot m^{-2}$ and 50% external cracking. Important results concerning the efficiency are shown in table 4.5. Purely looking at η_{SOFC}, it is evident one should strive for a high fuel utilisation as this wastes less fuel. This may be different in the hybrid system because it uses the hydrogen off-gas in the engine.

Cracking inside the SOFC stack has a major impact on system efficiency. The main reason is that less external heat has to be supplied to the cracker reactor before the stack. A strong reduction in (air) blower

Table 4.5: SOFC system efficiency for a system with $2.02 \cdot 10^5$ fuel cells.

T_{SP} = 1073 K, $ecr = 0$	P_{system} [MW]	$P_{blowers}$ [MW]	η_{SOFC} [%]	$\eta_{SOFC,gross}$ [%]	$\eta_{SOFC,SA}$ [%]
$UF = 0.5, i = 5000$	7.53	0.05	33.9	33.9	33.9
$UF = 0.7, i = 5000$	7.4	0.12	46.7	46.7	46.7
$UF = 0.9, i = 5000$	7.12	0.23	57.7	57.7	57.7
T_{SP} = 1073 K, $ecr = 0.5$					
$UF = 0.5, i = 5000$	7.5	0.22	30.7	33.8	33.8
$UF = 0.7, i = 5000$	7.2	0.33	41.3	45.4	45.4
$UF = 0.9, i = 5000$	7.0	0.42	51.0	56.2	56.2
T_{SP} = 1073 K, $ecr = 1$					
$UF = 0.5, i = 5000$	7.14	0.59	26.8	32.2	32.2
$UF = 0.7, i = 5000$	6.9	0.63	36.2	43.5	43.5
$UF = 0.9, i = 5000$	6.67	0.68	45	54.1	49.9

power is seen as well when ammonia is cracked internally.

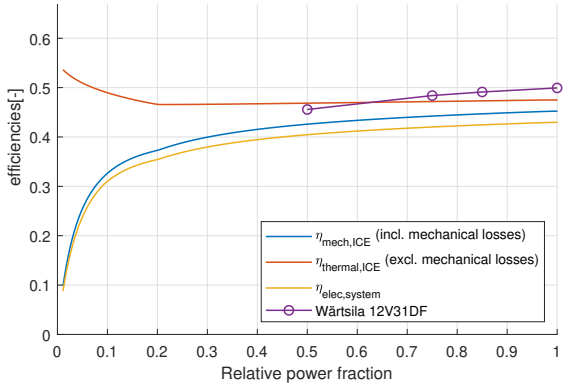

Figure 4.14: The efficiency of the ICE model with a 70 mol% NH_3 and 30% H2 dual-fuel.

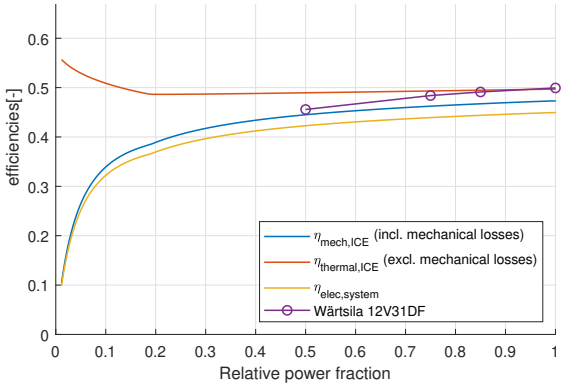

Figure 4.15: The efficiency of the engine with 100% gas (methane) fuel.

4.2. Internal combustion engine system

The model has been run from 100% to 1% load to assess the performance of the engine. 100% load is equal to 7200 kW mechanical power, which is converted into 6840 kW electrical power with 95% generator efficiency.

Section 4.2.1 comments on the ICE model results. The fuel efficiency, exhaust gas temperature and combustion air inlet mass flow of the ICE model are compared to manufacturer data of the Wärtsilä 12V31DF. The ICE model is not only fuelled with a 70%/30% ammonia-hydrogen blend, but also with natural gas (assumed to be pure methane). The latter provides a more appropriate way to compare the engine model with the real engine: the real Wärtsilä 12V31DF operates on HFO, marine diesel fuel or natural gas. It requires a pilot fuel in natural gas mode, which is, however, not included in the ICE model.

Section 4.2.2 describes the ICE emissions and the results of the after-treatment model.

4.2.1. ICE performance and validation

Efficiency and fuel consumption

Figures 4.14 and 4.15 show the engine efficiencies extracted from the ICE model. In the curve "$\eta_{\text{incl,SCR}}$", the LHV ammonia consumption in the SCR has been included in the efficiency. The electrical efficiency is over 40%: This is relatively high for an internal combustion engine, but it is less than the reported efficiency of the Wärtsilä 12V31DF in dual-fuel gas mode. Assuming that 5% of ammonia remains unburned accounts plays a role in the difference between the ICE model and the real Wärtsilä engine. It does not matter whether or not the ammonia consumed in the SCR is taken into account: the right amount of unburned ammonia is already present in the exhaust stream to react with the NO_x formed under the assumptions taken.

The mechanical losses, assumed constant along throughout the complete load profile, start to dominate the system performance towards lower power fractions. This pushes the engine efficiency towards zero load. There is an odd-shaped upward move in the thermal efficiency curve seen in the graph. Below approximately 21% power, all exhaust gas bypasses the turbine and the wastegate cannot open any further. While the air excess setpoint cannot be maintained below this point, it does positively impact the efficiency.

Figure 4.16 displays the molar fuel inflow of hydrogen and ammonia to the ICE model and is useful to verify that the desired dual-fuel mixing ratios have been obtained. Figure 4.17 presents the $bsfc$ of ammonia and hydrogen entering the ICE and the ammonia used as a reducing agent in the SCR. Excess ammonia is in the exhaust stream to the SCR as no extra ammonia is consumed in the SCR for all loads above approximately 500 kW.

Maximum in-cylinder temperature

The calculated maximum in-cylinder temperature (figures B.1 and B.2 in appendix B) is relatively constant from 20% to 100% power, which is due to the waste-gate controller controlling the air excess in this area. Applying ammonia-hydrogen increases the maximum in-cylinder temperature by 50 K compared to methane. The temperature, just below 2000 K, is on the high side according to [109] (Chapter 3.3.6). The exclusion of fuel mass in the thermodynamic cycle may have overestimated the temperature rise in the cylinder, but a high in-cylinder temperature is not considered infeasible for the Wärtsilä 12V31DF. The relatively high efficiency of the Wärtsilä 12V31DF could suggest that the manufacturer is capable of achieving high in-cylinder temperatures. Moreover, the cylinder wall will be colder.

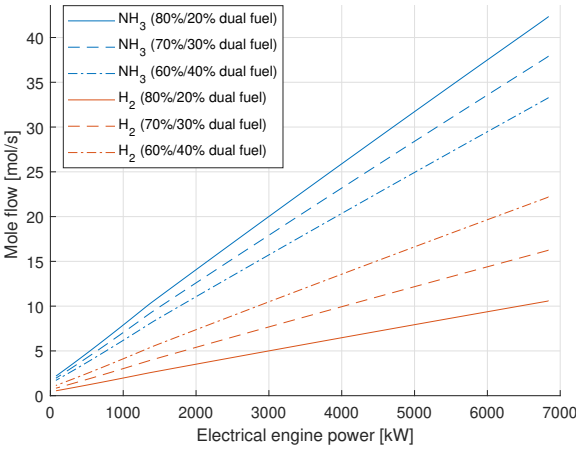

Figure 4.16: Molar fuel consumption of the ICE with different 20, 30 and 40 mol% hydrogen.

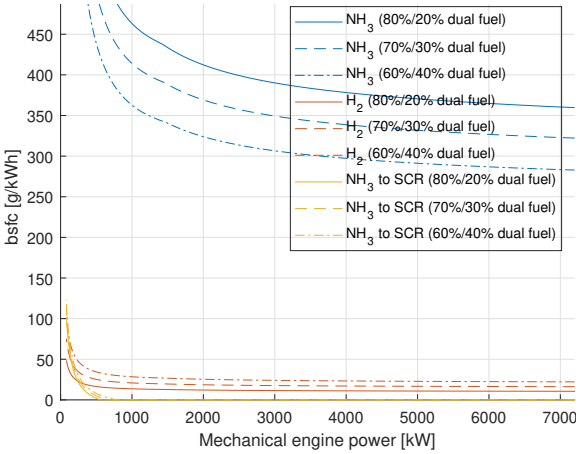

Figure 4.17: Brake specific fuel consumption of the ICE with different 20, 30 and 40 mol% hydrogen.

Maximum in-cylinder pressure and compressor pressure

The maximum in-cylinder pressure of the ICE model increases linearly from 20% to 100% power. It reaches 220 bar at 100% power for both ammonia-hydrogen dual-fuel and methane, which is high [109] but is not necessarily unrealistic due to the fact that the real Wärtsilä 12V31DF is one of the most efficient 4-stroke marine ICEs [114] on the market. The graphs are shown in figures B.3 and B.4 in appendix B. The outlet pressure of the compressor increases approximately linear with the power output above 20% and reaches more than 4 bar for methane (figures B.5 and B.6).

Exhaust gas temperature

The exhaust gas flow consists of the flow that exits and bypasses the turbine. Gas is expanded and thus cooled down in the turbine. Consequently; the exhaust gas temperature (figures 4.18 and 4.19) is higher than the temperature of the gas exiting the turbine. The wastegate is opened further at reduced loads. A larger fraction of the hot exhaust gas bypasses the turbine towards lower loads, which is the reason why the exhaust gas temperature increases strongly from 100% to 20%. The exhaust gas temperature is 100 K higher than the real Wärtsilä engine data in gas mode. Explanations could be that less energy is extracted from the working fluid considering the lower efficiency, or that the model loses less heat than the real Wärtsilä engine.

Air excess, waste-gate control and combustion air mass flow

An air excess set-point of 2.2 has been used as input to the model. Figures 4.20 and 4.21 show that the waste-gate controller is successful in maintaining the air excess setpoints from 100% to approximately 20% power. At least a part of the exhaust gas bypasses the turbine for all loads, so the wastegate never fully closes. This does not sound realistic as it would mean that the full potential of the turbocharger is never used. It is not known what kind of turbocharger control Wärtsilä uses. The waste-gate controller in this study is predominantly a way to maintain a somewhat realistic air excess ratio. The air excess is closely linked to the mass flow of air introduced in the engine.

Figure 4.23 shows that the combustion air inflow of the ICE model follows a trend similar to the data reported by Wärtsilä. The mass flow of air in the ICE model is almost identical to the mass flow of air in the real Wärtsilä 12V31DF, even though NH_3 and H_2 have other stoichiometric air-to-fuel ratios than CH_4.

In-cylinder thermodynamic property calculations

The method used to simulate the in-cylinder process has been explained in section 3.2.1. The 5-point air standard dual cycle is a crude approximation of a real combustion process. Nevertheless, this study does take into account the variation of c_p and c_v with temperature, where other ICE models may use a constant c_p and c_v throughout (part of the) in-cylinder process. This choice added complexity to the model as all temperature-dependent variables have been modelled manually as explained in appendix A.2. For the sake of comparison and validation, the thermodynamic cycle has been calculated (at 100% load and with a 70/30 ammonia-hydrogen blend) in three different ways:

- Assuming constant c_p and c_v (constant-κ).

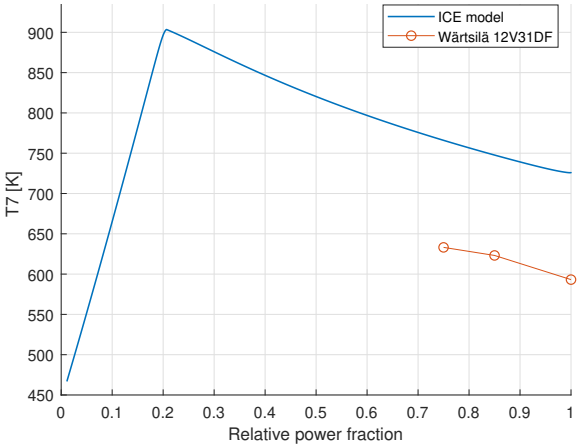

Figure 4.18: Exhaust gas temperature for the ICE engine model with a 70 mol% NH_3 and 30% H2 dual-fuel.

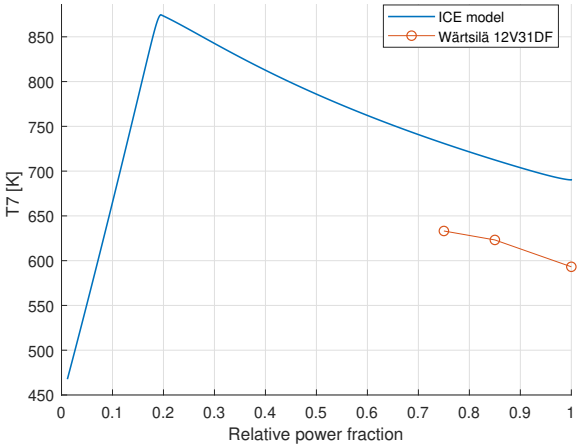

Figure 4.19: Exhaust gas temperature for the ICE engine model with 100% gas (methane) fuel.

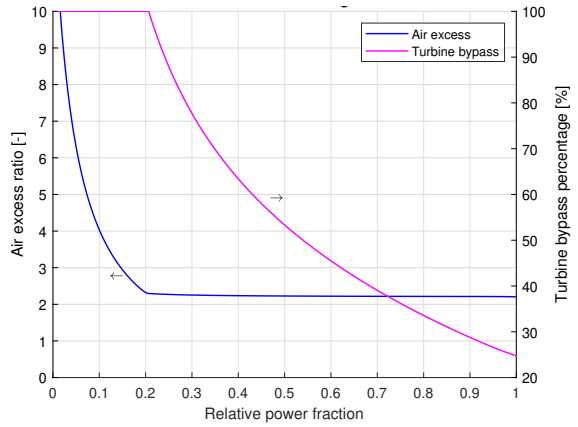

Figure 4.20: Air excess and wastegate control for the ICE model with a 70 mol% NH_3 and 30% H2 dual-fuel.

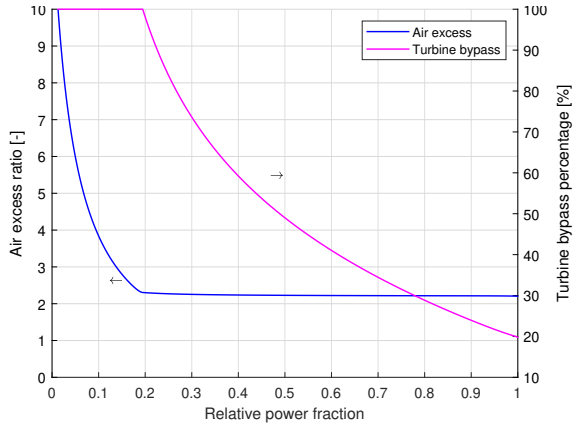

Figure 4.21: Air excess and wastegate control for the ICE engine model with 100% gas (methane) fuel.

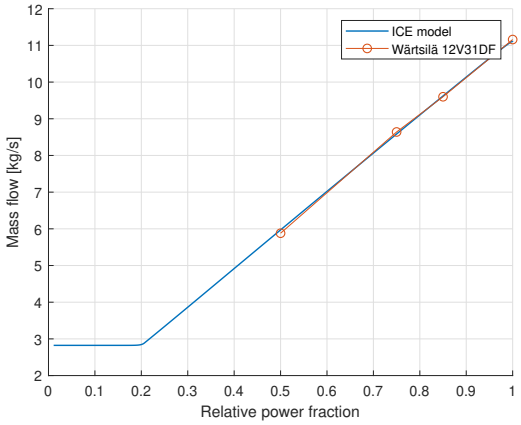

Figure 4.22: Combustion air inlet mass flow for the ICE engine model with a 70 mol% NH_3 and 30% H2 dual-fuel.

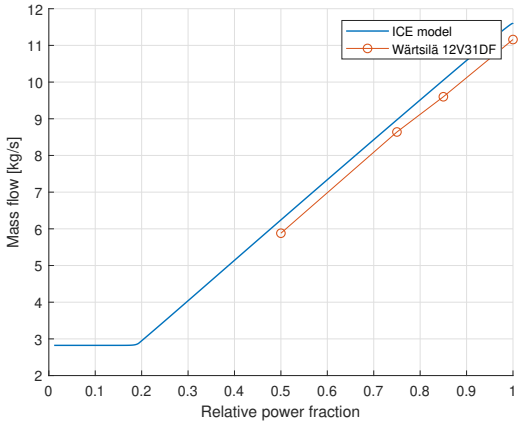

Figure 4.23: Combustion air inlet mass flow for the ICE engine model with 100% gas (methane) fuel.

- Using the thermodynamic property software package REFPROP [72].
- Using variable c_p and c_v, similar to the air-standard ICE model throughout this research.

Notable differences between constant-κ calculations and the ICE model simulations have been observed (): This was expected beforehand, as c_p and c_v have a strong temperature dependency. Tables B.1 to B.4 in appendix B present the results. The similarities between the REFPROP calculations and ICE model simulations indicate that there are likely no large programming errors in the in-cylinder ICE model. Both methods are based on thermodynamic properties from NIST, so they should give similar results throughout dual cycle stages. It is not known what the effect of not using the cold air assumption is on the overall efficiency.

4.2.2. Emissions and after-treatment

The likelihood of NO_x and ammonia emissions based on literature reports have been thoroughly discussed in section 3.2.4. 5% unburned NH_3 (relative to total ammonia consumption in the ICE), 225 ppm NO and 2250 ppm NO_2 have been added artificially to the combustion airflow to provide a qualitative analysis of the after-treatment on the proposed propulsion system.

The emission reduction is summarised in figure 4.24. The specific (g/kWh) NO_x emission increases for decreasing power outputs although the relative amount (ppm) of NO_x is assumed constant troughout the complete load range. This is because the engine becomes less efficient (figure 4.14). Below 20% there is an even steeper rise of specific NO_x emissions because of the sharp increase of air excess (figure 4.20) and the direct link between airflow and absolute NO_x emissions. This has no physical ground, but is the result of assuming a constant NO_x fraction in the air: If the mass of air per kWh mechanical energy increases; the mass of NO_x per kWh increases as well. The emission of NH_3 from the ICE is linked to the $bsfc$ (figure 4.17).

The NO_x reduction in the SCR is straightforward and as expected: A fixed 90% conversion in the SCR has been modelled. It is interesting to see that 2500 ppm NO_x emission from an NH_3 / H_2 engine can be reduced to Tier III levels in the SCR if 90% conversion is indeed feasible. The NO_x amount strongly increases to tier II level in the ASC as unwanted NO is yielded from the reaction of excess ammonia with oxygen.

100% of the slipped ammonia is converted in the ASC model, but highly undesired is the production of N_2O from excess ammonia with oxygen in the ASC. Laughing gas is 300 times more potent as a greenhouse gas compared to CO_2 [101]. The amount formed depends on the slip of ammonia from the SCR and the selectivity of NH_3 to N_2O oxidation; the precise numbers are highly uncertain and have been based on [36]. The current study assumes that 5% of the ammonia not converted in the SCR is converted to laughing gas in the ASC, amounting to 0.6 g/kWh N_2O. One could add less NH_3 to the SCR than necessary for a 1-1 stoichiometry to reduce ammonia slip and N_2O formation but this is not possible when excess ammonia is in the engine exhaust.

The exothermic nature of the reactions involved increases the temperature of the flow across the SCR and the ASC by approximately 50 K. The temperature rise of the exhaust stream does not affect the system performance as the waste heat from this stream is not used. The pressure drop across the after-treatment system has a more pronounced effect on the system performance as the turbocharger can extract less work from expansion. Nevertheless, the turbine bypass curve in the graph of figure 4.20 shows that the potential of the turbocharger is never fully employed in the ICE model. The elimination of the ASC and SCR pressure drop only means that the wastegate opens even further and more exhaust flow bypasses the turbine: The thermal efficiency is not affected.

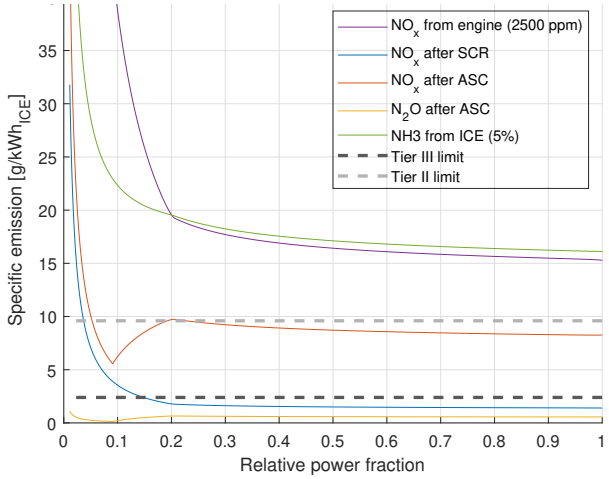

Figure 4.24: Effect of the after-treatment on NO_x (90% NO, 10% NO_2) and N_2O emission in grams per kWh mechanical ICE power with 70 mol% NH_3 and 30% H2 dual-fuel.

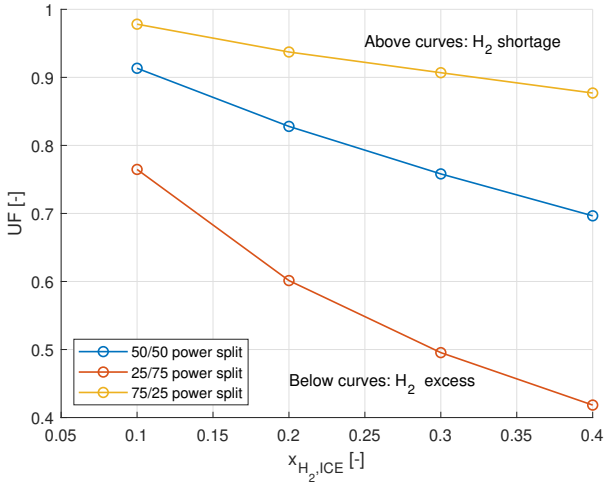

Figure 4.25: SOFC Fuel utilisation required to achieve a specific percentage of hydrogen in the ammonia–hydrogen dual-fuel blend in the ICE ($i = 5000\ \mathrm{A \cdot m^{-2}}$, $T_{SP} = 1073$ K, $ecr = 0.5$).

4.3. Hybrid system

The hybrid system has been simulated in three different configurations; design cases 1, 2 and 3. The number of cells of design cases 1, 2 and 3 have been varied to achieve 50/50, 25/75 en 50/50 SOFC/ICE power split. The ICE always maintains its nominal load and is chosen to be the same engine in all simulations. Different nominal ICE loads would require different engines, while the SOFC is easily scalable by altering the number of cells.

The power output of the SOFC depends on, next to the number of cells, on fuel utilisation, current density, stack temperature and external cracking ratio. Therefore, the SOFC net output power does not always meet the exact goal of the power split. A brief study on the effect of current density has been performed only with the 50/50 power split system.

In all simulations, fuel utilisation is tuned until the hydrogen output in the SOFC off-gas meets the hydrogen demand from the internal combustion engine. Figure 4.25 shows the fuel utilisations corresponding to certain values of $x_{H_2,ICE}$. Above the curves, there is a hydrogen deficit and additional cracking would be necessary to fuel the engine. Below the curves, there would be excess hydrogen. The results of the simulations all correspond to a point on one of the curves in figure 4.25.

Table 4.6: Operating conditions at which the number of cells is determined. The second and third column of the 50/50 power split are used in the current density sensitivity study. ecr = 0.5, T_{stack}=1073 K and $P_{\text{elec,ICE}}$=6840 kW.

Power split →	Design case 1 50/50			Design case 2 25/75	Design case 3 75/25	Unit ↓
i_{stack}	5000	2500	9000	5000	5000	$\text{A}\cdot\text{m}^{-2}$
UF	0.8	0.7	0.8	0.5	0.9	–
V_{cell}	0.773	0.8696	0.655	0.802	0.763	V
N_{cells}	$197{\cdot}10^3$	$335{\cdot}10^3$	$150{\cdot}10^3$	$61{\cdot}10^3$	$602\cdot10^3$	–
$P_{\text{elec,SOFC}}$	6841	6840	6840	2280	20520	kW

4.3.1. Design case 1: 50/50 SOFC/ICE power split

The most obvious configuration of the hybrid system is one where the SOFC and the ICE power are equal. The engine achieves 7200 kW mechanical power at full load, which is converted to 6840 kW electrical power. The number of cells in the SOFC stack has been chosen such that the net electrical power output of the SOFC system matches that of the ICE system. One design point has been chosen to determine the number of cells because the SOFC power depends on current density, temperature, fuel utilisation and external cracking ratio, so a precise 50/50 power split is not achieved, as seen in figure 4.27. This operating point is provided in table 4.6. The SOFC stack temperature setpoint has been kept constant at 1073 K as this results in the most efficient SOFC system, as shown in section 4.1. Only simulations with i = 5000 $\text{A}\cdot\text{m}^{-2}$ are discussed in section 4.3.1. The other current densities are shortly discussed in the last paragraph of section 4.3.1. 5000 $\text{A}\cdot\text{m}^{-2}$ is the current density in the high range of observations in literature. Nine simulations of the hybrid systems have been performed with varying hydrogen blending percentages in the ICE and external cracking ratios in the SOFC. Remember: The ecr is the degree to which the ammonia destined for the SOFC is pre-decomposed in an external decomposition reactor, or "cracker".

- Simulations 1-3: 20% H_2 / 80% NH_3 fuel in the ICE for ecr=0, 0.5 and 1
- Simulations 4-6: 30% H_2 / 70% NH_3 fuel in the ICE for ecr=0, 0.5 and 1
- Simulations 7-9: 40% H_2 / 60% NH_3 fuel in the ICE for ecr=0, 0.5 and 1

Fuel efficiency and the effect of fuel utilisation and external cracking ratio

Figure 4.26 provides the findings highlighting the efficiency of the simulations with 30% hydrogen in the hydrogen–ammonia fuel blend in the ICE. The blue and yellow bars show the estimated LHV electrical efficiency which the component could have achieved as a standalone (SA) system. The orange and purple bars show the LHV electrical efficiency of each component as part of the hybrid system. The green bar shows the electrical LHV efficiency of the hybrid system. ecr, UF and V_{cell} are shown below each simulation. Figure 4.27 presents the separate and combined power outputs.

The efficiency decay from the standalone SOFC to SOFC as part of the hybrid system (figure 4.26) is caused by the extra fuel necessary to heat the external cracker, which becomes more pronounced for higher ecr. For ecr = 0, there is no external cracking necessary, so there is no difference between standalone and hybrid SOFC configuration efficiency. In contrast, the ammonia–hydrogen ICE is more efficient as part of the hybrid system than as a standalone system, as hydrogen blended in the fuel has to be cracked from ammonia before entering the ICE and heating this process would require an additional amount of fuel.

All simulations point out that optimal fuel efficiency is obtained for ecr = 0. The hybrid system efficiency is higher than both the efficiency of the SOFC and the ICE, if 100% of the ammonia that delivers hydrogen atoms the SOFC is cracked inside the stack. The largest efficiency gain is 14 percent points compared to standalone ICE and 8 percent points compared to standalone SOFC in the simulations with 40% hydrogen in the ICE fuel blend. An increase in ecr is followed by an increase in blower power due to the increased cooling demand in the stack and the fuel consumption rises due to the heat requirement in the external cracker. The hybrid system efficiency is always higher than the ICE efficiency under the simulated circumstances. However, the fuel efficiency of the standalone SOFC is sometimes higher for two reasons:

- If the SOFC would act as a standalone SOFC, it can use the chemical energy of the anode off-gas to heat an external cracker, which is not done in the hybrid system as the off-gas is used in the engine.

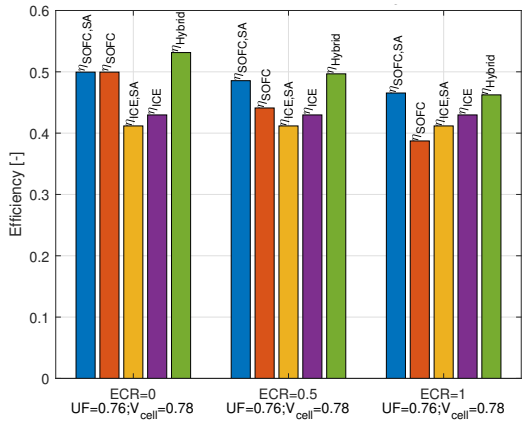

Figure 4.26: Design case 1: Electrical LHV efficiency SOFC and ICE in standalone or hybrid configuration, and the total hybrid system with the ICE operating with 30% hydrogen in the ammonia–hydrogen dual-fuel.

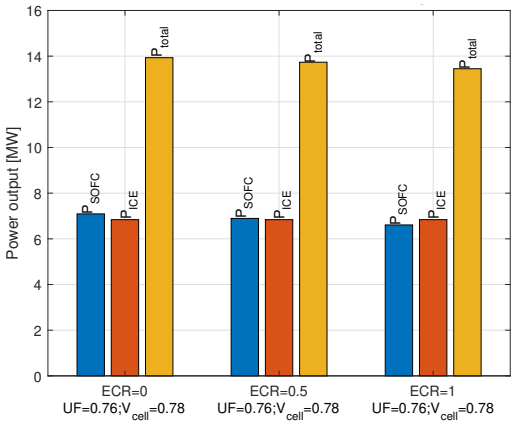

Figure 4.27: Design case 1: Power output of the SOFC, ICE and the total hybrid system with the ICE operating with 30% hydrogen in the ammonia–hydrogen dual-fuel.

Table 4.7: Summary of the performance of hybrid system of design case 1 with 20, 30 and 40% hydrogen in the ICE and ecr=0, 0.5 and 1.

simulation ↓	UF [−]	V_{cell} [V]	η_{hybrid} [−]
$x_{\text{H}_2,\text{ICE}} = 20\%, ecr = 0$	0.83	0.77	0.52
$x_{\text{H}_2,\text{ICE}} = 20\%, ecr = 0.5$	0.83	0.77	0.49
$x_{\text{H}_2,\text{ICE}} = 20\%, ecr = 1$	0.83	0.77	0.46
$x_{\text{H}_2,\text{ICE}} = 30\%, ecr = 0$	0.76	0.78	0.53
$x_{\text{H}_2,\text{ICE}} = 30\%, ecr = 0.5$	0.76	0.78	0.50
$x_{\text{H}_2,\text{ICE}} = 30\%, ecr = 1$	0.76	0.78	0.46
$x_{\text{H}_2,\text{ICE}} = 40\%, ecr = 0$	0.70	0.78	0.54
$x_{\text{H}_2,\text{ICE}} = 40\%, ecr = 0.5$	0.70	0.78	0.50
$x_{\text{H}_2,\text{ICE}} = 40\%, ecr = 1$	0.70	0.78	0.46

- The SOFC can operate at high fuel utilisations if the hydrogen demand from the engine is relatively low (e.g. 20% versus 40%). A high UF results in a high LHV efficiency of the SOFC but requires a very large system in practice.

The results obtained for the nine simulations of the 50/50 power split configuration have been summarised in table 4.10. Fuel utilisation is matched exactly with the hydrogen demand, so no ammonia cracking is necessary to fuel the engine. 70, 76 or 83% fuel utilisation is required to fuel the ICE with exactly 20, 30 or 40% hydrogen in the hydrogen–ammonia blend. The effect of fuel utilisation variation on the hybrid system within the given range efficiency is fairly limited, unlike the effect on the standalone SOFC, because all unused hydrogen leaving the stack in the anode off-gas now generates power in the ICE. Figures B.7, B.8, B.9 and B.10 show results of 20 and 40% ICE hydrogen, similar to figure 4.26 and 4.27.

Heat management

In the context of this research, successful heat management involves:

- The ability to maintain the desired temperature setpoint of the stack by adjusting the cathode airflow under the constraint of a 100 K temperature rise between the in- and outlet of the SOFC stack.
- The ability to pre-heat the cathode and anode stream to the SOFC inlet temperature of choice with a sufficient minimum approach temperature in the counter-current heat exchangers.

The air excess is always higher than the lower limit, 2, indicating that the temperature controller has sufficient flexibility to adapt the cathode airflow until the temperature setpoint T_{SP} is achieved. The desired temperature setpoint T_{SP} is always achieved under the simulated conditions with a 50/50 power split.

The fuel and inlet air to the SOFC have to be pre-heated to the SOFC inlet temperature (1023 K for T_{SP} = 1073) by the gas streams going out of the SOFC. The computed exit temperatures of the cathode and anode off-gas have been monitored to assess the thermodynamic feasibility of the heat exchangers. The

Table 4.8: Heat management results of the simulations of design case 1 with 20, 30 and 40% hydrogen in the ICE and ecr=0, 0.5 and 1.

simulation	λ [-]	T_{stack} [K]	$T_{\text{COG,HEX1,out}}$ [K]	$T_{\text{AOG,HEX2,out}}$ [K]	$Q_{\text{cracker,total}}$ [MW]
$x_{H_2,ICE} = 20\%, ecr = 0$	6	1073	391	663	0
$x_{H_2,ICE} = 20\%, ecr = 0.5$	8.6	1073	404	615	1.34
$x_{H_2,ICE} = 20\%, ecr = 1$	11.3	1073	412	566	2.68
$x_{H_2,ICE} = 30\%, ecr = 0$	5.3	1073	386	656	0
$x_{H_2,ICE} = 30\%, ecr = 0.5$	8.2	1073	402	607	1.46
$x_{H_2,ICE} = 30\%, ecr = 1$	11.1	1073	411	559	2.93
$x_{H_2,ICE} = 40\%, ecr = 0$	4.6	1073	380	650	0
$x_{H_2,ICE} = 40\%, ecr = 0.5$	7.7	1073	400	601	1.59
$x_{H_2,ICE} = 40\%, ecr = 1$	10.9	1073	411	552	3.19

lowest minimum approach temperature in the cathode air heat exchanger (HEX 1) is 76 K. The minimum approach temperature in the fuel heat exchanger (HEX 2) is 100 K. Both are considered more than enough to be feasible in a practical application. Problems in the fuel heat exchanger are unlikely to occur, as the exiting fuel mass flow is higher than the mass flow entering the SOFC.

The extent to which ammonia is cracked inside the SOFC stack has a great impact on heat management. The cathode cooling air demand reduces by a over factor 2 from $\lambda = 11$ to $\lambda = 5$ (at $x_{H_2,ICE} = 30\%$), as ecr changes from 1 to 0, because the endothermic ammonia decomposition reaction absorbs a large portion of the waste heat at $ecr = 0$. The strong cooling capability with $ecr = 0$ did not cause problems in the temperature control of the simulations. Nevertheless, a real system is not 0-D. There is a chance that the stack will not be able to achieve smooth operation in case 100% internal cracking is aimed at: The cooling effect of ammonia decomposition reaction may cause an excessive temperature drop if the electrochemical activity is lacking behind. The current study is not suitable to comment on spatial temperature variations in the stack. Therefore, the $ecr = 0.5$ simulations are valuable as a compromise between effective internal heat management in the stack and system efficiency.

The hydrogen fraction in the ICE dual-fuel has an indirect effect on the cooling air demand. A greater hydrogen fraction requires a lower fuel utilisation in the SOFC stack. The heat capacity of the increased fuel flow then reduces the cooling air demand in the cathode, which is seen in table 4.8 under the air excess λ.

Effect of current density on the system performance

5000 $A \cdot m^{-2}$ has been used rather as a standard current density in the majority of the simulations in this section, to narrow the number of system variations. Nevertheless, i is crucial in the performance in terms of power density, efficiency and heat management of the hybrid system, so it is worthwhile to comment on how sensitive the performance of the hybrid system 50/50 power split system is to a change in current density. Therefore, next to the simulations already performed, the system has been tested for $i = 2500$ $A \cdot m^{-2}$ and $i = 9000$ $A \cdot m^{-2}$ (see table 4.6).

Figure 4.28 points out that increasing current density comes at a cost. Doubling the i from 2500 to 5000 $A \cdot m^{-2}$ lessens the system efficiency by 3 to 4 percent points. A consecutive increase to 9000 $A \cdot m^{-2}$ is even more rigorous with a 6, 7 or 8 percent points efficiency penalty due to the cell voltage decrease and successive blower power increase. However, it must be emphasised that the design point of the system pressure drop has been defined at 5000 $A \cdot m^{-2}$. The effect would have been less pronounced if the system pressure drop design point had been defined at a higher current density. Figure 4.29 displays the cathode air excess increase following a current density increase. The two extremes include:

1. $i = 2500$ $A \cdot m^{-2}$, $ecr = 0 \rightarrow \lambda = 3.0$: The temperature controller in the model functions properly (as $\lambda > 2$ but heat management problems are more likely to arise in a real system, due to a lack of available heat.

2. $i = 9000$ $A \cdot m^{-2}$, $ecr = 1 \rightarrow \lambda = 14.0$: The pressure drop and airflow resulting from the abundance of waste heat is a risk to the system efficiency.

The number of cells required is 335, 197 and 150 thousand for $i = 2500$, and $i = 5000$ and $i = 9000$ $A \cdot m^{-2}$, respectively (table 4.6). Outweighing the power density to the efficiency and heat management is outside the scope of this study.

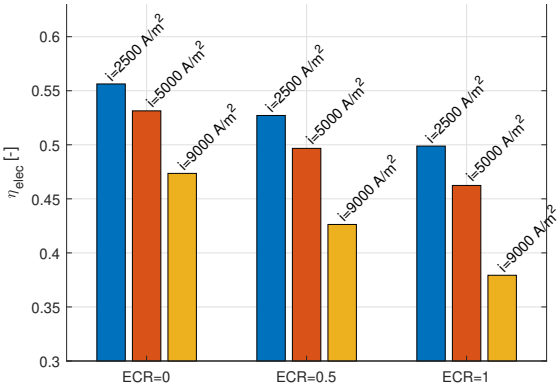

Figure 4.28: Design case 1: Effect of current density on the electric efficiency of the hybrid system in a 50/50 power split configuration with 30% hydrogen in the ICE fuel blend.

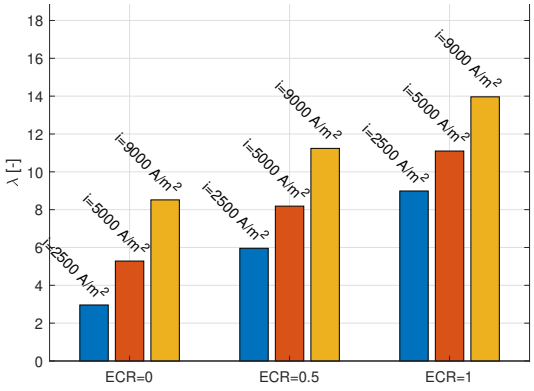

Figure 4.29: Design case 1: Effect of current density on the cathode air excess in a 50/50 power split configuration with 30% hydrogen in the ICE fuel blend.

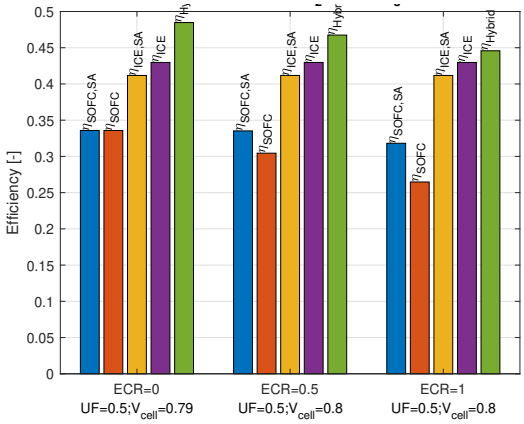

Figure 4.30: Design case 2: Electrical LHV efficiency SOFC and ICE in standalone or hybrid configuration, and the total hybrid system with the ICE operating with 30% hydrogen in the ammonia–hydrogen dual-fuel. The term "η_{hybrid}" is accidentally partly outside the graph in two leftmost bars.

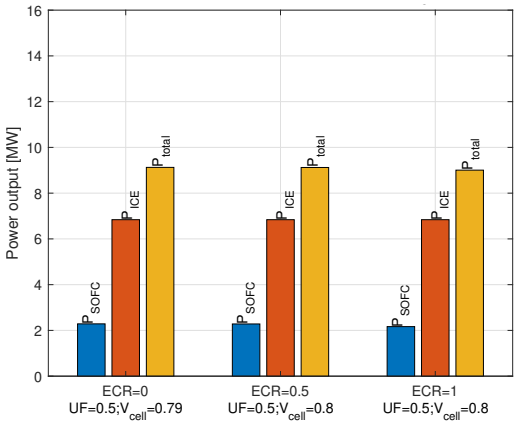

Figure 4.31: Design case 2: Power output of the SOFC, ICE and the total hybrid system with the ICE operating with 30% hydrogen in the ammonia–hydrogen dual-fuel.

4.3.2. Design case 2: 25/75 SOFC/ICE power split

The second system configuration analysed is a 25%/75% SOFC/ICE power split. Here, the SOFC acts primarily as a supplier of hydrogen to the engine. The number of cells has been chosen such that the power output of the SOFC matches one-third of the ICE power output: 2280 kW. The operating point determining N_{cells} has been provided in table 4.6. The fuel utilisation is tuned until the hydrogen output in the SOFC off-gas meets the hydrogen demand from the internal combustion engine as in design case 1. Nine simulations of the hybrid systems have been performed with varying hydrogen blending percentages in the ICE and external cracking ratios in the SOFC, similar to the nine simulations of design case 1.

Fuel efficiency and the effect of fuel utilisation and external cracking ratio

Similar trends as in design case 1 have been observed. For $ecr \neq 0$, the SOFC system in standalone configuration is more efficient than the SOFC in the hybrid system configuration, while for the ICE it is the other way around as seen in figure 4.30. Cracking all ammonia inside the fuel cell ($ecr = 0$) is most beneficial for the hybrid system efficiency. The ICE efficiency dominates in the 25/75 configuration. The hybrid system efficiency achieves 48% for $ecr = 0$ and drops to 45% for $ecr = 1$ at $x_{H_2,ICE} = 30\%$.

The decay is less pronounced than in design case 1 as the impact of the SOFC system efficiency is limited due to the small stack size; ecr primarily affects SOFC operation. The SOFC efficiency appears to be low but is somewhat misleading due to the low fuel utilisation; around half of the hydrogen is delivered to the ICE. The variation of UF following from the variation of $x_{H_2,ICE}$ has a minor effect on the hybrid system efficiency. Figures B.11, B.12, B.11 and B.12 have been compiled in table 4.9. The comments point out that two scenarios are considered unrealistic; this is motivated below.

Table 4.9: Summary of the performance of hybrid system of design case 2 with 20, 30 and 40% hydrogen in the ICE and ecr=0, 0.5 and 1. *: The temperature controller cannot ensure T_{SP} and the cathode off-gas is unable to pre-heat the incoming airflow.

simulation	UF [−]	V_{cell} [V]	η_{hybrid} [−]	comment
$x_{H_2,ICE} = 20\%, ecr = 0$	0.60	0.79	0.48	
$x_{H_2,ICE} = 20\%, ecr = 0.5$	0.60	0.79	0.46	
$x_{H_2,ICE} = 20\%, ecr = 1$	0.60	0.79	0.44	
$x_{H_2,ICE} = 30\%, ecr = 0$	0.50	0.79	0.48	invalid heat management*
$x_{H_2,ICE} = 30\%, ecr = 0.5$	0.50	0.80	0.47	
$x_{H_2,ICE} = 30\%, ecr = 1$	0.50	0.80	0.45	
$x_{H_2,ICE} = 40\%, ecr = 0$	0.42	0.76	0.49	invalid heat management*
$x_{H_2,ICE} = 40\%, ecr = 0.5$	0.42	0.81	0.47	
$x_{H_2,ICE} = 40\%, ecr = 1$	0.42	0.81	0.45	

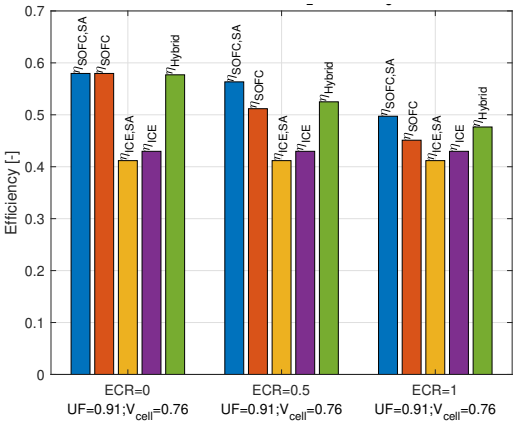

Figure 4.32: Design case 3: Electrical LHV efficiency SOFC and ICE in a standalone or hybrid configuration, and the total hybrid system with the ICE operating with 30% hydrogen in the ammonia–hydrogen dual-fuel.

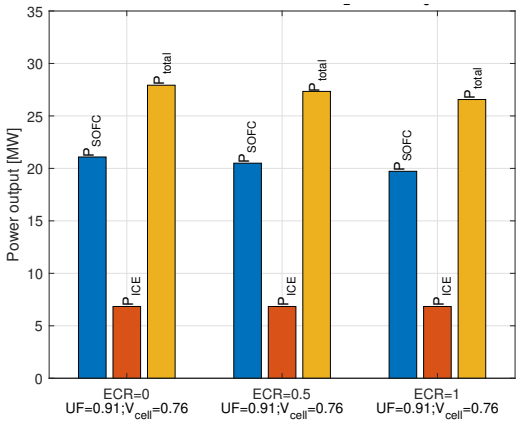

Figure 4.33: Design case 3: Power output of the SOFC, ICE and the total hybrid system with the ICE operating with 30% hydrogen in the ammonia–hydrogen dual-fuel.

Heat management

The temperature controller fails to acquire the temperature setpoint T_{SP} = 1073 K on two occasions in the simulations of design case 2. It fails because the cathode air excess was not allowed to fall below 2. The cathode air excess falls to 2 (table B.5) but is not allowed to attain lower values. There is, subsequently, not enough waste heat available relative to the cooling capacity of the cathode air.

1. $ecr = 0$ and $x_{H_2,ICE} = 30\% \rightarrow T_{stack} = 1066$ K ($< T_{SP}$=1073 K)
2. $ecr = 0$ and $x_{H_2,ICE} = 40\% \rightarrow T_{stack} = 1048$ K ($< T_{SP}$=1073 K)

This has two major consequences:

- Cell voltage is affected by a stack temperature decline. A 0.05 V drop in cell voltage (table 4.9) is caused in the $ecr = 0, x_{H_2,ICE} = 40\%$ simulation due to the increase of ohmic and activation losses in the cells, reducing SOFC efficiency.
- The SOFC cathode off-gas does not contain enough heat to pre-heat incoming airflow. The computed cathode off-gas exit temperature from HEX 2 is too low (table B.5) considering a minimum $\Delta T_{min} >> 0$ in an air heat exchanger. In practice, this would mean that the proposed heat integration should be adapted to sufficiently pre-heat the cathode air.

4.3.3. Design case 3: 75/25 SOFC/ICE power split

Design case 3 involves a power split favouring the SOFC. The ICE is relatively small. A high fuel utilisation (≥ 88%) is required in the SOFC to obtain the desired power split. Table 4.6 lists parameters of the operating point establishing N_{cells}.

Table 4.10: Summary of the performance of hybrid system of design case 3 with 20, 30 and 40% hydrogen in the ICE and ecr=0, 0.5 and 1.

simulation ↓	UF [−]	V_{cell} [V]	η_{hybrid} [−]
$x_{H_2,\text{ICE}} = 20\%, ecr = 0$	0.94	0.76	0.57
$x_{H_2,\text{ICE}} = 20\%, ecr = 0.5$	0.94	0.76	0.52
$x_{H_2,\text{ICE}} = 20\%, ecr = 1$	0.94	0.76	0.47
$x_{H_2,\text{ICE}} = 30\%, ecr = 0$	0.91	0.76	0.58
$x_{H_2,\text{ICE}} = 30\%, ecr = 0.5$	0.91	0.76	0.52
$x_{H_2,\text{ICE}} = 30\%, ecr = 1$	0.91	0.76	0.48
$x_{H_2,\text{ICE}} = 40\%, ecr = 0$	0.88	0.77	0.58
$x_{H_2,\text{ICE}} = 40\%, ecr = 0.5$	0.88	0.77	0.53
$x_{H_2,\text{ICE}} = 40\%, ecr = 1$	0.88	0.77	0.48

Fuel efficiency and the effect of fuel utilisation and external cracking ratio
Based on earlier observations it is straightforward that the SOFC efficiency flourishes in the 75/25 power split: Matching the limited hydrogen demand of the ICE with the hydrogen off-gas requires a high fuel utilisation in the SOFC. The large portion of the system power emerging from the SOFC boosts the hybrid system efficiency to 58% when all ammonia is cracked in the stack. The disadvantage of the large SOFC power relative to the ICE power is that the penalty of 100% external cracking is as high as 10 percent points, compared to 3 percent points in the 25/75 power split. The fuel utilisation in the SOFC and the fraction of hydrogen in the ICE dual-fuel have negligible influence on the hybrid system efficiency in the investigated range of design case 3. Nevertheless, the cell voltage is 0.04 V lower than in the 25/75 power split, which involves a much lower UF.

Heat management
No problems arise in maintaining $T_{\text{SP}} = 1073$ K. The air excess required to cool the stack does not come close to the minimum of 2:

- Minimal air excess observed: $\lambda = 6.4$ at $x_{H_2,\text{ICE}} = 40\%, ecr = 0$
- Maximal air excess observed: $\lambda = 11.6$ at $x_{H_2,\text{ICE}} = 20\%, ecr = 1$

Again it is observed that the degree of internal cracking has an unmistakable effect on the cooling air required: 100% external cracking ($ecr = 1$) requires 1.7 to 1.8 times more cooling air than 100% internal cracking ($ecr = 0$) (table B.6 in appendix B).

The high fuel utilisation involved in the 75/25 simulations leads to a raised cathode air blower power because of two reasons. Firstly, the fuel mass flow (and its total heat capacity) is low compared to when a smaller fraction of the fuel is used (at constant current density), as little excess fuel has to flow through the SOFC. Therefore, the cathode airflow has to account for a larger portion of the total cooling power. Secondly, a high UF leads to more voltage losses (at a constant current density) and the increased production of waste heat requires additional cooling. Details of the heat management are provided in table B.6.

4.3.4. Reduction of nitrogen compounds

It is inevitable to install an after-treatment system to reduce the NO, NO_2 and NH_3 emissions from the ICE, undeterred by the fact that it is hard to accurately estimate the emissions. Based on the observations in this research, it is expected that an SCR system can reduce NO_x emissions to Tier III levels.

The possibility of NO_x emission from the SOFC system has not been considered; fuelling the external cracker in the hybrid system with a H_2/N_2 mixture may result in additional emissions. All anode off-gas is lead to the ICE in the proposed design, so the SOFC will not emit hydrogen or ammonia to the environment.

Excess ammonia coming from the SCR can be converted with an ammonia slip catalyst (ASC) but a high selectivity towards NO could annihilate part of the NO_x reduction in the SCR system. Even more alarming is the risk of N_2O (laughing gas) emission from the ASC. Further research is required for quantitative analysis of the emitted substances and the reduction obtained in an after-treatment system. After-treatment affects the hybrid system in the following ways:

- The SCR and ASC introduce a pressure drop in the system. Nevertheless, this pressure drop is seen as a negligible threat to the system efficiency, considering that the same was concluded for the ICE thermal efficiency too (section 3.2.4).

- Chemical reactions taking place in the SCR and ASC are exothermic, so a temperature rise in the exhaust stream along the after-treatment system shows up. There is no integration of the exhaust waste heat with the rest of the hybrid system, so this has limited consequences for the investigated hybrid system.

- Under the tested circumstances involved in the hybrid system simulations and with the assumption of 2500 ppm NO_x and 5% unburned ammonia in the ICE, the SCR does not require an additional amount of ammonia to allow full NO_x reduction.

- After-treatment adds to the system complexity, reduces system power density and increases system costs.

A high hybrid system efficiency is advantageous as emissions are normally reported in mass per kWh. Moreover, it is foreseen that the SOFC emits limited NO_x compared to the ICE. A large share in propulsion power from the SOFC is favoured in light of this observation, which is only the case if emissions are reported per kWh hybrid system power, rather than per kWh of ICE energy.

4.3.5. Power density

The approximate size of each hybrid system (design case 1, 2 and 3) has been deduced from commercial system dimensions (table B.8), analogues to was done by Reurings [100]. The dimensions of the Bloom Energy Server 5 and the real Wärtsilä 12V31DF generator set are used to investigate and compare the power densities of design cases 1, 2 and 3. The Bloom Energy Server 5, based on a 300 kW module, is used as a reference because the modular methane-fuelled system has already 350 MW installed power in total [1], and because large-scale ammonia-fuelled SOFC systems do not exist yet. The system dimensions (table B.7) have been found in data-sheets[7, 8]. The power density of the SOFC system is solely based on the power output rating provided by the manufacturer.

The volumetric energy density of the commercial SOFC system is five times lower than the ICE: 9 $kW \cdot m^{-3}$ compared to 45 $kW \cdot m^{-3}$, as seen in table 4.11. The gravimetric power density difference, a factor 3, is less pronounced. The power density of the 25/75 power split system attains half (51%) of the power density of the ICE, which is two times more than that of the 75/25 power split system (26%). Design case 3 is three times less energy-dense than the ICE.

Volume scales with the third power of a length scale ($V \sim L^3$), so the 50/50 SOFC/ICE hybrid system would have sides only 43% larger (per kW) than the ICE, despite occupying a three times larger volume, if both systems form a perfect cube. Figure 4.34 shows how the SOFC–ICE inverse volumetric power densities compare if one normalises and projects them on a two-dimensional surface.

Nonetheless, this study only serves as rough guidance to compare the power density of the different design cases and further research should provide a more satisfactory assessment.

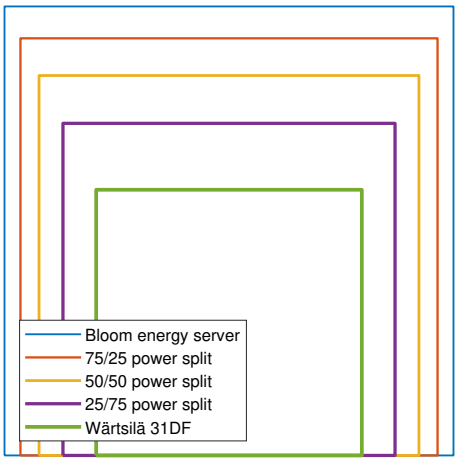

Figure 4.34: Comparison of the system size per unit power output of the hybrid system, the Bloom Energy Server 5 and the Wärtsilä 12V31DF generator set.

Table 4.11: Gravimetric (grav.) and volumetric (vol.) power density (PD) of the proposed systems excluding all power plant equipment. The Wärtsilä 31DF "genset" is a combination of engine and generator.

System or power split →	Bloom Energy Server 5	Wärtsilä 31DF genset	50/50	25/75	75/25
vol. PD [$kW \cdot m^{-3}$]	9	45	15	23	12
grav. PD [$W \cdot kg^{-1}$]	19	60	29	39	23
vol. PD [%]	21	100	34	51	26
grav. PD [%]	32	100	48	65	38

5

Discussion

Societal and scientific relevance of the research
The results of this study provide a characterisation of an ammonia-fuelled SOFC–ICE hybrid system and address some critical challenges related to the use of ammonia. The proposed process can serve as a zero-carbon ship propulsion system and increases efficiency compared to conventional marine engines.

Contrary to the natural gas-fuelled equivalent, this system has not been analysed in literature before (as far as known). A blend of hydrogen from SOFC off-gas and additional ammonia forms a dual-fuel in the ICE, in contrast to many natural gas-based [29, 32, 71, 93] or ammonia-based studies [15, 16, 43, 56, 107, 123] where fuel cell off-gas acts as the only fuel in a downstream gas turbine or internal combustion engine. While the latter is interesting from an efficiency viewpoint, it may lead to an excess space requirement, high capital costs and poor dynamic capabilities. 25%/75%, 50%/50% and 75%/25% SOFC/ICE power splits are obtained, altering the number of SOFC cells in the stack.

Interpretation of the results
Table 5.1 summarises the effects of operational parameters on the SOFC system. Increasing efficiency often reduces cooling demand, which is possible up to the point where a lack of electrochemical waste heat or an excess heat demand from the endothermic decomposition reaction in the stack causes heat management problems.

The SOFC model instantaneously decomposes ammonia upon entering the stack. Pure ammonia, an equivalent hydrogen-nitrogen (3:1) mixture or an ammonia-hydrogen-nitrogen mixture result in an identical cell voltage. Nernst potential and anode concentration losses are unaffected as the partial pressures are alike. Kishimoto et al. [66] computed that, in the case of direct ammonia, most ammonia decomposes within 25% cell length. Moreover, experiments from Kishimoto et al. [64] and Cinti et al. [35] report limited differences between fuels, confirming that immediate decomposition is a valid assumption. Subsequently, this implicates that the degree of external cracking (ecr) does not affect the output voltage of the SOFC if the stack temperature is maintained.

Nevertheless, ecr has a pronounced effect on the system efficiency. The SOFC should crack ammonia up to the point where heat management fails. Internal cracking reduces blower power and the need for burning fuel to heat the external cracker.

The hybrid system simulations provide a first insight into the capabilities of an ammonia-fuelled SOFC–ICE hybrid system. In all 25/75 SOFC/ICE power split simulations ($UF \leq 0.60$), in half of the 50/50 simulations ($0.77 \geq UF \leq 0.83$), and none of the 75/25 SOFC/ICE power split simulations ($UF \geq 0.88\%$), SOFC fuel utilisation is low enough to make it worthwhile (from an efficiency viewpoint) to burn the anode off-gas hydrogen

	Cell voltage	Cooling demand	Power density	SOFC system efficiency
Stack temperature	↑	↓	↑	↑
External cracking ratio	–	↑	–	↓
Fuel utilisation	↓	↑	↓	↑
Current density	↓	↑	↑	↓

Table 5.1: Effects of increments in different operational parameters of an individual fuel cell when the other parameters are kept constant.

with ammonia in the ICE. Then, the hybrid system exhibits better efficiency than a standalone ammonia-fuelled SOFC system (with equal fuel utilisation).

However, one should be careful with comparing hybrid system efficiency to a standalone SOFC system, as a practical SOFC aims to achieve a high fuel utilisation. More important is that the hybrid system outscores the ICE in all simulations. Full internal cracking results in at most 58% (75/25 power split) and 54% (50/50 power split) electrical system efficiency. That is 15 and 11 percent points improvement, as the ICE efficiency (in the hybrid system) is 43%. Full internal cracking caused heat management problems in the 25/75 power split, but 50% external cracking still leads to a 4 percent point increase in system efficiency compared to the engine.

Section 4.3 highlights under what circumstances the hydrogen off-gas from the SOFC matches the hydrogen demand in the ICE. 30 mol% hydrogen in the engine requires 76, 50 or 91% fuel utilisation in the three respective power splits investigated. ICE fuel blends are varied from 20 to 40% hydrogen in an ammonia-hydrogen mixture, so SOFC fuel utilisation is also varied to leave the right amount of hydrogen to the engine. The variation of fuel utilisation at constant current density does not impact system efficiency considerably because all hydrogen off-gas contributes to power production in the ICE. Also, it has a minor effect on cell voltage.

From an efficiency viewpoint, one should aim for a low current density, a low external cracking ratio and a high stack temperature, resulting in a higher stack voltage, reduced external cracker fuel consumption, and reduced blower power. However, the waste heat provided in the electrochemical reactions may be insufficient to maintain the stack temperature setpoint in extreme cases. SOFC fuel utilisation (at constant current density) has no severe impact on the system efficiency because all anode off-gas leaving the stack is used to generate electricity in the internal combustion engine system.

NO_x emissions are reduced in a selective catalytic reduction system without the need for a reducing agent (NH_3 or urea), under the assumption that 5% of the ammonia put in the engine leaves unburned and that the exhaust flow contains 2500 ppm NO_x. The ASC removes excess ammonia but forms NO and the even more undesirable N_2O. The significant uncertainties in ICE emissions and after-treatment conversions require further research. Nevertheless, the hybrid system is favourable over 100% ICE operation because a share of SOFC (expected to form minimal NO_x emissions) power will abate specific emissions (g/kWh).

The volumetric power density of the hybrid system decreases strongly with the SOFC power share. However, at least partly, this effect is counteracted because an increased efficiency reduces the required fuel tank size.

Comparison to relevant literature

Several articles provide valuable insights into methane-fuelled SOFC–ICE integrated systems. However, it was not known in advance whether their methods and results could be extrapolated to the ammonia-fuelled equivalent.

Park et al. [93], Choi et al. [32] and Lee et al. [71] modelled a natural gas-fuelled SOFC–ICE hybrid system showing similarities to this research. A striking difference is that they use ICE exhaust gas [71, 93] or anode off-gas [32] to heat one [71, 93] or two [32] external reformers. In contrast, the proposed system in cracks and burns fuel to heat the external cracker. Therefore, the external cracking ratio (ecr) is critical for efficiency. The exhaust temperature from the turbocharged engine may be too low to crack a considerable fraction of the incoming ammonia. However, the proposed system may be incapable of utilising waste heat optimally.

Next to that, all three studies [32, 71, 93] add no extra fuel to anode off-gas in the ICE, resulting in a small ICE power share. The 75% SOFC–25% ICE simulation with full internal cracking and 40% hydrogen in the ICE dual-fuel is most similar to their power distribution and results in 58% electrochemical hybrid system efficiency, which is close to 59.5% [93] and 59% [32] and 58% [71] found by the stated authors.

Sapra et al. studied SOFC–ICE hybrid systems that add fuel to the ICE, apart from only anode off-gas. They conclude that an increment in the pre-reforming ratio benefits efficiency, while the current study concludes the opposite for the external cracking ratio. In contrast to the external cracker in this research, they integrated the pre-reformer with the stack (using SOFC waste heat directly). They report that a 50/50 SOFC–ICE hybrid system exceeds the efficiency of a conventional marine engine by (at most) 8 percent points.

Strengths and limitations of the research

The section below provides an in-depth discussion of the research methodology.

The SOFC model assumes a uniform temperature along the gas channels, PEN structure and interconnect, similar to the model developed by Kang et al. [61], which greatly simplifies the SOFC model. It eliminates all internal heat transfer equations as introduced by Aguiar et al. [14]. A comparison with the cell behaviour

from Aguiar et al. suggests that this is a valid idea. Averaging temperature and gas concentrations along the stack is especially useful in the system performance analysis; the model is suitable to meet the main goals of this research. However, the temperature profile is unlikely to be perfectly linear, so not all problems with heat management in the stack can be addressed. Kishimoto et al. [65] computed that 75% of ammonia fuelled to a fuel cell is decomposed within approximately 25% of the cell length, which will have a significant impact on the stream-wise temperature profile.

A methane-based study [14] provides SOFC properties in the absence of reliable ammonia SOFC properties, requiring additional validation.

The flow rate-dependent SOFC system pressure drop is extrapolated from 100 millibar at T_{stack} = 1073 K, 100% external cracking and 70% fuel utilisation. The subsequent variable blower power is more realistic than a rigid one, and it shows why internal cracking is beneficial from a cooling point of view. The downside of this approach is that the SOFC system model is sensitive to at which point the pressure drop is quantified.

The largest reported ammonia-fuelled SOFC system is 1 kW, making it difficult to validate the SOFC system model. Different authors also reported a wide diversity of cell performances. Nevertheless, there is no evidence that conventional methane-based SOFC models cannot be altered to an ammonia-fuelled equivalent.

The ICE model is an appropriate model to meet the required level of detail for a system-level approach, although it cannot describe the complex combustion process. The combustion air mass flow and exhaust gas temperature show similarities to the real Wärtsilä 12V31DF, and the computed maximum in-cylinder temperatures and pressures are realistic. The model is more comprehensive than the non-turbocharged four-point engine cycle from Park et al. [93]. On the other hand, it does not require as many experimental input parameters as the six-point Seiliger cycle used by Sapra et al. [103]. Furthermore, it is less complex than the approach of Zheng [124] (MSc thesis) as it excludes combustion modelling. Nonetheless, the dual cycle relies on several input parameters that require experimental validation:

- The five-point thermodynamic engine model incorporates heat loss during compression (5% at full load), combustion (10%) and expansion (8% at full load), but it remains unclear how accurate this is.
- An isochoric (25%) and isobaric part (75%) split combustion. It is unknown what is most realistic in ammonia-hydrogen combustion in an ICE, apart from the expectation that the isobaric phase dominates due to the low fl of ammonia.
- The compression ratio of a Wärtsilä 12V31DF was found in a certification report but details about valve timing are unknown, and the effective compression ratio may have been overestimated.

The air-standard model is unable to describe of the combustion process. The assumption of 5% unburned NH_3 has far-going consequences for engine performance and is on the low side literature reports. There are significant uncertainties related to NO_x and NH_3 emissions from the engine, but this research still provides practical after-treatment insights.

The proposed hybrid system is one way to form an ammonia-fuelled SOFC–ICE hybrid system successfully, but other heat integration configurations were not investigated. It may be possible to facilitate a limited amount of external cracking as well, in addition to pre-heating the air and fuel streams, saving fuel to heat the cracker.

One of the goals of this research was to investigate the possibility of part-load operation of the hybrid system. Sub-models are capable of part-load operation: The SOFC achieves a reduced power output by, for example, reducing current density. The ICE can shift its operating point by providing less fuel to the cylinders. Unfortunately, time constraints objected part-load simulations.

Conclusions have only been drawn based on steady-state results of the models that are, in essence, dynamic. Nevertheless, one of the significant advantages of adding an internal combustion engine to the SOFC is to tackle the weak dynamic behaviour of SOFCs. This research is unsuccessful in supporting this claim with results.

The hybrid system layout (figure 3.14) is a simplification of a practically feasible process system and only consists of the essential components for the system study. For example, it only includes pumps and compressors when they contribute to a significant part of the power requirement. Ammonia enters in gaseous form, while a ship stores it in liquid form; evaporating may require mechanical work, but ambient air is warm enough to supply the heat needed. Start-up and load transients may require hydrogen buffers. The layout only shows two control valves because they provide insight into the model.

6

Conclusion and recommendations

6.1. Conclusion

An ammonia–fuelled solid oxide fuel cell – internal combustion engine hybrid system has been modelled and simulated with three different SOFC stack sizes to achieve a 50/50, 25/75 and 75/25 SOFC/ICE power split. Blowers deliver cathode air and anode fuel to the SOFC stack via heat exchangers. Part of the fuel reaches the SOFC stack via an external cracker, and a part bypasses the cracker to enter as pure ammonia. The heat required for external cracking is supplied by cracking (externally, as well) an additional quantity of ammonia and, subsequently, burning the acquired hydrogen. The anode off-gas from the SOFC contains hydrogen and nitrogen (after the condenser removes the water). It enters the internal combustion engine with ammonia in an 80/20, 70/30 or 60/40 ammonia/hydrogen blend. Low fuel utilisation is needed if the SOFC is large compared to the ICE and vice versa. The SOFC fuel utilisation is tuned so there is neither a hydrogen excess nor a hydrogen shortage for the ICE; the latter would require additional cracking. The turbocharger expands the exhaust flow and compresses the combustion air. Selective catalytic reduction and an ammonia slip catalyst create an after-treatment system that reduces harmful ICE emissions. However, tackling ammonia slip could emit highly unwanted N_2O (laughing gas) and NO_x.

The system model includes the following sub-models:

- The SOFC model incorporates one temperature layer (anode, electrolyte, cathode, interconnect and gas flows), and only inlet, outlet and an averaged temperature are distinguished.
- The decomposition reactor model cracks 0 to 100% of the ammonia going to the SOFC stack.
- Air acts as the working fluid in the ICE model, a five-point thermodynamic cycle, including polytropic compression, isochoric combustion, isobaric combustion and polytropic expansion. The model is based on the geometry and power output of the Wärtsilä 12V31DF.
- Non-isentropic compression models estimate the power required to force air and fuel through the SOFC system.
- Heat balances are solved in two heat exchanger models to assess whether the fuel and air flows to the SOFC stack can be adequately pre-heated.
- Selective catalytic reduction and ammonia slip catalyst models use constant conversions.

Fuel efficiency, heat management and power density quantify the influence of different parameters. Increasing current density (i) benefits power density and provides waste heat to facilitate internal cracking in the SOFC but requires an increased blower power and reduces SOFC and system efficiency. SOFC off-gas hydrogen contributes to power generation in the ICE, so the impact of fuel utilisation (UF) on the system efficiency is minor. The SOFC voltage loss resulting from increased fuel utilisation is moderate. The degree of external (ecr) cracking before the SOFC stack has the utmost influence on system efficiency as extra fuel supplies heat to the endothermic cracking reaction in the external cracker. Moreover, it requires more stack cooling power. The efficiency of the 75/25 SOFC/ICE power split configuration with full internal cracking

(58%) is 17 percent points higher than the standalone ICE ($\eta_{ICE,SA}$=41%). However, the volume per unit power output, based on commercial ICE and SOFC systems, is double as high as the 25/75 configuration.

The electrochemical oxidation of hydrogen supplies heat to the internal cracking reaction of ammonia in the SOFC. An increased system efficiency, caused by a high SOFC voltage and low blower power, is accompanied by a net reduction of waste heat from the SOFC. The hybrid system efficiency can be improved until the cathode airflow reaches its lower limit, stack temperature cannot be maintained, and sufficiently preheating air and fuel streams is impossible. These problems arose in a few instances where internal cracking obtained 100% of the hydrogen for the SOFC. Follow-up research should further quantify heat management problems inside the SOFC.

In general, the SOFC–ICE hybrid system includes some powerful advantages compared to a standalone SOFC or ICE system. The SOFC saves fuel costs as it is considerably more efficient in converting ammonia to power than the ICE. The low SOFC power density will be compensated in some measure, as the high efficiency limits the minimum on-board fuel tank size. The highly endothermic decomposition reaction of ammonia to hydrogen and nitrogen requires high-temperature heat, which the electrochemical reactions in the SOFC should supply. Moreover, it is expected that the SOFC emits little NO_x compared to the ICE so that it will decrease the NO_x emissions per unit of electrical energy. Adding an ICE to the SOFC is advantageous as 100% oxidation cannot be obtained in the SOFC: The hydrogen off-gas counteracts the weak combustion characteristics of ammonia and contributes to power generation.

6.2. Recommendations

Directions considered for follow-up research are listed below.

- More research is needed to predict the power output and the emissions of NO_x, unburned NH_3 and possibly even N_2O or H_2 of ammonia-hydrogen-fuelled marine engines. While writing this, T. Boxma completed his MSc thesis [26] on this topic. Combustion modelling, experiments or cooperation with an engine manufacturer, as MAN is planning to build a megawatt-scale ammonia engine[79], could be part of a future study.

- 1- or multi-dimensional modelling of the SOFC is necessary to thoroughly analyse the interplay between electrochemistry and the endothermic ammonia decomposition reaction inside the stack. However, the 0-D model used cannot unveil all challenges with heat management, especially in the case of a high degree of internal cracking. Furthermore, this research neglects electrochemical behaviour changes along the stack's stream direction, but the continuous shift in gas concentrations and temperature affects losses throughout the cell.

- Anode off-gas is roughly 300 to 400°C when it enters the water-cooled condenser, and the model releases engine exhaust gas at over 400°C. This waste heat may be used more effectively. One may also think of a different way to heat the external cracker, for instance, by burning (excess) off-gas hydrogen or pure ammonia. Electric heating could be an option if heating by combustion results in too high emissions but is ill-favoured from an energy and exergy efficiency point of view. Furthermore, ammonia is cracked inside the fuel channel or outside the stack in a separate reactor in this research. Indirect internal cracking would involve the integration of a different cracking channel with the anode channel, which might act as a practical compromise between internal and external cracking.

- Effort was put in developing an air standard internal combustion engine model that includes a variable ratio of specific heats $\kappa = \frac{c_p}{c_p} = f(T)$. It should be assessed whether this level of detail is justified in a system analysis compared to a more conventional model where $\kappa = \frac{c_p}{c_p} =$ constant. On the other hand, the model may be too simplistic. The mass balance is inaccurate by definition because the ICE model neglects the air exchange process, and only air acts as the working fluid. Adding complexity to the engine model may do more justice to the combustion processes in a real engine.

- Kinetic reaction models of the ammonia decomposition, selective catalytic reduction, and ammonia slip catalyst reactors could replace the constant conversion models in this research.

- Data about electrochemical properties such as conductivity, activation energy of diffusivity of components of an ammonia-fuelled stack could be collected in future research, as the current study made use of properties of a methane-fuelled SOFC. In addition, experiments should validate the SOFC model.

- The power consumption of the air and fuel blowers is an essential factor in the system efficiency, which largely depends on the system pressure drop. Therefore, future work should determine the system pressure drop more carefully.
- Part load behaviour has not been studied yet and should have a vital role in further research to show the potential of an ammonia-fuelled SOFC–ICE hybrid system for ships. Besides, an improved ability to operate dynamically is one of the reasons why integrating an SOFC with a less efficient ICE is interesting; so, future research should involve dynamic operation and the accompanying control strategies. For example, temporary hydrogen storage could be part of dynamic operation.
- More dedicated flow-sheeting software than Matlab & Simulink such as Aspen Plus or Cycle Tempo could ease the process of modelling thermodynamic processes and enhance the system analysis through, for example, an exergy analysis.

A

Appendix: Methodology

A.1. Heat exchanger models

The flow of the cold stream through the anode heat exchanger (HEX1) is the sum of ammonia required for the SOFC and the ammonia required for the burner fuel and the hot stream the anode off-gas stream.

$$\dot{N}_{\text{HEX1,cold}} = \dot{N}_{\text{NH}_3,\text{SOFC}} + \dot{N}_{\text{NH}_3,\text{burner}} \tag{A.1}$$

$$\dot{N}_{\text{HEX1,hot}} = \dot{N}^{\text{out}}_{\text{an,H}_2} + \dot{N}^{\text{out}}_{\text{an,H}_2\text{O}} + \dot{N}^{\text{out}}_{\text{an,NH}_3} + \dot{N}^{\text{out}}_{\text{an,N}_2} \tag{A.2}$$

The inlet temperatures of the hot and cold stream are the SOFC and the fuel blower outlet temperature, respectively. The outlet temperature of the fuel is the inlet that is required for the SOFC.

$$T^{\text{in}}_{\text{HEX1,hot}} = T^{\text{out}}_{\text{SOFC}} \tag{A.3}$$

$$T^{\text{in}}_{\text{HEX1,cold}} = T^{\text{out}}_{\text{fuelblower}} \tag{A.4}$$

$$T^{\text{out}}_{\text{HEX1,cold}} = T^{\text{in}}_{\text{SOFC}} = T_{\text{stack}} - \frac{\Delta T_{\text{stack}}}{2} \tag{A.5}$$

The duty of the heat exchanger is:

$$\dot{Q}_{\text{HEX1}} = \sum_{i=1}^{4} \dot{N}_{i,\text{HEX1,cold}} (h^{\text{out}}_i - h^{\text{in}}_i) \qquad i \in \{\text{H}_2, \text{NH}_3, \text{N}_2, \text{H}_2\text{O}\} \tag{A.6}$$

Where h^{in}_i and h^{out}_i are functions of $T^{\text{in}}_{\text{HEX1,cold}}$ and $T^{\text{out}}_{\text{HEX1,cold}}$ in NIST polynomials (appendix A.2). Heat loss in the heat exchanger is neglected. Modified Newton-Raphson is then used to solve equation A.7 for $T^{\text{out}}_{\text{HEX1,hot}}$; the outlet temperature of the hot stream.

$$0 = \sum_{i=1}^{4} \dot{N}_{i,\text{HEX1,hot}} (h^{\text{in}}_i - h^{\text{out}}_i) + \dot{Q}_{\text{HEX1}} \qquad i \in \{\text{N}_2, \text{O}_2\} \tag{A.7}$$

The cold stream through the cathode heat exchanger (HEX2) is the air that flows to the cathode. The hot stream is simply the cathode off-gas stream.

$$\dot{N}_{\text{HEX2,cold}} = \dot{N}_{\text{N}_2,\text{SOFC}} + \dot{N}_{\text{O}_2,\text{SOFC}} \tag{A.8}$$

$$\dot{N}_{\text{HEX2,hot}} = \dot{N}^{\text{out}}_{\text{ca,N}_2} + \dot{N}^{\text{out}}_{\text{ca,O}_2} \tag{A.9}$$

The inlet temperatures of the hot and cold stream are the SOFC and the fuel blower outlet temperature, respectively. The outlet temperature of the fuel is the inlet that is required for the SOFC.

$$T^{\text{in}}_{\text{HEX2,hot}} = T^{\text{out}}_{\text{SOFC}} \tag{A.10}$$

$$T^{\text{in}}_{\text{HEX2,cold}} = T^{\text{out}}_{\text{airblower}} \tag{A.11}$$

$$T^{\text{out}}_{\text{HEX2,cold}} = T^{\text{in}}_{\text{SOFC}} = T_{\text{stack}} - \frac{\Delta T_{\text{stack}}}{2} \tag{A.12}$$

The duty of the heat exchanger is:

$$\dot{Q}_{\text{HEX2}} = \sum_{i=1}^{4} \dot{N}_{i,\text{HEX2,cold}}(h_i^{\text{out}} - h_i^{\text{in}}) \qquad i \in \{H_2, NH_3, N_2, H_2O\} \tag{A.13}$$

Where h_i^{in} and h_i^{out} are functions of $T^{\text{in}}_{\text{HEX2,cold}}$ and $T^{\text{out}}_{\text{HEX2,cold}}$ (appendix A.2). Heat loss in the heat exchanger is neglected. Modified Newton-Raphson is then used to solve equation A.14 for $T^{\text{out}}_{\text{HEX1,hot}}$; the outlet temperature of the hot stream.

$$0 = \sum_{i=1}^{4} \dot{N}_{i,\text{HEX1,hot}}(h_i^{\text{in}} - h_i^{\text{out}}) + \dot{Q}_{\text{HEX1}} \qquad i \in \{H_2, NH_3, N_2, H_2O\} \tag{A.14}$$

A.2. Thermodynamic properties from NIST

The equations below, obtained from the NIST Chemistry WebBook [4], are manually coded in a large number of MATLAB & Simulink models to approximate thermodynamic properties. All molecules have different A, B, C, D, E, F, G and H coefficients and some coefficients are only valid in a specific temperature range. Programming this is time-consuming but the result is a fast and accurate computation of enthalpy, entropy or specific heat capacity of gases that are considered to be ideal. The alternative considered first was to let MATLAB interact with REFPROP [72] but that slows down simulations. Listing over 100 coefficients is avoided; please refer to the NIST Chemistry WebBook [4] for the A-H coefficients of the molecules in table A.1.

$$t = \frac{T}{1000} \tag{A.15}$$

$$c_{\text{p}} = A + B \cdot t + C \cdot t^2 + D \cdot t^3 + E \cdot t^{-2} \tag{A.16}$$

$$h^0 - h^0_{298.15} = h = A \cdot t + B \cdot \frac{t^2}{2} + C \cdot \frac{t^3}{3} + D \cdot \frac{t^4}{4} - E \cdot t^{-1} + F - H \tag{A.17}$$

$$s^0 - s^0_{298.15} = s = A \cdot \ln t + B \cdot t + C \cdot \frac{t^2}{2} + D \cdot \frac{t^3}{3} - E \cdot \frac{t^{-2}}{2} + G \tag{A.18}$$

Table A.1: Thermodynamic properties used in the sub-models.

	NIST [4] properties used
Several SOFC system sub-models	NH_3, H_2, N_2, O_2, H_2O
Air-standard dual cycle in the ICE model	N_2, O_2, Ar
After-treatment sub-models	NH_3, H_2, N_2, O_2, H_2O, NO, NO_2, N_2O

A.3. Compressibiliy factors from REFPROP

The table below has been generated based on data from the thermodynamic property software package REFPROP [72].

Table A.2: Compressibility factor of air for different temperatures and pressures adopted from REFPROP [72].

	Pressure [bar]														
Temperature [K]	1.00	5.00	10.0	20.0	40.0	60.0	80.0	100	150	200	250	300	400	500	600
75	0.005	0.026	0.052	0.103	0.206	0.307	0.408	0.508	0.754	0.997	1.236	1.472	1.935	2.389	2.834
80	0.582	0.025	0.050	0.099	0.198	0.295	0.391	0.487	0.722	0.953	1.181	1.405	1.844	2.274	2.696
90	0.972	0.023	0.047	0.093	0.185	0.276	0.365	0.454	0.671	0.883	1.092	1.296	1.696	2.086	2.468
100	0.979	0.888	0.045	0.090	0.177	0.263	0.348	0.431	0.634	0.831	1.024	1.213	1.582	1.940	2.289
120	0.988	0.938	0.867	0.677	0.177	0.257	0.335	0.410	0.592	0.767	0.936	1.101	1.420	1.729	2.029
140	0.992	0.962	0.921	0.831	0.588	0.331	0.373	0.433	0.590	0.743	0.892	1.038	1.319	1.590	1.853
160	0.995	0.975	0.949	0.896	0.781	0.661	0.571	0.549	0.633	0.756	0.883	1.009	1.257	1.497	1.730
180	0.997	0.983	0.966	0.932	0.863	0.798	0.744	0.709	0.718	0.798	0.899	1.006	1.221	1.434	1.643
200	0.998	0.988	0.977	0.954	0.910	0.870	0.838	0.814	0.807	0.855	0.931	1.018	1.204	1.393	1.579
250	0.999	0.995	0.991	0.983	0.968	0.956	0.947	0.942	0.946	0.972	1.016	1.071	1.200	1.340	1.483
300	1.000	0.999	0.997	0.995	0.992	0.991	0.991	0.993	1.008	1.033	1.068	1.110	1.208	1.317	1.431
350	1.000	1.000	1.001	1.001	1.004	1.007	1.012	1.018	1.037	1.063	1.095	1.131	1.212	1.302	1.397
400	1.000	1.001	1.002	1.005	1.010	1.016	1.023	1.030	1.052	1.078	1.107	1.140	1.211	1.289	1.371
450	1.000	1.002	1.003	1.006	1.013	1.020	1.028	1.036	1.059	1.085	1.113	1.143	1.207	1.276	1.348
500	1.000	1.002	1.004	1.007	1.015	1.023	1.031	1.040	1.063	1.087	1.114	1.142	1.201	1.264	1.328
600	1.000	1.002	1.004	1.008	1.016	1.024	1.032	1.041	1.063	1.086	1.110	1.135	1.186	1.240	1.294
800	1.000	1.002	1.004	1.007	1.015	1.022	1.030	1.038	1.057	1.077	1.097	1.117	1.158	1.200	1.242
1000	1.000	1.002	1.003	1.007	1.013	1.020	1.026	1.033	1.050	1.066	1.083	1.100	1.135	1.169	1.204
1200	1.000	1.001	1.003	1.006	1.011	1.017	1.023	1.029	1.043	1.058	1.073	1.087	1.117	1.146	1.176
1400	1.000	1.001	1.003	1.005	1.010	1.015	1.020	1.025	1.038	1.051	1.064	1.077	1.102	1.128	1.154
1600	1.000	1.001	1.002	1.005	1.009	1.014	1.018	1.023	1.034	1.045	1.057	1.068	1.091	1.114	1.136
1800	1.000	1.001	1.002	1.004	1.008	1.012	1.016	1.020	1.031	1.041	1.051	1.061	1.082	1.102	1.122
2000	1.000	1.001	1.002	1.004	1.007	1.011	1.015	1.018	1.028	1.037	1.046	1.055	1.074	1.092	1.111
2200	1.000	1.001	1.002	1.003	1.007	1.010	1.013	1.017	1.025	1.034	1.042	1.051	1.067	1.084	1.101
2400	1.000	1.001	1.002	1.003	1.006	1.009	1.012	1.015	1.023	1.031	1.039	1.046	1.062	1.077	1.093
2600	1.000	1.001	1.001	1.003	1.006	1.009	1.011	1.014	1.021	1.029	1.036	1.043	1.057	1.071	1.085

B

Appendix: Results

B.1. Internal combustion engine model results

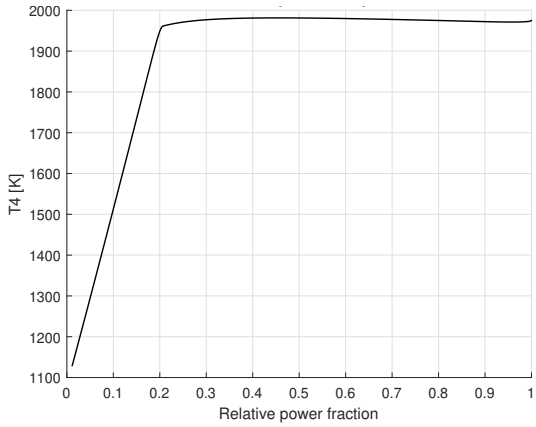

Figure B.1: Maximum in-cylinder temperature for the ICE engine model with a 70 mol% NH_3 and 30% H2 dual fuel.

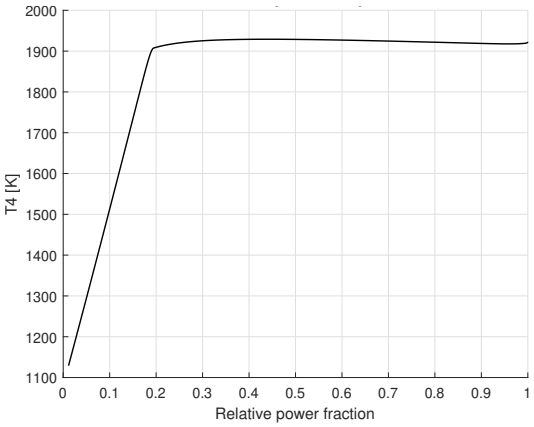

Figure B.2: Maximum in-cylinder temperature for the ICE engine model with 100% gas (methane) fuel.

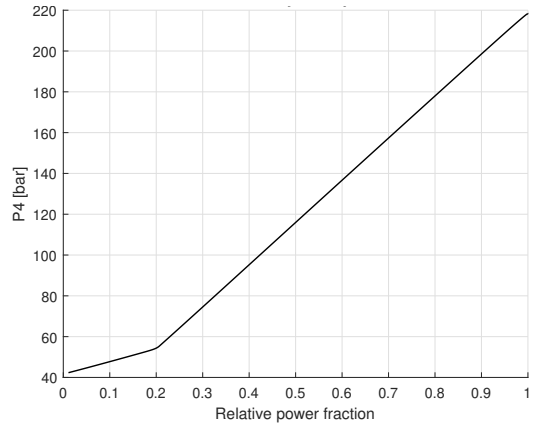

Figure B.3: Maximum in-cylinder pressure for the ICE engine model with a 70 mol% NH_3 and 30% H2 dual fuel.

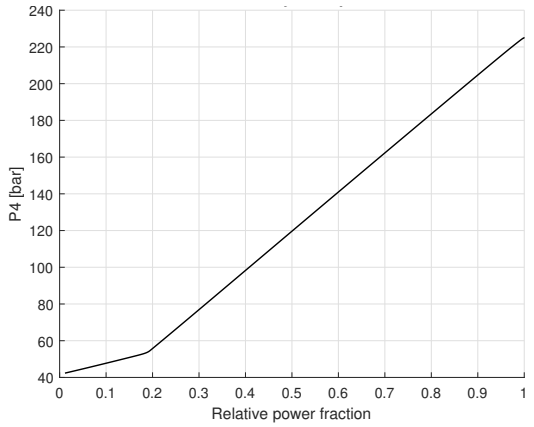

Figure B.4: Maximum in-cylinder pressure for the ICE engine model with 100% gas (methane) fuel.

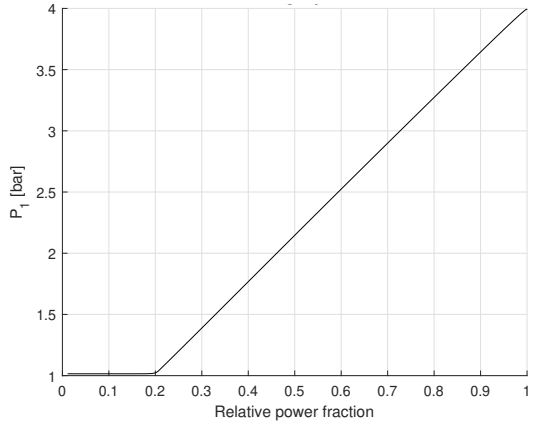

Figure B.5: Compressor outlet pressure for the ICE engine model with a 70 mol% NH_3 and 30% H2 dual fuel.

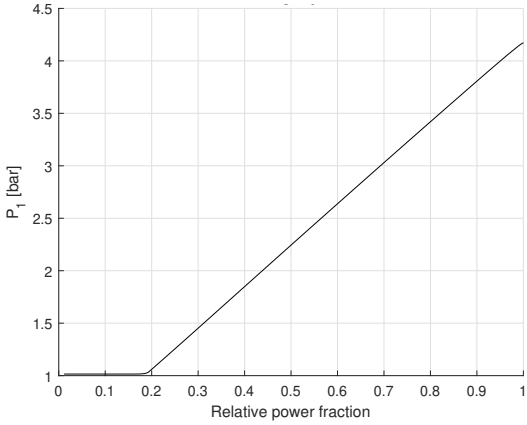

Figure B.6: Compressor outlet pressure for the ICE engine model with 100% gas (methane) fuel.

Table B.1: Polytropic compression process with ($PV^{n_{\text{exp,c}}}$)=constant and $n_{\text{exp,c}}$=1.383. All three methods use the same inlet condition (1).

Point in dual cycle →	1	2: ICE model ($\kappa \neq$ constant)	2: $\kappa = 1.4$	2: REFPROP [72]
T [K]	328.0	857.5	901.7	856.0
P [bar]	3.7	144.5	144.5	144.2
V	0.0350	0.0025	0.0025	0.0025
$\Delta u_{1\to2}$ [kJ·kg^{-1}]	-	406.8	412.1	398.6
$\Delta w_{1\to2}$ [kJ·kg^{-1}]	-	-430.2	-430.4	-429.6
$\Delta q_{1\to2}$ [kJ·kg^{-1}]	-	-23.4	-18.3	-31.0

Table B.2: Isochoric combustion process. All three methods use the same inlet condition (2).

Point in dual cycle →	2	3: ICE model ($\kappa \neq$ constant)	3: $\kappa = 1.4$	3: REFPROP [72]
T [K]	857.5	1242.2	1320.7	1241.7
P [bar]	144.5	209.3	222.6	210.6
V	0.0025	0.0025	0.0025	0.0025
$\Delta u_{2\to3}$ [kJ·kg^{-1}]	-	0.0	0.0	0.0
$\Delta w_{2\to3}$ [kJ·kg^{-1}]	-	0.0	0.0	0.0
$\Delta q_{2\to3}$ [kJ·kg^{-1}]	-	332.7	332.7	332.7

Table B.3: Isobaric combustion process. All three methods use the same inlet condition (3).

Point in dual cycle →	3	4: ICE model ($\kappa \neq$ constant)	4: $\kappa = 1.4$	4: REFPROP [72]
T [K]	1242.2	2055.4	2234.9	2054.9
P [bar]	209.3	209.3	209.3	210.6
V	0.0025	0.0040	0.0045	0.0041
$\Delta u_{3\to4}$ [kJ·kg^{-1}]		763.4	713.0	761.5
$\Delta w_{3\to4}$ [kJ·kg^{-1}]		234.8	285.2	236.7
$\Delta q_{3\to4}$ [kJ·kg^{-1}]		998.2	998.2	998.2

Table B.4: Polytropic expansion process with $(PV^{n_{\text{exp,e}}})$=constant $n_{\text{exp,e}}$=1.360. All three methods use the same inlet condition (4).

Point in dual cycle →	4	5: ICE model ($\kappa \neq$ constant)	5: $\kappa = 1.35$	5: REFPROP [72]
T [K]	2055.4	977.5	945.4	977.4
P [bar]	209.3	11.1	11.1	11.1
V	0.00405	0.03500	0.03500	0.03500
$\Delta u_{4\to5}$ [kJ·kg^{-1}]	-	-995.6	-903.4	-991.2
$\Delta w_{4\to5}$ [kJ·kg^{-1}]	-	919.3	885.9	918.6
$\Delta q_{4\to5}$ [kJ·kg^{-1}]	-	-76.4	-17.6	-72.6

B.2. Hybrid system model results

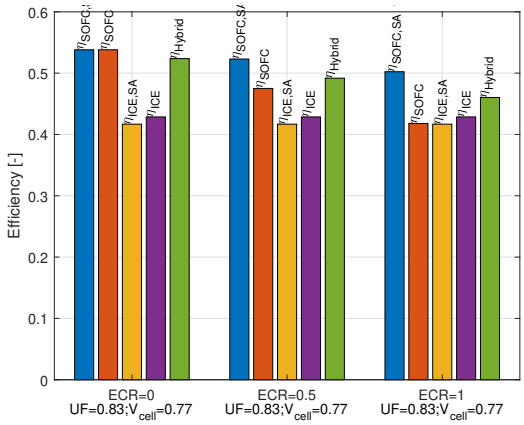

Figure B.7: Design case 1: Electrical efficiency SOFC and ICE in standalone or hybrid configuration, an the total hybrid system with the ICE operating with 20% hydrogen in the ammonia–hydrogen dual fuel.

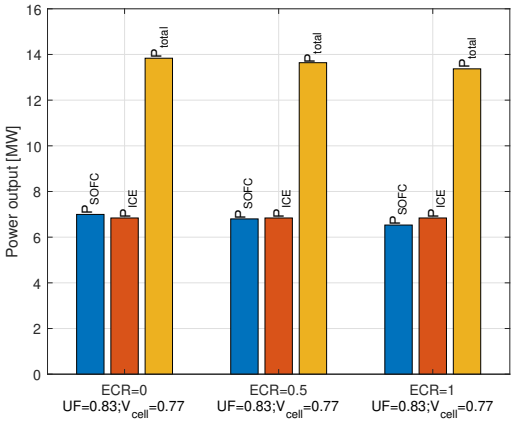

Figure B.8: Design case 1: Power output of the SOFC, ICE and the total hybrid system with the ICE operating with 20% hydrogen in the ammonia–hydrogen dual fuel.

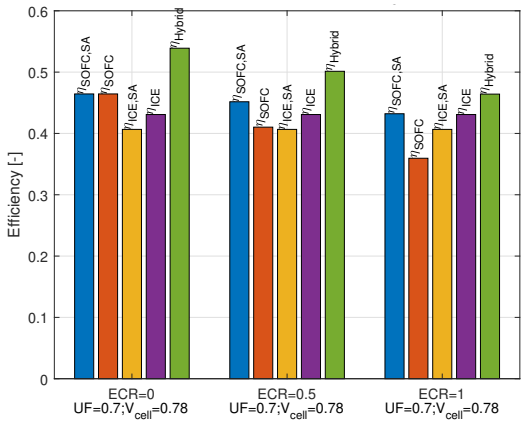

Figure B.9: Design case 1: Electrical efficiency SOFC and ICE in standalone or hybrid configuration, an the total hybrid system with the ICE operating with 40% hydrogen in the ammonia–hydrogen dual fuel.

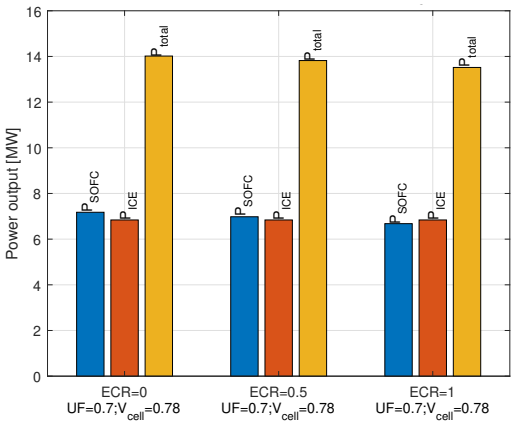

Figure B.10: Design case 1: Power output of the SOFC, ICE and the total hybrid system with the ICE operating with 40% hydrogen in the ammonia–hydrogen dual fuel.

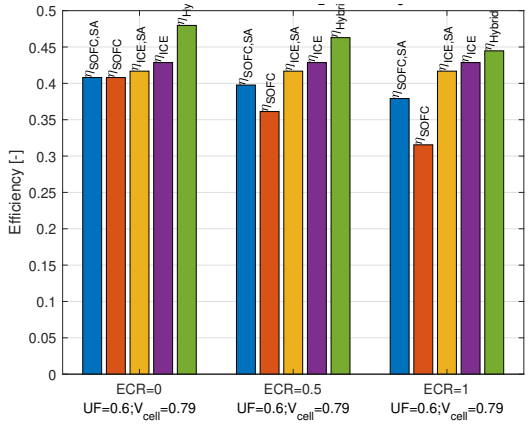

Figure B.11: Design case 2: Electrical efficiency SOFC and ICE in standalone or hybrid configuration, an the total hybrid system with the ICE operating with 20% hydrogen in the ammonia–hydrogen dual fuel.

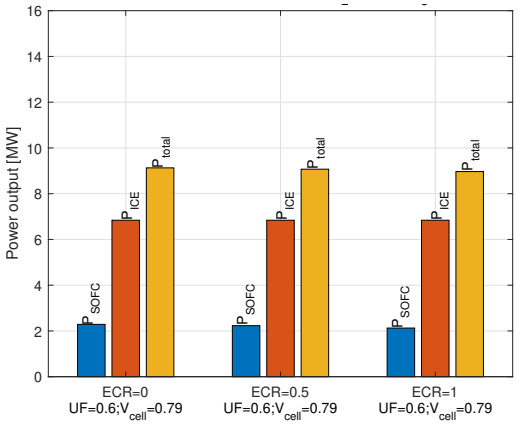

Figure B.12: Design case 2: Power output of the SOFC, ICE and the total hybrid system with the ICE operating with 20% hydrogen in the ammonia–hydrogen dual fuel.

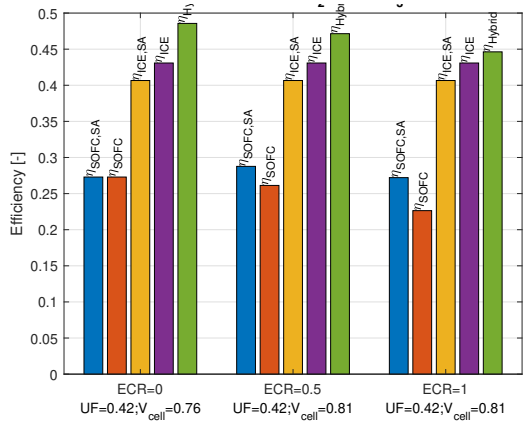

Figure B.13: Design case 2: Electrical efficiency SOFC and ICE in standalone or hybrid configuration, an the total hybrid system with the ICE operating with 40% hydrogen in the ammonia–hydrogen dual fuel.

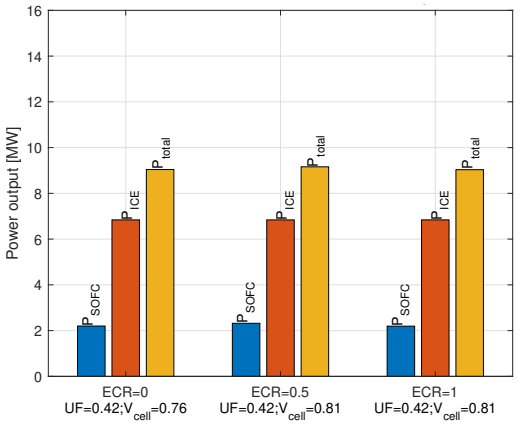

Figure B.14: Design case 2: Power output of the SOFC, ICE and the total hybrid system with the ICE operating with 40% hydrogen in the ammonia–hydrogen dual fuel.

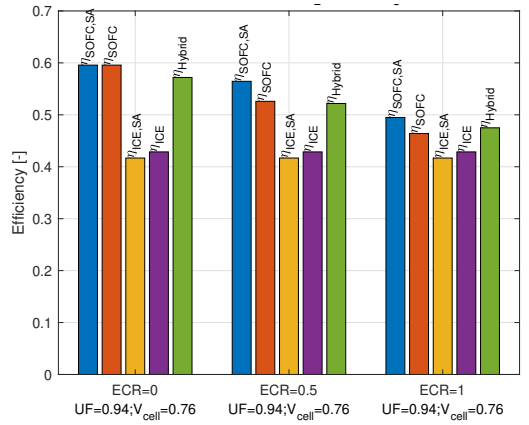

Figure B.15: Design case 3: Electrical efficiency SOFC and ICE in standalone or hybrid configuration, an the total hybrid system with the ICE operating with 20% hydrogen in the ammonia–hydrogen dual fuel.

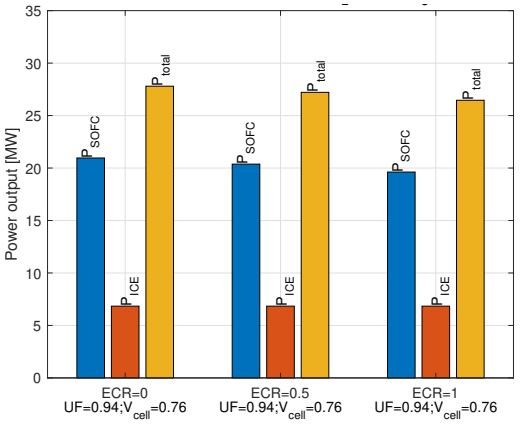

Figure B.16: Design case 3: Power output of the SOFC, ICE and the total hybrid system with the ICE operating with 20% hydrogen in the ammonia–hydrogen dual fuel.

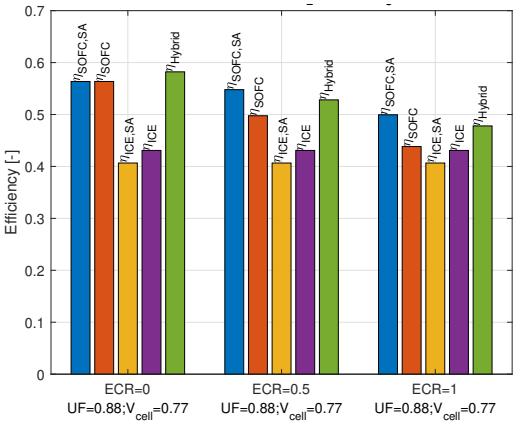

Figure B.17: Design case 3: Electrical efficiency SOFC and ICE in standalone or hybrid configuration, an the total hybrid system with the ICE operating with 40% hydrogen in the ammonia–hydrogen dual fuel.

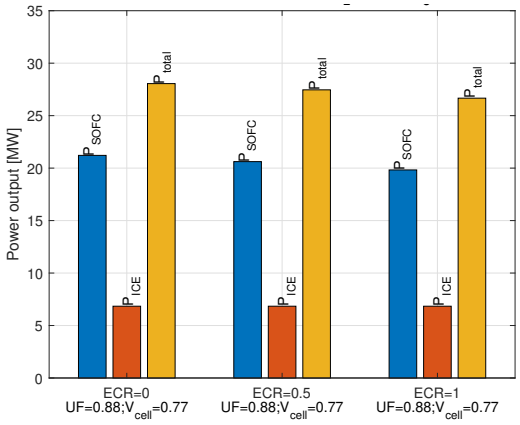

Figure B.18: Design case 3: Power output of the SOFC, ICE and the total hybrid system with the ICE operating with 40% hydrogen in the ammonia–hydrogen dual fuel.

Table B.5: Heat management results of the simulations of design case 2 with 20, 30 and 40% hydrogen in the ICE and ecr=0, 0.5 and 1.

simulation ↓	λ [-]	T_{stack} [K]	$T_{\text{COG,HEX1,out}}$ [K]	$T_{\text{AOG,HEX2,out}}$ [K]	$Q_{\text{cracker,total}}$ [MW]
$x_{H_2,ICE} = 20\%, ecr = 0$	3.3	1073	361	640	0
$x_{H_2,ICE} = 20\%, ecr = 0.5$	6.9	1073	396	591	0.58
$x_{H_2,ICE} = 20\%, ecr = 1$	10.6	1073	410	541	1.16
$x_{H_2,ICE} = 30\%, ecr = 0$	2	1066	305 (infeasible)	614	0
$x_{H_2,ICE} = 30\%, ecr = 0.5$	5.7	1073	389	580	0.7
$x_{H_2,ICE} = 30\%, ecr = 1$	10.1	1073	408	530	1.4
$x_{H_2,ICE} = 40\%, ecr = 0$	2	1048	262 (impossible)	566	0
$x_{H_2,ICE} = 40\%, ecr = 0.5$	4.5	1073	379	572	0.83
$x_{H_2,ICE} = 40\%, ecr = 1$	9.7	1073	407	522	1.66

Table B.6: Heat management results of the simulations of design case 3 with 20, 30 and 40% hydrogen in the ICE and ecr=0, 0.5 and 1.

simulation ↓	λ [-]	T_{stack} [K]	$T_{\text{COG,HEX1,out}}$ [K]	$T_{\text{AOG,HEX2,out}}$ [K]	$Q_{\text{cracker,total}}$ [MW]
$x_{H_2,ICE} = 20\%, ecr = 0$	6.9	1073	396	673	0
$x_{H_2,ICE} = 20\%, ecr = 0.5$	9.3	1073	406	626	3.63
$x_{H_2,ICE} = 20\%, ecr = 1$	11.6	1073	412	578	7.26
$x_{H_2,ICE} = 30\%, ecr = 0$	6.7	1073	395	670	0
$x_{H_2,ICE} = 30\%, ecr = 0.5$	9.1	1073	405	623	3.75
$x_{H_2,ICE} = 30\%, ecr = 1$	11.5	1073	412	575	7.5
$x_{H_2,ICE} = 40\%, ecr = 0$	6.4	1073	394	667	0
$x_{H_2,ICE} = 40\%, ecr = 0.5$	8.9	1073	405	619	3.88
$x_{H_2,ICE} = 40\%, ecr = 1$	11.4	1073	412	571	7.76

Table B.7: Power density of the Bloom Energy Server 5 and the Wärtsilä 31DF genset. The Wärtsilä 31DF dimensions include the engine and generator combination (genset).

system →	Bloom Energy Server 5 [8]	Wärtsilä 31DF genset [7]
Power [kW]	300	6840
Length [m]	5.7	10.2
Width [m]	2.6	3.5
Height [m]	2.1	4.4
Volume [m^3]	32.2	152.8
Weight [kg]	15800	115000
Vol. PD [$kW \cdot m^{-3}$]	9.3	44.8
Grav. PD [$W \cdot kg^{-1}$]	19.0	59.5

Table B.8: Hybrid system dimensions based on the dimensions of the Bloom Energy Server 5 and the Wärtsilä 31DF genset (table B.7).

Power split →	50/50	25/75	75/25
SOFC power [kW]	6840	2280	20520
ICE power [kW]	6840	6840	6840
System power [kW]	13680	9120	27360
SOFC volume [m^3]	734	245	2203
ICE volume [m^3]	153	153	153
Combined size [m^3]	887	398	2356
SOFC weight [10^3 kg]	360	120	1081
ICE weight [10^3 kg]	115	115	115
Combined weight [10^3 kg]	475	235	1196

B.3. Dynamic response of the SOFC

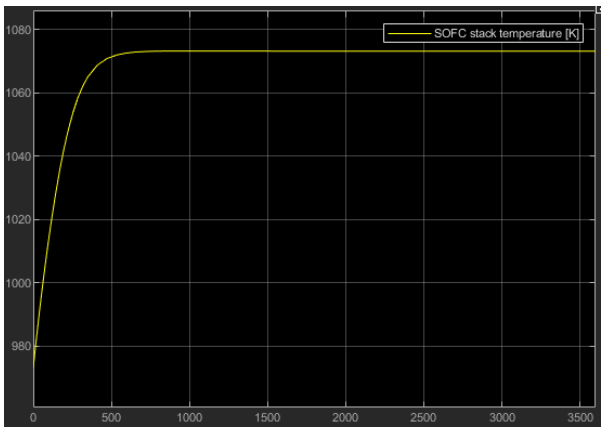

Figure B.19: Dynamic response of the stack temperature. The initial stack temperature is 973 K at $i = 5000\ A \cdot m^{-2}$, $UF = 0.7$, $ecr = 0.5$, $T_{SP} = 1073$ K. The figure is a screenshot from MATLAB & Simulink); the vertical axis is the temperature [K], the horizontal axis is the time in seconds.

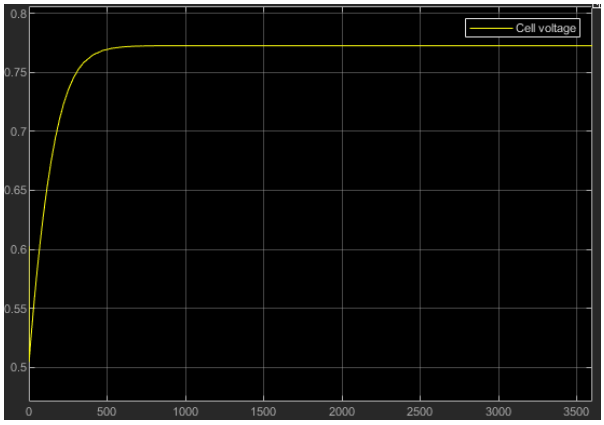

Figure B.20: Dynamic response of the cell voltage. The initial stack temperature is 973 K at $i = 5000\ \mathrm{A \cdot m^{-2}}$, $UF = 0.7$, $ecr = 0.5$, $T_{\mathrm{SP}} = 1073$ K. The figure is a screenshot from MATLAB & Simulink); the vertical axis is the cell voltage [V], the horizontal axis is the time in seconds.

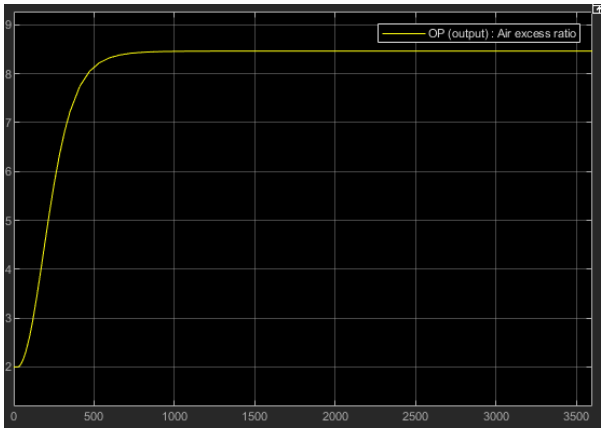

Figure B.21: Dynamic response of the SOFC air excess ratio. The initial stack temperature is 973 K at $i = 5000\ \mathrm{A \cdot m^{-2}}$, $UF = 0.7$, $ecr = 0.5$, $T_{\mathrm{SP}} = 1073$ K. The figure is a screenshot from MATLAB & Simulink); the vertical axis is the dimensionless air excess ratio, the horizontal axis is the time in seconds.

Bibliography

[1] Bloom Energy provides clean, cost-effective, AlwaysON electricity for organizations and communities. URL https://www.bloomenergy.com/.

[2] Emission Standards: Europe: Heavy-Duty Truck and Bus Engines, . URL https://dieselnet.com/standards/eu/hd.php.

[3] Emission Standards: IMO Marine Engine Regulations, . URL https://dieselnet.com/standards/inter/imo.php.

[4] NIST Chemistry WebBook. URL https://webbook.nist.gov/.

[5] Solid Oxide cell stack. URL https://elcogen.com/products/solid-oxide-cell-stacks/.

[6] Wärtsilä and Simon Møkster Shipping to study feasibility of ammonia and LNG dual-fuel operations, . URL https://tinyurl.com/wartsilafeasibilityammonia.

[7] Wärtsilä generating sets, . URL https://www.wartsila.com/marine/build/engines-and-generating-sets/generating-sets/wartsila-gensets.

[8] Bloomenergy Energy Server 5 product datasheet, 2019. URL https://www.bloomenergy.com/wp-content/uploads/es5-300kw-datasheet-2019.pdf.

[9] Fourth IMO GHG Study 2020. Technical report, 2020. URL https://docs.imo.org/Documents/Detail.aspx?did=125134.

[10] World's first full scale ammonia engine test - an important step towards carbon free shipping, 6 2020. URL https://tinyurl.com/wartsilafirstammoniatest.

[11] Wärtsilä launches major test programme towards carbon-free solutions with hydrogen and ammonia, 7 2021. URL https://tinyurl.com/Wartsilatests.

[12] Stuart B. Adler. Factors governing oxygen reduction in solid oxide fuel cell cathodes. *Chemical Reviews*, 104(10):4791–4843, 2004. ISSN 00092665. doi: 10.1021/cr020724o. URL https://pubs.acs.org/sharingguidelines.

[13] Ahmed Afif, Nikdalila Radenahmad, Quentin Cheok, Shahriar Shams, Jung H Kim, and Abul K Azad. Ammonia-fed fuel cells: a comprehensive review. 2016. doi: 10.1016/j.rser.2016.01.120. URL http://dx.doi.org/10.1016/j.rser.2016.01.120.

[14] P. Aguiar, C. S. Adjiman, and N. P. Brandon. Anode-supported intermediate temperature direct internal reforming solid oxide fuel cell. I: model-based steady-state performance. *Journal of Power Sources*, 138: 120–136, 2004. doi: 10.1016/j.jpowsour.2004.06.040.

[15] K. H.M. Al-Hamed and I. Dincer. A new direct ammonia solid oxide fuel cell and gas turbine based integrated system for electric rail transportation. *eTransportation*, 2, 2019. ISSN 25901168. doi: 10.1016/j.etran.2019.100027. URL https://doi.org/10.1016/j.etran.2019.100027.

[16] Khaled H.M. Al-Hamed and Ibrahim Dincer. A novel ammonia solid oxide fuel cell-based powering system with on-board hydrogen production for clean locomotives. *Energy*, 220:119771, 4 2021. ISSN 03605442. doi: 10.1016/j.energy.2021.119771.

[17] Vyjayanthi Alagharu, Srinivas Palanki, and Kevin N. West. Analysis of ammonia decomposition reactor to generate hydrogen for fuel cell applications. *Journal of Power Sources*, 195(3):829–833, 2010. ISSN 03787753. doi: 10.1016/j.jpowsour.2009.08.024.

[18] Amirpiran Amiri, Shi Tang, Robert Steinberger-Wilckens, and Moses O. Tadé. Evaluation of fuel diversity in Solid Oxide Fuel Cell system. *International Journal of Hydrogen Energy*, 43(52):23475–23487, 2018. ISSN 03603199. doi: 10.1016/j.ijhydene.2018.10.192. URL www.sciencedirect.com.

[19] Mirko Baratta, Daniela Misul, Ludovico Viglione, and Jiajie Xu. Combustion chamber design for a high-performance natural gas engine: CFD modeling and experimental investigation. *Energy Conversion and Management*, 192:221–231, 7 2019. ISSN 01968904. doi: 10.1016/j.enconman.2019.04.030. URL https://linkinghub.elsevier.com/retrieve/pii/S019689041930442X.

[20] Wolfgang G. Bessler, Stefan Gewies, and Marcel Vogler. A new framework for physically based modeling of solid oxide fuel cells. *Electrochimica Acta*, 53(4):1782–1800, 2007. ISSN 00134686. doi: 10.1016/j.electacta.2007.08.030. URL www.sciencedirect.com.

[21] L. van Biert. *Solid oxide fuel cells for ships: System integration concepts with reforming and thermal cycles*. PhD thesis, TU Delft, 2020. URL https://repository.tudelft.nl/islandora/object/uuid%3Add1f7899-38ee-4c78-a5b0-a6fa92c90f56?collection=research.

[22] L. van Biert, T. Woudstra, M. Godjevac, K. Visser, and P. V. Aravind. A thermodynamic comparison of solid oxide fuel cell-combined cycles. *Journal of Power Sources*, 397:382–396, 9 2018. ISSN 03787753. doi: 10.1016/j.jpowsour.2018.07.035. URL https://doi.org/10.1016/j.jpowsour.2018.07.035.

[23] Peter Van Blarigan. Advanced Internal Combustion Engine Research. Technical report, 2000.

[24] Astrid Boisen, Søren Dahl, Jens K. Nørskov, and Claus Hviid Christensen. Why the optimal ammonia synthesis catalyst is not the optimal ammonia decomposition catalyst. *Journal of Catalysis*, 230(2):309–312, 2005. ISSN 00219517. doi: 10.1016/j.jcat.2004.12.013. URL www.elsevier.com/locate/jcat.

[25] A. Boudghene Stambouli and E. Traversa. Solid oxide fuel cells (SOFCs): a review of an environmentally clean and efficient source of energy. Technical report, 2002. URL www.elsevier.com/locate/rser.

[26] T Boxma. Removal of nitrogen based pollutants from the AmmoniaDrive exhaust, 2021. URL http://resolver.tudelft.nl/uuid:914ca18b-d7be-4a70-8ba5-8390b4f738ab.

[27] Sandro Brandenberger, Oliver Kröcher, Arno Tissler, and Roderik Althoff. The state of the art in selective catalytic reduction of NOx by ammonia using metal-exchanged zeolite catalysts. *Catalysis Reviews - Science and Engineering*, 50(4):492–531, 2008. ISSN 01614940. doi: 10.1080/01614940802480122. URL https://www.tandfonline.com/action/journalInformation?journalCode=lctr20.

[28] Nigel P. Brandon, Enrique Ruiz-Trejo, and Paul Boldrin, editors. *Solid Oxide Fuel Cell Lifetime and Reliability*. Elsevier, 2017. ISBN 978-0-08101102-7.

[29] Annamaria Buonomano, Francesco Calise, Massimo Dentice d'Accadia, Adolfo Palombo, and Maria Vicidomini. Hybrid solid oxide fuel cells-gas turbine systems for combined heat and power: A review. *Applied Energy*, 156:32–85, 2015. ISSN 03062619. doi: 10.1016/j.apenergy.2015.06.027. URL http://dx.doi.org/10.1016/j.apenergy.2015.06.027.

[30] João Sousa Cardoso, Valter Silva, Rodolfo C. Rocha, Matthew J. Hall, Mário Costa, and Daniela Eusébio. Ammonia as an energy vector: Current and future prospects for low-carbon fuel applications in internal combustion engines. *Journal of Cleaner Production*, 296, 2021. ISSN 09596526. doi: 10.1016/j.jclepro.2021.126562. URL https://doi.org/10.1016/j.jclepro.2021.126562.

[31] S. H. Chan, K. A. Khor, and Z. T. Xia. Complete polarization model of a solid oxide fuel cell and its sensitivity to the change of cell component thickness. *Journal of Power Sources*, 93(1-2):130–140, 2001. ISSN 03787753. doi: 10.1016/S0378-7753(00)00556-5.

[32] Wonjae Choi, Jaehyun Kim, Yongtae Kim, and Han Ho Song. Solid oxide fuel cell operation in a solid oxide fuel cell–internal combustion engine hybrid system and the design point performance of the hybrid system. *Applied Energy*, 254, 11 2019. ISSN 03062619. doi: 10.1016/j.apenergy.2019.113681. URL https://doi.org/10.1016/j.apenergy.2019.113681.

[33] G. Cinti, U. Desideri, D. Penchini, and G. Discepoli. Experimental analysis of SOFC fuelled by ammonia. *Fuel Cells*, 14(2):221–230, 4 2014. ISSN 16156854. doi: 10.1002/fuce.201300276. URL www.fuelcells.wiley-vch.de.

[34] G. Cinti, G. Discepoli, E. Sisani, and U. Desideri. SOFC operating with ammonia: Stack test and system analysis. *International Journal of Hydrogen Energy*, 41(31):13583–13590, 2016. ISSN 03603199. doi: 10.1016/j.ijhydene.2016.06.070. URL http://dx.doi.org/10.1016/j.ijhydene.2016.06.070.

[35] G. Cinti, G. Discepoli, E. Sisani, and U. Desideri. SOFC operating with ammonia: Stack test and system analysis. *International Journal of Hydrogen Energy*, 41(31):13583–13590, 2016. ISSN 03603199. doi: 10.1016/j.ijhydene.2016.06.070.

[36] Massimo Colombo, Isabella Nova, Enrico Tronconi, Volker Schmeißer, Brigitte Bandl-Konrad, and Lisa Zimmermann. Experimental and modeling study of a dual-layer (SCR+PGM) NH3 slip monolith catalyst (ASC) for automotive SCR aftertreatment systems. Part 1. Kinetics for the PGM component and analysis of SCR/PGM interactions. *Applied Catalysis B: Environmental*, 142-143:861–876, 2013. ISSN 09263373. doi: 10.1016/j.apcatb.2012.10.031. URL http://dx.doi.org/10.1016/j.apcatb.2012.10.031.

[37] Massimiliano Comotti and Stefano Frigo. Hydrogen generation system for ammonia-hydrogen fuelled internal combustion engines. *International Journal of Hydrogen Energy*, 40(33):10673–10686, 2015. ISSN 03603199. doi: 10.1016/j.ijhydene.2015.06.080. URL http://dx.doi.org/10.1016/j.ijhydene.2015.06.080.

[38] Peter De Vos. AmmoniaDrive: a solution for zero-emission shipping?! *SWZ Maritime*, pages 36–37, 2020.

[39] N. J.J. Dekker and G. Rietveld. Highly efficient conversion of ammonia in electricity by solid oxide fuel cells. *Journal of Fuel Cell Science and Technology*, 3(4):499–502, 2006. ISSN 1550624X. doi: 10.1115/1.2349536. URL http://asmedigitalcollection.asme.org/electrochemical/article-pdf/3/4/499/5896582/499_1.pdf.

[40] Andrew Dicks and David Anthony James Rand. *Fuel Cell Systems Explained*, volume 3. John Wiley & Sons, 2018. ISBN 9781118613528.

[41] Pavlos Dimitriou and Rahat Javaid. A review of ammonia as a compression ignition engine fuel, 2 2020. ISSN 03603199. URL www.sciencedirect.com.

[42] Sudhanshu Dwivedi. Solid oxide fuel cell: Materials for anode, cathode and electrolyte. *International Journal of Hydrogen Energy*, 45(44):23988–24013, 2020. ISSN 03603199. doi: 10.1016/j.ijhydene.2019.11.234. URL www.sciencedirect.com.

[43] M. F. Ezzat and I. Dincer. Comparative assessments of two integrated systems with/without fuel cells utilizing liquefied ammonia as a fuel for vehicular applications. *International Journal of Hydrogen Energy*, 43(9):4597–4608, 3 2018. ISSN 03603199. doi: 10.1016/j.ijhydene.2017.07.203. URL http://dx.doi.org/10.1016/j.ijhydene.2017.07.203.

[44] Jeffrey W. Fergus. Electrolytes for solid oxide fuel cells. *Journal of Power Sources*, 162:30–40, 2006. doi: 10.1016/j.jpowsour.2006.06.062.

[45] Pio Forzatti. Present status and perspectives in de-NOx SCR catalysis. *Applied Catalysis A: General*, 222 (1-2):221–236, 2001. ISSN 0926860X. doi: 10.1016/S0926-860X(01)00832-8.

[46] Stefano Frigo and Roberto Gentili. Analysis of the behaviour of a 4-stroke Si engine fuelled with ammonia and hydrogen. *International Journal of Hydrogen Energy*, 38(3):1607–1615, 2013. ISSN 03603199. doi: 10.1016/j.ijhydene.2012.10.114. URL http://dx.doi.org/10.1016/j.ijhydene.2012.10.114.

[47] Maria Galluci. Why the Shipping Industry Is Betting Big on Ammonia. URL https://spectrum.ieee.org/transportation/marine/why-the-shipping-industry-is-betting-big-on-ammonia.

[48] J. I. Ghojel. Review of the development and applications of the Wiebe function: A tribute to the contribution of Ivan Wiebe to engine research. *International Journal of Engine Research*, 11(4):297–312, 2010. ISSN 14680874. doi: 10.1243/14680874JER06510.

[49] J. M. Gordon and Mahmoud Huleihil. General performance characteristics of real heat engines. *Journal of Applied Physics*, 72(3):829–837, 1992. ISSN 00218979. doi: 10.1063/1.351755. URL https://doi.org/10.1063/1.351755.

[50] Minfang Han, Xiuling Tang, Huiyan Yin, and Suping Peng. Fabrication, microstructure and properties of a YSZ electrolyte for SOFCs. *Journal of Power Sources*, 165(2):757–763, 2007. ISSN 03787753. doi: 10.1016/j.jpowsour.2006.11.054.

[51] Ronald M. Heck, Robert J. Farrauto, and Suresh T. Gulati. Selective catalytic reduction of NOx. In *Catalytic air pollution control : Commercial technology*, chapter 12.3, pages 407–416. John Wiley & Sons, 3 edition, 2013.

[52] Elbert Hendricks and Spencer C Sorenson. Mean Value Modelling of Spark Ignition Engines. Technical report, 1990.

[53] John B. Heywood. *Internal Combustion Engine Fundamentals*. McGraw-Hill,, 1988. ISBN 007028637X.

[54] John B. Heywood. *Internal Combustion Engine Fundamentals*. McGraw Hill Education, 2 edition, 2018. ISBN 978-1-26-011611-3.

[55] IMO. Air Pollution and Energy Efficiency. Final Report of the Correspondence Group on Assessment of Technological Developments to Implement the Tier III NOx Emission Standards under MARPOL Annex VI. Technical report, 2013. URL https://officeroftheWatch.files.wordpress.com/2014/04/imo-mepc-65-4-7-final-report-for-tier-iii-nox-emission-standards.pdf.

[56] F. Ishak, I. Dincer, and C. Zamfirescu. Energy and exergy analyses of direct ammonia solid oxide fuel cell integrated with gas turbine power cycle, 2012. ISSN 03787753.

[57] Boris Iwanschitz, Josef Sfeir, Andreas Mai, and Michael Schütze. Degradation of SOFC Anodes upon Redox Cycling: A Comparison Between Ni/YSZ and Ni/CGO. *Journal of The Electrochemical Society*, 157(2):B269–B277, 2010. ISSN 00134651. doi: 10.1149/1.3271101.

[58] Georgina Jeerh, Mengfei Zhang, and Shanwen Tao. Recent progress in ammonia fuel cells and their potential applications. *Journal of Materials Chemistry A*, 9(2):727–752, 2021. ISSN 20507496. doi: 10.1039/d0ta08810b.

[59] Yildiz Kalinci and Ibrahim Dincer. Analysis and performance assessment of NH3 and H2 fed SOFC with proton-conducting electrolyte. *International Journal of Hydrogen Energy*, 43(11):5795–5807, 2017. ISSN 03603199. doi: 10.1016/j.ijhydene.2017.07.234. URL http://dx.doi.org/10.1016/j.ijhydene.2017.07.234.

[60] Sanggyu Kang and Kook Young Ahn. Dynamic modeling of solid oxide fuel cell and engine hybrid system for distributed power generation. *Applied Energy*, 195:1086–1099, 2017. ISSN 03062619. doi: 10.1016/j.apenergy.2017.03.077. URL http://dx.doi.org/10.1016/j.apenergy.2017.03.077.

[61] Ying Wei Kang, Jun Li, Guang Yi Cao, Heng Yong Tu, Jian Li, and Jie Yang. Dynamic temperature modeling of an SOFC using least squares support vector machines. *Journal of Power Sources*, 179(2):683–692, 2008. ISSN 03787753. doi: 10.1016/j.jpowsour.2008.01.022.

[62] Ying Wei Kang, Jun Li, Guang Yi Cao, Heng Yong Tu, Jian Li, and Jie Yang. A reduced 1D dynamic model of a planar direct internal reforming solid oxide fuel cell for system research. *Journal of Power Sources*, 188(1):170–176, 2009. ISSN 03787753. doi: 10.1016/j.jpowsour.2008.11.073.

[63] Kyunghwa Kim, Gilltae Roh, Wook Kim, and Kangwoo Chun. A Preliminary Study on an Alternative Ship Propulsion System Fueled by Ammonia : Environmental and Economic Assessments. *Journal of Marine Science and Engineering*, 8, 2020. doi: 10.3390/jmse8030183.

[64] M. Kishimoto, H. Muroyama, S. Suzuki, M. Saito, T. Koide, Y. Takahashi, T. Horiuchi, H. Yamasaki, S. Matsumoto, H. Kubo, N. Takahashi, A. Okabe, S. Ueguchi, M. Jun, A. Tateno, T. Matsuo, T. Matsui, H. Iwai, H. Yoshida, and K. Eguchi. Development of 1 kW-class Ammonia-fueled Solid Oxide Fuel Cell Stack. *Fuel Cells*, 20(1):80–88, 2020. ISSN 16156854. doi: 10.1002/fuce.201900131. URL www.fuelcells.wiley-vch.de.

[65] Masashi Kishimoto, Naoto Furukawa, Tatsuya Kume, Hiroshi Iwai, and Hideo Yoshida. Formulation of ammonia decomposition rate in Ni-YSZ anode of solid oxide fuel cells. *International Journal of Hydrogen Energy*, 42(4):2370–2380, 1 2017. ISSN 03603199. doi: 10.1016/j.ijhydene.2016.11.183. URL http://dx.doi.org/10.1016/j.ijhydene.2016.11.183.

[66] Masashi Kishimoto, Tatsuya Kume, Hiroshi Iwai, and Hideo Yoshida. Numerical Analysis of Ammonia-Fueled Planar Solid Oxide Fuel Cells. *ECS Transactions*, 78(1):2845–2853, 2017. ISSN 1938-6737. doi: 10.1149/07801.2845ecst.

[67] T. Korakianitis, A. M. Namasivayam, and R. J. Crookes. Natural-gas fueled spark-ignition (SI) and compression-ignition (CI) engine performance and emissions. *Progress in Energy and Combustion Science*, 37(1):89–112, 2011. ISSN 03601285. doi: 10.1016/j.pecs.2010.04.002.

[68] Leigh Krietsch Boerner. Industrial ammonia production emits more CO2 than any other chemical-making reaction. Chemists want to change that. *Chemical & Engineering news*, 6 2019. URL https://cen-acs-org.tudelft.idm.oclc.org/environment/green-chemistry/Industrial-ammonia-production-emits-CO2/97/i24.

[69] James Larminie and Andrew Dicks. *Fuel cell systems explained: Second edition*. 2013. ISBN 9781118878330. doi: 10.1002/9781118878330.

[70] Robert Timothy Leah, Adam Bone, Ahmet Selcuk, Mahfujur Rahman, Andrew Clare, Mike Lankin, Florence Felix, Subhasish Mukerjee, and Mark Selby. Latest Results and Commercialization of the Ceres Power SteelCell® Technology Platform, 2019. ISSN 1938-6737. URL moz-extension://5788fbf0-a2a1-4465-9a43-63e846586dbb/enhanced-reader.html?openApp&pdf=https%3A%2F%2Fiopscience-iop-org.tudelft.idm.oclc.org%2Farticle%2F10.1149%2F09101.0051ecst%2Fpdf.

[71] Young Duk Lee, Kook Young Ahn, Tatiana Morosuk, and George Tsatsaronis. Exergetic and exergoeconomic evaluation of an SOFC-Engine hybrid power generation system. *Energy*, 145:810–822, 2018. ISSN 03605442. doi: 10.1016/j.energy.2017.12.102. URL https://doi.org/10.1016/j.energy.2017.12.102.

[72] E. W. Lemmon, M. L. Huber, and M. O. McLinden. REFPROP: Reference Fluid Thermodynamics and Transport Properties, 2010. URL https://www.nist.gov/srd/refprop.

[73] Charles Lhuillier, Pierre Brequigny, Francesco Contino, and Christine Mounaïm-Rousselle. Experimental study on ammonia/hydrogen/air combustion in spark ignition engine conditions. *Fuel*, 269, 2020. ISSN 00162361. doi: 10.1016/j.fuel.2020.117448. URL https://doi.org/10.1016/j.fuel.2020.117448.

[74] Jun Li, Hongyu Huang, Noriyuki Kobayashi, Zhaohong He, and Yoshihiro Nagai. Study on using hydrogen and ammonia as fuels: Combustion characteristics and NOx formation. *International Journal of Energy Research*, 38(9):1214–1223, 7 2014. ISSN 1099114X. doi: 10.1002/er.3141.

[75] Ye Lin, Ran Ran, Youmin Guo, Wei Zhou, Rui Cai, Jun Wang, and Zongping Shao. Proton-conducting fuel cells operating on hydrogen, ammonia and hydrazine at intermediate temperatures. *International Journal of Hydrogen Energy*, 35(7):2637–2642, 2010. ISSN 03603199. doi: 10.1016/j.ijhydene.2009.04.019.

[76] Jinlong Liu and Cosmin E. Dumitrescu. Single and double Wiebe function combustion model for a heavy-duty diesel engine retrofitted to natural-gas spark-ignition. *Applied Energy*, 248:95–103, 8 2019. ISSN 03062619. doi: 10.1016/j.apenergy.2019.04.098. URL https://doi.org/10.1016/j.apenergy.2019.04.098.

[77] Qianli Ma, Ranran Peng, Yongjing Lin, Jianfeng Gao, and Guangyao Meng. A high-performance ammonia-fueled solid oxide fuel cell. *Journal of Power Sources*, 161(1):95–98, 2006. ISSN 03787753. doi: 10.1016/j.jpowsour.2006.04.099.

[78] MAN Energy Solutions. MAN B&W ME-LGIP. URL `https://man-es.com/marine/products/lgip`.

[79] MAN Energy Solutions. Engineering the future: Two-stroke green-ammonia, 2019.

[80] Dario Marra, C. (Cesare) Pianese, Pierpaolo Polverino, and Marco Sorrentino. Models for solid oxide fuel cell systems : exploitation of models hierarchy for industrial design of control and diagnosis strategies. Technical report, 2016. URL `https://play.google.com/store/books/details?id=Lc6zCwAAQBAJ&rdid=book-Lc6zCwAAQBAJ&rdot=1&source=gbs_vpt_read`.

[81] Rakesh Kumar Maurya and Mohit Raj Saxena. Characterization of ringing intensity in a hydrogen-fueled HCCI engine. *International Journal of Hydrogen Energy*, 43(19):9423–9437, 5 2018. ISSN 03603199. doi: 10.1016/j.ijhydene.2018.03.194.

[82] Stephen John McPhail, Bruno Conti, and Jari Kiviaho. *The Yellow Pages of SOFC Technology - International Status of SOFC deployment 2017*. Number February. 2017. ISBN 978-88-8286-290-9.

[83] Kazunari Miyazaki, Hiroki Muroyama, Toshiaki Matsui, and Koichi Eguchi. Impact of the ammonia decomposition reaction over an anode on direct ammonia-fueled protonic ceramic fuel cells. *Sustainable Energy and Fuels*, 4(10):5238–5246, 2020. ISSN 23984902. doi: 10.1039/d0se00841a.

[84] Michael Moran, Howard Shapiro, Daisie Boettner, and Margaret Bailey. *Fundamentals of Engineering Thermodynmics*. John Wiley and Sons Inc, 7 edition, 2011. ISBN 13 978-0470-49590.

[85] C. S. Mørch, A. Bjerre, M. P. Gøttrup, S. C. Sorenson, and J. Schramm. Ammonia/hydrogen mixtures in an SI-engine: Engine performance and analysis of a proposed fuel system. *Fuel*, 90(2):854–864, 2 2011. ISSN 00162361. doi: 10.1016/j.fuel.2010.09.042.

[86] Jacob A. Moulijn. *Chemical process technology*, volume 51. 2013. ISBN 9781444320244. doi: 10.5860/choice.51-2107.

[87] Hung Nguyen-Schäfer. *Rotordynamics of automotive turbochargers: Linear and nonlinear rotordynamics-bearing design-rotor balancing*. Springer, Stuttgart, 2012. ISBN 9783642275180. doi: 10.1007/978-3-642-27518-0. URL `www.springer.com`.

[88] Meng Ni, Dennis Y C Leung, and Michael K H Leung. Thermodynamic analysis of ammonia fed solid oxide fuel cells: Comparison between proton-conducting electrolyte and oxygen ion-conducting electrolyte. *Journal of Power Sources*, 183:682–686, 2008. doi: 10.1016/j.jpowsour.2008.05.022.

[89] Meng Ni, Dennis Y.C. Leung, and Michael K.H. Leung. Mathematical modeling of ammonia-fed solid oxide fuel cells with different electrolytes. *International Journal of Hydrogen Energy*, 33(20):5765–5772, 2008. ISSN 03603199. doi: 10.1016/j.ijhydene.2008.07.021.

[90] D. A. Noren and M. A. Hoffman. Clarifying the Butler-Volmer equation and related approximations for calculating activation losses in solid oxide fuel cell models. *Journal of Power Sources*, 152(1-2):175–181, 2005. ISSN 03787753. doi: 10.1016/j.jpowsour.2005.03.174.

[91] Masahiko Okabe, Katsuhiko Sakaguchi, Masahide Sugihara, Akihiro Miyanagi, Naohiro Hiraoka, and Satoru Murata. World's Largest Marine 2-Stroke Diesel Test Engine , the 4UE-X3 - Development in Compliance with the Next Version of Environmental Regulations and Gas Engine Technology -. Technical Report 1, 2013.

[92] T. Okanishi, K. Okura, A. Srifa, H. Muroyama, T. Matsui, M. Kishimoto, M. Saito, H. Iwai, H. Yoshida, M. Saito, T. Koide, H. Iwai, S. Suzuki, Y. Takahashi, T. Horiuchi, H. Yamasaki, S. Matsumoto, S. Yumoto, H. Kubo, J. Kawahara, A. Okabe, Y. Kikkawa, T. Isomura, and K. Eguchi. Comparative Study of Ammonia-fueled Solid Oxide Fuel Cell Systems. *Fuel Cells*, 17(3):383–390, 2017. ISSN 16156854. doi: 10.1002/fuce.201600165.

[93] Sung Ho Park, Young Duk Lee, and Kook Young Ahn. Performance analysis of an SOFC/HCCI engine hybrid system: System simulation and thermo-economic comparison. *International Journal of Hydrogen Energy*, 39(4):1799–1810, 1 2014. ISSN 03603199. doi: 10.1016/j.ijhydene.2013.10.171. URL http://dx.doi.org/10.1016/j.ijhydene.2013.10.171.

[94] Roland Peters, Robert Deja, Ludger Blum, Jari Pennanen, Jari Kiviaho, and Tuomas Hakala. Analysis of solid oxide fuel cell system concepts with anode recycling. *International Journal of Hydrogen Energy*, 38(16):6809–6820, 2013. ISSN 03603199. doi: 10.1016/j.ijhydene.2013.03.110. URL http://dx.doi.org/10.1016/j.ijhydene.2013.03.110.

[95] Roland Peters, Robert Deja, Maximilian Engelbracht, Matthias Frank, Van Nhu Nguyen, Ludger Blum, and Detlef Stolten. Efficiency analysis of a hydrogen-fueled solid oxide fuel cell system with anode off-gas recirculation. *Journal of Power Sources*, 328:105–113, 2016. ISSN 03787753. doi: 10.1016/j.jpowsour.2016.08.002. URL http://dx.doi.org/10.1016/j.jpowsour.2016.08.002.

[96] M Pochet, I Truedsson, F Foucher, H Jeanmart, and F Contino. Ammonia-Hydrogen Blends in Homogeneous-Charge Compression-Ignition Engine. *SAE Technical Papers*, pages 2017–2041, 2017. doi: 10.4271/2017-24-0087. URL https://doi.org/10.4271/2017-24-0087.

[97] Maxime Pochet, Hervé Jeanmart, and Francesco Contino. A 22:1 Compression Ratio Ammonia-Hydrogen HCCI Engine: Combustion, Load, and Emission Performances. *Frontiers in Mechanical Engineering*, 6:43, 2020. ISSN 2297-3079. doi: 10.3389/fmech.2020.00043. URL www.frontiersin.org.

[98] C. D. Rakopoulos and C. N. Michos. Development and validation of a multi-zone combustion model for performance and nitric oxide formation in syngas fueled spark ignition engine. *Energy Conversion and Management*, 49(10):2924–2938, 10 2008. ISSN 01968904. doi: 10.1016/j.enconman.2008.02.011.

[99] Rolf D. Reitz and Ganesh Duraisamy. Review of high efficiency and clean reactivity controlled compression ignition (RCCI) combustion in internal combustion engines. *Progress in Energy and Combustion Science*, 46:12–71, 2015. ISSN 03601285. doi: 10.1016/j.pecs.2014.05.003. URL http://dx.doi.org/10.1016/j.pecs.2014.05.003.

[100] J. W. Reurings. *A modeling study to investigate performance of SOFC-ICE hybrid systems for marine applications (MSc thesis)*. 2019. URL http://repository.tudelft.nl/.

[101] David Richardson, Heather Felgate, Nick Watmough, Andrew Thomson, and Elizabeth Baggs. Mitigating release of the potent greenhouse gas N2O from the nitrogen cycle - could enzymic regulation hold the key? *Trends in Biotechnology*, 27(7):388–397, 2009. ISSN 01677799. doi: 10.1016/j.tibtech.2009.03.009.

[102] Harsh Sapra, Milinko Godjevac, Peter De Vos, Wim Van Sluijs, Youri Linden, and Klaas Visser. Hydrogen-natural gas combustion in a marine lean-burn SI engine: A comparitive analysis of Seiliger and double Wiebe function-based zero–dimensional modelling. *Energy Conversion and Management*, 207, 3 2020. ISSN 01968904. doi: 10.1016/j.enconman.2020.112494. URL https://doi.org/10.1016/j.enconman.2020.112494.

[103] Harsh Sapra, Jelle Stam, Jeroen Reurings, Lindert van Biert, Wim van Sluijs, Peter de Vos, Klaas Visser, Aravind Purushothaman Vellayani, and Hans Hopman. Integration of solid oxide fuel cell and internal combustion engine for maritime applications. *Applied Energy*, 281, 2021. ISSN 03062619. doi: 10.1016/j.apenergy.2020.115854. URL http://creativecommons.org/licenses/by/4.0/.

[104] H.D. Sapra. *Combined Gas Engine- Solid Oxide Fuel Cell Systems for Marine Power Generation*. PhD thesis, TU Delft, 2020.

[105] F. Schüth, R. Palkovits, R. Schlögl, and D. S. Su. Ammonia as a possible element in an energy infrastructure: Catalysts for ammonia decomposition. *Energy and Environmental Science*, 5(4):6278–6289, 2012. ISSN 17545706. doi: 10.1039/c2ee02865d. URL http://pubs.rsc.org.

[106] Shabana P.S. Shaikh, Andanastuti Muchtar, and Mahendra R. Somalu. A review on the selection of anode materials for solid-oxide fuel cells. *Renewable and Sustainable Energy Reviews*, 51:1–8, 2015. ISSN 18790690. doi: 10.1016/j.rser.2015.05.069. URL http://dx.doi.org/10.1016/j.rser.2015.05.069.

[107] O. Siddiqui and I. Dincer. Development and Assessment of a Novel Integrated System Using an Ammonia Internal Combustion Engine and Fuel Cells for Cogeneration Purposes. 2019. doi: 10.1021/acs.energyfuels.8b04323. URL https://pubs.acs.org/sharingguidelines.

[108] R. P. Sinha and Wan Mohd Norsani Wan Nik. Investigation of propulsion system for large LNG ships. In *IOP Conference Series: Materials Science and Engineering*, volume 36, 2012. doi: 10.1088/1757-899X/36/1/012004.

[109] D. Stapersma. Diesel Engines Volume 1: Performance Analysis, 2010.

[110] Chunwen Sun. Anodes for Solid Oxide Fuel Cell. In Bin Zhu, Rizwan Raza, Liangdong Fan, and Chunwen Sun, editors, *Solid Oxide Fuel Cells: From Electrolyte-Based to Electrolyte-Free Devices*, chapter 4, pages 113–144. John Wiley & Sons, 1 edition, 2020. ISBN 978-3-527-34411-6.

[111] Chunwen Sun, Rob Hui, and Justin Roller. Cathode materials for solid oxide fuel cells: A review. *Journal of Solid State Electrochemistry*, 14(7):1125–1144, 2010. ISSN 14328488. doi: 10.1007/s10008-009-0932-0.

[112] Francisco A. Uribe. Effect of Ammonia as Possible Fuel Impurity on Pem Fuel Cell Performance. In *ECS Proceedings Volumes*, volume 1998-27, pages 229–237, 1998. doi: 10.1149/199827.0229pv.

[113] K. Wang, D. Hissel, M. C. Péra, N. Steiner, D. Marra, M. Sorrentino, C. Pianese, M. Monteverde, P. Cardone, and J. Saarinen. A Review on solid oxide fuel cell models. *International Journal of Hydrogen Energy*, 36(12):7212–7228, 2011. ISSN 03603199. doi: 10.1016/j.ijhydene.2011.03.051.

[114] Wärtsilä. New Wärtsilä 31 engine achieves Guinness World Records title. URL https://tinyurl.com/wartsilaworldrecord.

[115] Fredrik R. Westlye, Anders Ivarsson, and Jesper Schramm. Experimental investigation of nitrogen based emissions from an ammonia fueled SI-engine. *Fuel*, 111(2):239–247, 2013. ISSN 00162361. doi: 10.1016/j.fuel.2013.03.055. URL http://dx.doi.org/10.1016/j.fuel.2013.03.055.

[116] Mark Christopher Williams, Shailesh D Vora, and Gary Jesionowski. Worldwide Status of Solid Oxide Fuel Cell Technology. *ECS Transactions*, 96(1):1–10, 2020. ISSN 1938-6737. doi: 10.1149/09601.0001ecst.

[117] WingD. Selective Catalytic Reduction FAQ. URL https://www.wingd.com/en/documents/general/brochures/wingd-scr-technology-faq/.

[118] Adam Wojcik, Hugh Middleton, Ioannis Damopoulos, and Jan Van Herle. Ammonia as a fuel in solid oxide fuel cells. *Journal of Power Sources*, 118(1-2):342–348, 2003. ISSN 03787753. doi: 10.1016/S0378-7753(03)00083-1.

[119] Handa Xi and Jing Sun. Dynamic analysis of planar solid oxide fuel cell models with different assumptions of temperature layers. *Journal of Fuel Cell Science and Technology*, 6(1):0110111–01101112, 2009. ISSN 1550624X. doi: 10.1115/1.2971055.

[120] Mingfa Yao, Zhaolei Zheng, and Haifeng Liu. Progress and recent trends in homogeneous charge compression ignition (HCCI) engines. *Progress in Energy and Combustion Science*, 35(5):398–437, 2009. ISSN 03601285. doi: 10.1016/j.pecs.2009.05.001.

[121] S. F. Yin, B. Q. Xu, X. P. Zhou, and C. T. Au. A mini-review on ammonia decomposition catalysts for on-site generation of hydrogen for fuel cell applications. *Applied Catalysis A: General*, 277(1-2):1–9, 2004. ISSN 0926860X. doi: 10.1016/j.apcata.2004.09.020. URL www.elsevier.com/locate/apcata.

[122] C. Zamfirescu and I. Dincer. Using ammonia as a sustainable fuel. *Journal of Power Sources*, 185(1):459–465, 2008. ISSN 03787753. doi: 10.1016/j.jpowsour.2008.02.097.

[123] C Zamfirescu and I Dincer. Ammonia as a green fuel and hydrogen source for vehicular applications. *Fuel Processing Technology*, 90:729–737, 2009. doi: 10.1016/j.fuproc.2009.02.004.

[124] Xiao Sen Zheng. *An investigation of hydrogen-ammonia combustion inside internal combustion engines*. 2020. URL https://repository.tudelft.nl/islandora/object/uuid%3A2372f356-c197-4286-b6fe-5b2873b40539?collection=education.

[125] W. Z. Zhu and S. C. Deevi. A review on the status of anode materials for solid oxide fuel cells. *Materials Science and Engineering A*, 362(1-2):228–239, 2003. ISSN 09215093. doi: 10.1016/S0921-5093(03)00620-8.

[126] W. Z. Zhu and S. C. Deevi. Development of interconnect materials for solid oxide fuel cells. Technical Report 1-2, 2003. URL www.elsevier.com/locate/msea.